UNIVERSITY OF CALIFORNIA SAN DIEGO

SAN DIEGO STATE UNIVERSITY

Organic Multiferroic Composites

A dissertation submitted in partial satisfaction of the

requirements for the degree Doctor of Philosophy

in

Engineering Sciences (Mechanical and Aerospace Engineering)

by

Scott William Newacheck

Committee in charge:

University of California San Diego

Professor Prabhakar Bandaru, Co-Chair
Professor Vitali Nesterenko
Professor Yu Qiao

San Diego State University

Professor George Youssef, Co-Chair
Professor Khaled Morsi

2021

The Dissertation of Scott William Newacheck is approved, and it is acceptable in quality and form for publication on microfilm and electronically:

_____

_____

_____

_____

Co-chair

_____

Co-chair

University of California San Diego

San Diego State University

2021

TABLE OF CONTENTS

LIST OF FIGURES

LIST OF TABLES

LIST OF SUPPLEMENTARY FILES

Newacheck_Document_SupplementaryChapter2.pdf

Newacheck_Document_SupplementaryChapter4.pdf

ACKNOWLEDGEMENTS

I would like to acknowledge Professor George Youssef for his support as my advisor, mentor, and as the chair of my committee. The completion of my dissertation would not be possible without his dedication and expertise. I would also like to acknowledge Professor Prabhakar Bandaru for his invaluable advice and guidance. Additionally, I am grateful of Professor Vitali Nesterenko, Professor Khaled Morsi, and Professor Yu Qiao for their time and insightful discussions. The project would not be possible without the funding from the Department of Defense (Contract No. W911NF1410039 and W911NF1810477) and internal support from San Diego State University.

Chapter 1, in full, is a reprint of the material as it appears in Composites Part B: Engineering, 2019. Youssef, George. The dissertation author was the primary investigator and author of this paper.

Chapter 2, in full, has been submitted for publication of the material as it may appear in International Journal of Mechanical Sciences 2021. Youssef, George. The dissertation author was the primary investigator and author of this paper.

Chapter 3, in full, has been submitted for publication of the material as it may appear in International Journal of Engineering Sciences 2021. Singh, Anil. Youssef, George. The dissertation author was the primary investigator and author of this paper.

Chapter 4, in full, has been submitted for publication of the material as it may appear in Crystal Growth and Design 2021. Huynh, Nha Uyen. Youssef, George. The dissertation author was the primary investigator and author of this paper.

Chapter 5, in part, is currently being prepared for submission for publication of the material. Huynh, Nha Uyen; Youssef, George. The dissertation author was the primary investigator and author of this material.

Chapter 6, in part, is currently being prepared for submission for publication of the material. Youssef, George. The dissertation author was the primary author of this chapter.

VITA

2012 Bachelor of Science, University of California: Irvine

2017 Master of Science, San Diego State University

2021 Doctor of Philosophy, University of California San Diego

2021 Doctor of Philosophy, San Diego State University

PUBLICATIONS

Youssef, G., Newacheck, S., Huynh, N., Gamez, C., (2021) Multiscale Characterization of E-Glass/Epoxy Composite Exposed to Extreme Environmental Conditions. J. Compos. Sci. 5, no. 3: 80.

Stampfli R., Newacheck S., Youssef G. (2021). Fully-coupled Computational Modeling of the Dynamic Response of 1-3 Multiferroic Composite Structures. International Journal of Mechanical Sciences 191, 106086

Newacheck S., Youssef G. (2020). Noncontact spatiotemporal strain mapping of composite multiferroic cylinders. International Journal of Mechanics and Materials in Design 16, 857-868 6

Youssef G., Nacy S., Newacheck S. (2020). Leveraging strain localization to improve the performance of magnetoelectric composite cylinders EPL (Europhysics Letters) 131 (1), 14003 4

Youssef G., Newacheck S., Lopez M., Stampfli R. (2020). Triaxial Magnetic Flux Emanation in Response to Uniaxial Electric Field in Magnetoelectric Composite Cylinder Structure. physica status solidi (a) 217 (15), 2000177

Newacheck S., Youssef G. (2020). Magnetoelectricity beyond saturation. Materials Horizons 7 (8), 2124-2129

Youssef G., Nacy S., Newacheck S. (2020). Dynamic magnetoelectric response of composite multiferroics cylinders. Smart Materials and Structures 29 (3), 035025 9

Youssef G., Newacheck S., Yousuf L.S. (2020). Insights into the displacement field in magnetoelectric composites. Journal of Intelligent Material Systems and Structures 31 (3), 436-444 6

Newacheck S., Youssef G. (2019). Wireless energy transfer based on strain-mediated composite multiferroics. Smart Materials and Structures 29 (1), 015014 10

Newacheck S., Weers W., Kolber D., Rutherford K., Youssef G. (2019). Advancing Ship Model's Mobility and Agility Using Steerable Rim-Driven Thrusters. Journal of Ocean Technology 14 (4)

Newacheck S., Youssef G. (2019). Synthesis and characterization of polarized novel 0–3 Terfenol-D/PVDF-TrFE composites. Composites Part B: Engineering 172, 97-102 7

Newacheck S., Webster T., Youssef G. (2018). The effect of multidirectional bias magnetic fields on the converse magnetoelectric response of multiferroic concentric composite ring. Applied Physics Letters 113 (17), 172902 12

Youssef G., Newacheck S., Lopez M. (2017). Mapping magnetoelastic response of terfenol-D ring structure. Applied Physics Letters 110 (19), 192408 14

Youssef G., Lopez M., Newacheck S. (2017). On the effect of polarization direction on the converse magnetoelectric response of multiferroic composite rings. Smart Materials and Structures 26 (3), 037003 24

FIELDS OF STUDY

Major Field: Engineering

Study in Mechanics and Materials
Professors George Youssef and Prabhakar Bandaru

ABSTRACT OF THE DISSERTATION

Soft Organic Multiferroic Composites

by

Scott William Newacheck

Doctor of Philosophy in Engineering Science (Mechanical and Aerospace Engineering)
University of California San Diego, 2021
San Diego State University, 2021

Professor George Youssef, Chair

Professor Prabhakar Bandaru, Co-Chair

Multiferroic magnetoelectric composites are an attractive material system for multifunctional design due to their ability to bidirectionally couple magnetic and electric fields at nearly all length and time scales. Unfortunately, all efficient multiferroic composites have been reliant on stiff, brittle, and sometimes lead-based materials, which inhibits their implementation to wearable, biomedical, and soft robotic applications. Many prior soft and semi-organic multiferroic composites have been investigated and reported in literature, however they fall orders of magnitude short to their stiff and brittle counterparts. Thus, the objective of this project is to develop a novel class of soft semi-organic or completely organic multiferroic composites with

considerable magnetoelectric coupling. The hypotheses of the proposed research is based on overcoming two engineering shortcomings of the prior semi-organic multiferroic research; namely the poor magnetostriction and property-mismatch arbitration. Therefore, two classes of composite materials are proposed which aim to replace the poorly performing ferromagnetic materials in prior studies with 1) giant magnetostrictive rare-earth alloy particulates or 2) newly discovered organic magnetic polymers. The composites were fabricated, analyzed, and characterized through computational and experimental techniques, including finite element analysis, explicit dynamic modeling, probe force microscopy, magnetometry, crystallography, dynamic mechanical analysis, dielectric analysis, terahertz and infrared spectroscopy, and other various testing methods. The culmination of the characterization techniques produces comprehensive property maps of these two composites which elucidates pitfalls and enlighten scientific foundations of how each material can beneficially or detrimentally affect the other. Results show the feasibility of these composites to fill various applications and illuminates a path for future studies to take soft multiferroic composites even further.

Introduction

In conventional design, each material component generally serves a single purpose. A few examples include concrete pillars for structural support, copper wires for electrical conductivity, polymer coatings for wear resistance, and magnets for the construction of electric motors. The multifunctional design paradigm uses materials and composites that possess multiple physical properties to fulfill multiple simultaneous usages [1], [2]. A common example of a multifunctional design is the aluminum frames of electronic devices, providing structural protection while being an electrical ground source. More advanced multifunctional designs could be a load-bearing structure that has the capability for vibration control and energy harvesting/storage[3]. Thus, creative designs of multifunctional materials can reduce weight, improve efficiency, and minimize cost.

Arguably, at the pinnacle of multifunctional materials lie multiferroics, used for their ferromagnetic, ferroelectric, and in many cases for their structural, piezoelectric, pyroelectric, magnetostrictive, magnetodielectric, and magnetoelectric properties [4]–[6]. Multiferroics materials can harvest, store, sense, and actuate magnetic, electrical, thermal, and mechanical energy [7]–[9]. Magnetoelectricity is the bidirectional coupling of magnetism with electric polarization. It can substitute nearly any induction-based electromagnetic technology while offering many benefits, such as multifunctionality, multidirectional coupling, linear scalability, and often-lower power consumption. However, finding such a capable material is still an active research quest since most of the known multiferroics lose some of their ferroic properties at ambient temperatures. For example, BiFeO is one of the best performing multiferroic materials with strong ferroelectric properties but with an abysmally weak ferromagnetic response at room

temperature [10]. Until an efficient room-temperature multiferroic material is discovered or synthesized, engineers rely on multiferroic composites to satisfy their multifunctional or magnetoelectric needs. Multiferroic composites are various combinations of ferroelectric and ferromagnetic materials, which, as a whole, can have the properties of monolithic multiferroic materials but can operate at room temperature efficiently.

The rare magnetodielectric and magnetoelectric properties possessed by multiferroics enable innovative technologies that would be unachievable otherwise. For example, the length of a conventional antenna is fixed to be roughly equal to half of the wavelength of the transmitted/received electromagnetic signals Alternatively, magnetoelectric bulk wave acoustic antennas defy the size-limit in traditional counterparts and can be several orders of magnitude smaller than the signal wavelength [11]. Another example that our group have recently demonstrated is multiferroics-based wireless power transfer transmitters and receivers, which possess the unique ability to simultaneously transmit electrical, mechanical, and magnetic energy [12]. Our novel multiferroics-based transmitter and receiver elements are universal and can work with any other conventional near-field wireless power system, namely, induction, capacitance, or acoustic [12].

Combining any two ferroelectric and ferromagnetic materials is unlikely to achieve a magnetoelectric response, as it generally requires substantial development effort and comprehensive engineering analysis. There are a few different mechanisms that engineers exploit to attain magnetoelectric properties, namely, strain-mediation, charge-mediation, spin-exchange, along with a few others [13], [14]. Strain-mediation approach is the most widely studied and has achieved higher magnetoelectric efficiencies than their other counterparts [15]–[30]. The magnetoelectric efficiency is quantified by the ratio of the input magnetic flux to the output electric

field (or vise-versa) and is usually reported in units of V/Oe·cm (or [A/m][m/V]). Strain-mediated magnetoelectric coupling relies on the piezoelectric and magnetostrictive properties found in some ferroelectric and all ferromagnetic materials, respectively. In the direct sense, application of a magnetic field induces the ferromagnetic material to deform based on their magnetostriction properties, where the deformation exerts a stress on the ferroelectric phase of the composite that then produces electric charges due to the piezoelectric effect. Conversely, an electric field applied across the ferroelectric material generates piezoelectric strain, which, in turn, alters the state of magnetism of the ferromagnetic material. Thus, the efficacy of strain-mediated magnetoelectric coupling is reliant on the piezoelectric and magnetostrictive properties of the constituents and the efficiency of strain to transfer between the two phases. Many different combinations of piezoelectric and magnetostrictive materials have been explored for magnetoelectric coupling. Table 0-1 lists a few notable material candidates and their properties.

Table 0-1. List of prominent piezoelectric and magnetostrictive materials with their associated properties [31]–[33]

Piezoelectric			Magnetostrictive		
Material	Coupling	Stiffness	Material	Coupling	Stiffness
PZT	117	70	Metglas	12000	117
PMN-PT	2000	172	Terfenol-D	15707	30
BaTiO	17.5	140	Fe_3O_4	140	200
PVDF	28	1.5	$CoFe_2O_4$	1880	153

In addition to the material candidates, many configurations (i.e., stacking configurations) such as particle-matrix, fiber-matrix, and laminate layers, referred herein as 0-3, 1-3, and 2-2, respectively, have been explored either to improve the strain transfer or to achieve other particular goals, as discussed later [34]. Table 0-2 lists a few of the greatest magnetoelectric coupling

efficiencies reported along with the materials and configuration used. Notably, the highest yielding composites are mostly laminates of magnetostrictive alloys with piezoelectric ceramics with a few exceptions of piezoelectric polymers. Unfortunately, all of the piezoelectric ceramics and most of the magnetostrictive alloys are very stiff and brittle, which may be unfavorable for engineering designs that require large deformation (e.g., biomedical applications or wearable electronics). That is, soft magnetoelectric composite will enable their use in wearable, biomedical, and soft robotic applications, making their development highly desirable.

Table 0-2. Reported high efficiency magnetoelectric composites

Magnetoelectric coupling	Magnetostrictive Material	Piezoelectric Material	Configuration	Reference
52 V/cm·Oe	Metglas	PVDF	2-2	[35]
51 V/cm·Oe	Metglas	PMN-PT	2-2	[36]
11 V/cm·Oe	Terfenol-D	PMN-PT	2-2	[37]
9 V/cm·Oe	Terfenol-D	PZT	2-2	[38]
5 V/cm·Oe	CoCu-NFO	PZT	0-3	[39]
1.5 V/cm·Oe	Terfenol-D	PVDF	2-2	[16]

The potential for soft magnetoelectric composites has motivated research in 0-3 inorganic-organic composites, which are metallic magnetostrictive particles embedded into a piezoelectric polymer matrix. This composite configuration achieves a soft and compliant behavior since their mechanical properties are largely influenced by the polymer matrix [40]. Moreover, PVDF, a well-established and high performing piezoelectric polymer, has high chemical and wear resistance making it even more appealing for multifunctional applications [41]–[43]. Importantly, many analytical models predict large magnetoelectric coupling of soft 0-3 magnetoelectric composites, further inspiring their research. For example, Nan *et al*. used Green's function to analytically

predict 25%-50% magnetoelectric coupling efficiency in 0-3 inorganic-organic composite structure when compared to 2-2 counterpart [44]. Since a few 2-2 inorganic-organic composites exhibit a high magnetoelectric response, as observed from the data in Table 0-2, it was expected that a few 0-3 composites would be comparable. However, that is far from the case. Despite several attempts to synthesize soft 0-3 magnetoelectric composites, the reported magnetoelectric coefficients have fallen orders of magnitude lower than the analytical expectations. Table 0-3 lists various soft 0-3 magnetoelectric composites and their reported efficiencies. Moreover, many published 0-3 composites that were likely fabricated for magnetoelectric coupling, chose not to report it probably due to their poor performance. Most research groups dedicated to soft 0-3 composites have pivoted to find other means of usefulness for multifunctional design, such as magnetodielectric [45]. Departing from the common approach, this dissertation continues to investigate the mechanisms leading to the shortcomings of soft magnetoelectric composites.

Table 0-3. Reported inorganic-organic 0-3 magnetoelectric composites

Magnetoelectric coupling	Magnetostrictive Material	Piezoelectric Material	Configuration	Reference
0.0400 V/cm·Oe	CFO	PVDF	0-3	[46]
0.0180 V/cm·Oe	Fe	PU	0-3	[47]
0.0013 V/cm·Oe	$Ni_{0.5}Zn_{0.5}Fe_2O_4$	PVDF-TrFE	0-3	[48]
No report	Fe_3O_4	PVDF	0-3	[49]
No report	$Ni_{0.5}Zn_{0.5}Fe_2O_4$	PVDF	0-3	[45]
No report	$BaFe_{12}O_{19}$	PVDF	0-3	[50]

There are two paramount shortcomings of soft 0-3 magnetoelectric composites, each of which happen to exacerbate the other, namely percolation/electrical breakdown and magnetic particle size limitations. The particles must not make a percolated conductive path through the

matrix; otherwise, the electric displacement is nullified. To have a reasonable probability to prevent shunts from randomly forming, the particles must be much smaller than the thickness of the matrix. This typically mandates the particles to be on the nanometer-scale, limiting the potential for their magnetic properties. Moreover, this limitation has led research groups to rely on suboptimal magnetic materials, such as iron oxide, since most high output magnetostrictive materials, such as Terfenol-D, oxidizes in small volumes [51]. It is worth noting that hardly any of the magnetostrictive materials used in the top performing magnetoelectric composites in Table 0-2 are used in the list of soft 0-3 composites in Table 0-3, for the aforementioned reason. Thus, this dissertation *firstly aims* to fabricate and characterize a soft 0-3 multiferroic composite with a high output magnetostrictive materials, specifically, Terfenol-D.

Chapter 1 of this dissertation is focused on fabricating 0-3 Terfenol-D/PVDF-TrFE multiferroic composite that do not percolate or succumb to dielectric breakdown. The ferroelectric, dielectric, and piezoelectric properties of the composites with different loading percentages were characterized. Chapter 2 pivots to computational modeling of the soft 0-3 multiferroic composites to answer questions that arose from the work in Chapter 1, such as the effect of particle settling, agglomerations, and their geometry. The computational model verified a few speculative explanations from Chapter 1, along with alleviating the concerns about particle settling. However, the expected magnetoelectric output was significantly lower than the analytical models have suggested due to micromechanics, which were previously ignored. Chapter 3 completes the property-map of the 0-3 Terfenol-D/PVDF-TrFE composite material by experimentally characterizing the mechanical, morphological, chemical, magnetic, and magnetoelectric properties. Another shortcoming was discovered, the investigated composites quickly nullify their efficiency due particle migration and agglomeration. The magnetic particles were observed to be

able to escape and migrate through the polymer matrix during testing and form the shunts, which are the aforementioned shortcomings that 0-3 composites must meticulously avoid. Ways to prolong the lifetime of the composites were identified and discussed.

The persistent underperformance 0-3 composites motivated a pivot to investigate a new and exciting topic in research, organic ferromagnetic materials to explore their potential in soft multiferroic composites. Two early identified benefits for organic-based ferromagnetic materials in soft multiferroic composites are that 1) the elastic properties of the two phases will be similar (for better strain transfer), and that 2) the geometrical requirement can be relaxed (they do not have to be particles since they can bend), bypassing the aforementioned shortcomings of inorganic-organic 0-3 composites. Experimental chemists have now synthesized hundreds of purely organic ferromagnetic molecules and polymers[52], [53]. A small subset of the synthesized molecular magnets exhibit magnetic properties above room temperature. Figure 0-1 displays some well-discussed organic magnetic materials and their respective Curie temperatures on a schematic log-scale thermometer [4], [6]–[11]. It should be noted that the temperatures listed for triaminobenzene and P3HT:PCBM are the pyrolysis temperatures since it occur before reaching the Curie temperature. Of the few available room-temperature organic ferromagnets, P3HT:PCBM is particularly alluring for its replicability, while independent researchers (including myself) struggled to be reproduced the other polymers. Moreover, P3HT:PCBM had been exhaustively research for its photovoltaic applications, possessing a rich scientific literature on its structure, morphology, chemical properties, and absorption characteristics [54]–[57]. However, little is known about its magnetic properties, allowing for potential scientific discoveries.

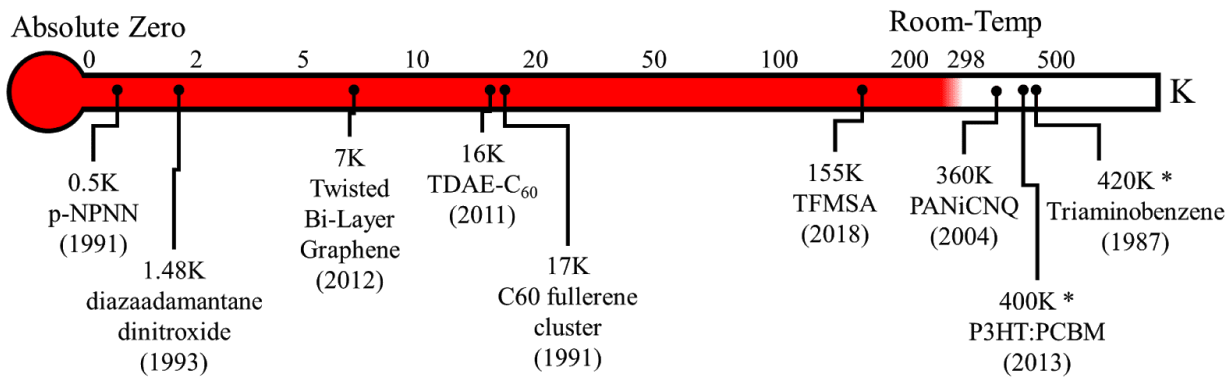

Figure 0-1: Organic ferromagnetic molecules and polymers with their associated Curie (or pyrolysis) temperatures.

The second half of this dissertation emphasizes P3HT:PCBM as an organic ferromagnetic material and its implementation in multiferroic composites. Chapter 4 is dedicated on the effect of fabrication techniques to achieve that greatest ferromagnetic response for these P3HT:PCBM blends while Chapter 5 looks to unveil some scientific questions about the physical origin of their magnetic behavior. The work on Chapter 4 and 5 developed colossal crystals of PCBM, which Chapter 6 is focused on their full property map characterization. The final chapter will discuss the potential of the two composites, Terfenol-D/PVDF-TrFE and P3HT:PCBM-PVDF, and their future perspectives.

Chapter 1 Synthesis and Characterization of Polarized Novel 0-3 Terfenol-D/PVDF-TrFE Composites

Scott Newacheck and George Youssef

1.1 Abstract

Conductive metallic particulate inclusions in electroactive polymer matrix composite have been widely studied for enhanced sensitivity applicable to sensors, energy harvesters, electromechanical actuators, and high charge storage capacitors. If the metallic particulates exhibit magnetostrictive properties, it expand the domain of application due to the direct and converse coupling between electric displacement and magnetization. In the paper, the synthesis of a composite material consisting of a giant magnetostrictive alloy particulates, Terfenol-D, embedded into an electroactive polymer matrix, PVDF-TrFE is discussed. The experimental protocol to elucidate the ferroelectric, dielectric, and piezoelectric properties of the novel composite is also reported. It was observed that the ferroelectric polarization was improved with a small weight fraction of Terfenol-D particles, but it was hindered when more weight fraction of the particles were added. Nonetheless, the permittivity of the composite rapidly increased with the addition of more Terfenol-D particles, which was attributed to the reduction in polarization of the PVDF-TrFE matrix. Finally, a notable phase delay was observed in the piezoelectric strain in response to a high frequency electric field, such a delay was directly proportionally to the addition of Terfenol-D particles.

1.2 Introduction

Smart materials intrinsically have coupling between two or more order parameters including strain, electric field, magnetic flux, or heat flux; to name a few, where a stimulus from one of these states results in an another state from a dissimilar physics. For examples, magnetocaloric materials couple magnetic to thermal energies by inducing a change in temperature in the presence of a magnetic field and triboluminescent materials illuminate in response to traction forces; or in other words couple the physics of mechanics to optics. In micro- and nanoscale actuation applications, smart materials with electromechanical (EM) properties were found to be an attractive option since it deforms with higher degree of precision than their mechanical counterparts in response to a low power electrical stimulus available in electronic devices. A subclass of EM materials is electroactive polymers (EAPs), which are more mechanically compliant resulting in mechanical strains 10-2500% higher than oxide-based piezoelectrics. Homopolymer polyvinylidene fluoride (PVDF) and copolymer PVDF with trifluoroethylene (PVDF-TrFE) are two EAPs that stably exhibit ferroelectric and piezoelectric behaviors, which extends their applicability into technological areas where the properties of remnant polarization and remnant strain in the absence of an applied electric field are imperative.[58]

Despite the prevalence of multi-field coupling in smart materials, as mentioned above, intrinsic coupling may be prohibited by the surrounding environment or the fundamental structure of the material, which in turn limits its integration in advanced applications requiring coupling at higher efficiency levels. A room-temperature stable smart material with intrinsic coupling between magnetic with electric properties eluded scientists for decades.[14] Alternatively, composite structures comprising of different types of smart materials can be engineered to achieve inter-field coupling with higher efficiency based on the effectiveness of the constituents at such operating conditions. The basic principle supporting the inception of composites of smart materials is

mediation or transfer through another state. In the area of magnetoelectric coupling, for example, spin-transfer, charge-mediation and strain-mediation have been shown to be effective in coupling electric and magnetic properties in heterogeneous structures with higher efficacy than their intrinsic monolithic counterparts.[14] To achieve the magnetic to electric coupling through strain mediation, composite multiferroics consist of piezoelectric and magnetoelastic materials that indirectly change magnetization in response to an applied electric field. These strain-mediated composite multiferroics for magnetoelectric coupling are being sought after for memory, antenna, and motor applications.[11], [59], [60]

In mediated composite multiferroics, the material properties of each of the constituents as well as the mediation mechanism play major roles in the effectiveness of the coupling. In the case of strain-mediated composite multiferroics, embedding magnetostrictive Terfenol-D alloy particulates into an electroactive PVDF-TrFE copolymer matrix to synthetize a new material system is hypothesized to yield enhanced magnetoelectric coupling coefficients. Nan et al. explained that the enhanced response of the ferroic composite is attributed to the giant magnetoelastic properties of Terfenol-D as well as the large piezoelectric properties and compliance of the PVDF-TrFE matrix.[44] While the 0-3 Terfenol-D/PVDF-TrFE composite was theoretically proposed nearly two decades ago, the practical realization of such composite was inhibited due to the difficulty to polarize the EAP matrix before electrical breakdown occurs due to the conductivity of the embedded Terfenol-D particles. The conductive inclusions induce electrical breakdown by providing a percolation path for the electric charge to pass through the structure, diminishing the applied electric field that is required to stimulate the EAP phase and ultimately nullifying the composite functionality as a whole. Therefore, this class of composites are limited to low volume fractions of magnetoelastic particles to overcome the percolation

problem by decreasing the probability for a pathway to incur. The size of Terfenol-D particles imposes an additional practical constraint on the realization of the 0-3 composite since it must be on the order of microns to retain magnetic properties. Recently, Cui et al. demonstrated a milling process of Terfenol-D particles, which could reduce the size down to a sub-micron scale while retaining its ferromagnetic properties. Hence, the milled Terfenol-D particles can be used as the magnetostrictive phase in 0-3 composite while overcoming the fabrication challenges.

It is then the subject of this article to report the synthesis, polarization and electrical characterization of 0-3 Terfenol-D/PVDF-TrFE composite, while observing the effect of that Terfenol-D inclusions on the electroactive properties of the PVDF-TrFE matrix.

1.3 Results and Discussion

1.3.1 Polarization of 0-3 Terfenol-D/PVDF-TrFE Composites

The polarization-electric field hysteresis loops for the neat PVDF-TrFE and each of the composite samples are shown in Figure 1-1, where the overall hysteretic polarization behaviors were found to be consistent but with a noticeable difference in the values. Table 1-1 summarizes the values of the coercive electric field (E_c) as well as the remnant (P_r) and maximum polarizations (P_m) of the 0-3 Terfenol-D/PVDF-TrFE composite samples in comparison with the properties of the neat copolymer. In all, the addition of 0.5 *wt.*% Terfenol-D has enhanced the polarization while 2 *wt.*% loading hindered both the polarization and electrical coercivity.

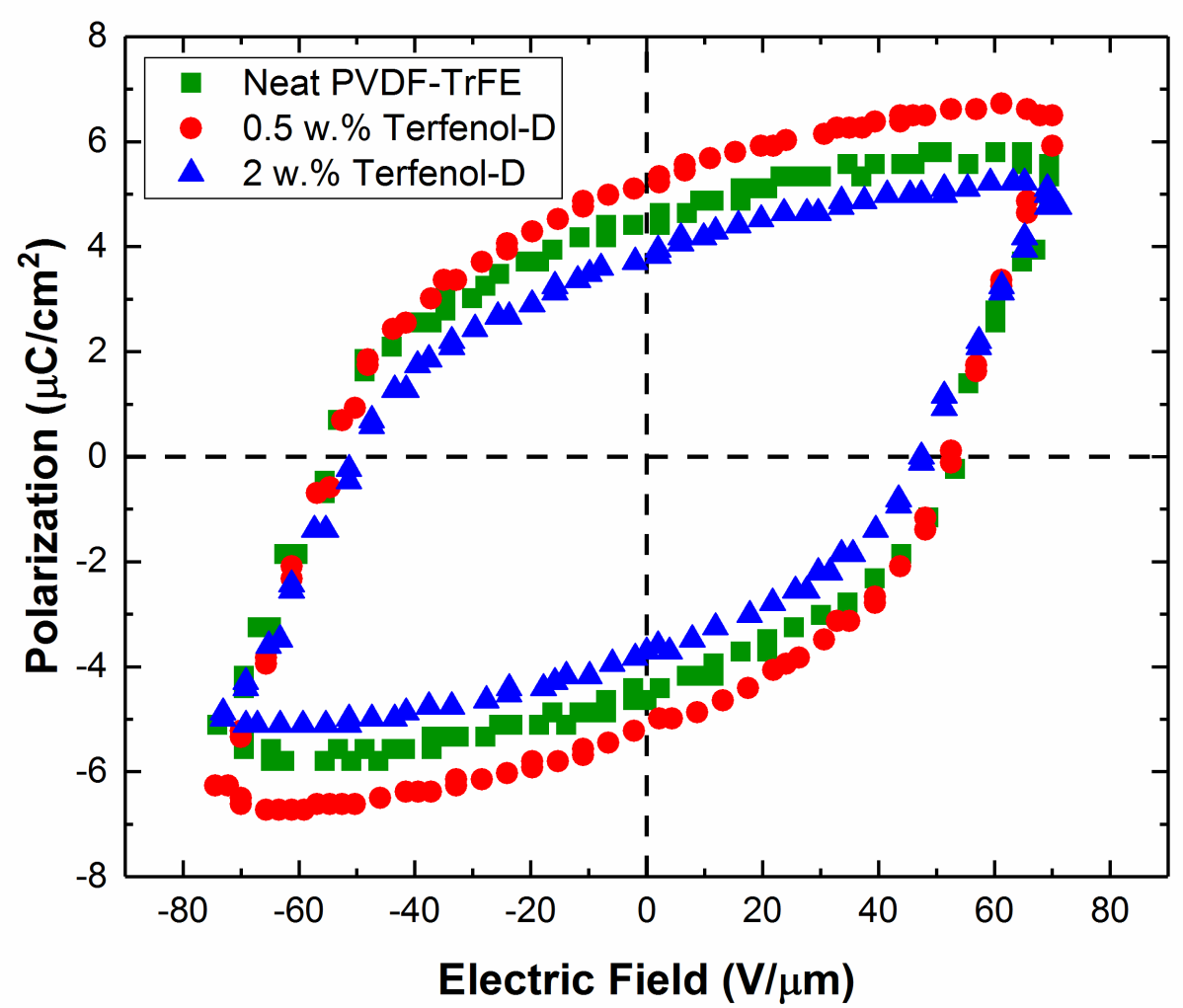

Figure 1-1: Polarization vs Electric field loops for neat, 0.5 wt.% and 2 wt.% Terfenol-D/PVDF-TrFE composites.

Enhancement in the polarization of the 0-3 composite with 0.5 *wt.*% Terfenol-D particles in comparison to the polarization of the neat copolymer samples is attributed to the conductivity of the magnetostrictive inclusions. Gan et al. reported a similar phenomenon in their composite materials consisting of <0.5 *wt.*% of conductive zinc-oxide particles embedded in a ferroelectric PVDF matrix[61]. The higher polarization was due to the effect of the conductive inclusions on increasing the applied electric field in the vicinity of the particles. The electric flux tends to favor areas of lower permittivity thus crowding near the interface between the electroactive polymer and

conductive Terfenol-D inclusions, which in turn reduce the electrostatic energy. Therefore, EAP material enclosed between Terfenol-D particles in proximity of one another undergoes a conformational transformation leading to locally higher polarization.[61] The collective increase in polarization in PVDF-TrFE entrapped between successive Terfenol-D particles leads in an overall enhancement in the polarization.

Although the conductive inclusions improve the electric field near the particles, they also act as impurities by hindering the potential of conformational order of the polymer matrix during the polymerization process. The PVDF-TrFE copolymer can assume different conformational phases, including α-, β-, and γ- phases based on the environmental, operating, and processing conditions during the polymerization process, where each phase holds different polarization capacity (Generally, $\beta > \gamma >> \alpha$).[62] Inclusions impurities increases the entropy during the polymerization process by disrupting the chain alignments and orders, which can be a source for changing the conformational phases. Such changes can explicate the differences noted in the polarization of the neat copolymers, 0.5 *wt.*% and 2 *wt.*/% Terfenol-D/PVDF-TrFE composite samples, of which the 0.5 *wt.*% composite samples reported the highest remnant and maximum values. The increase in the polarization can be attributed to an α to γ- phase transformation due to the Terfenol-D inclusion enhancing the electric field of the polymer matrix molecular structure as discussed before.[61] Whereas the decrease observed in 2 *wt.*% is due to the impurities interrupting and limiting the β -phase conformation.

1.3.2 Permittivity of 0-3 Terfenol-D/PVDF-TrFE Composites

Figure 1-2 displays the experimental results of the relative dielectric constant of the polarized samples as a function of frequency ranging from 20Hz to 40kHz. The dielectric constant, $\varepsilon_r = Cd/A\varepsilon_o$, was calculated based on the capacitance (C) measured across the top and bottom

surfaces using the LCR meter, the thickness (d), and the surface area (A) of the electrodes on each sample given that ε_o is the permittivity of free space ($8.854\times10^{-12}m^{-3}kg^{-1}s^4A^2$). The relative dielectric constant was found to exponentially decrease as a function of frequency, $\varepsilon_r(f) = Ae^{-f/\tau} + \varepsilon_\infty$, where f, τ, ε_∞, and A are the excitation frequency, relaxation time constant, the converging permittivity, and a curve fitting parameter, respectively. The fitting parameters obtained from curve fitting the results into this equation are also summarized in Table 1-1. Notably, the increase in the weight percentage of the conductive Terfenol-D inclusions resulted in a higher dielectric constant of the composite samples than that of the neat copolymer. Regardless of the frequency, the dielectric constant of 2 *wt.*% composite sample was found to be ~26% higher than that of the neat copolymer, while the dielectric constant of 0.5 *wt.*% was merely 1.5% higher when compared to the dielectric constant of PVDF-TrFE.

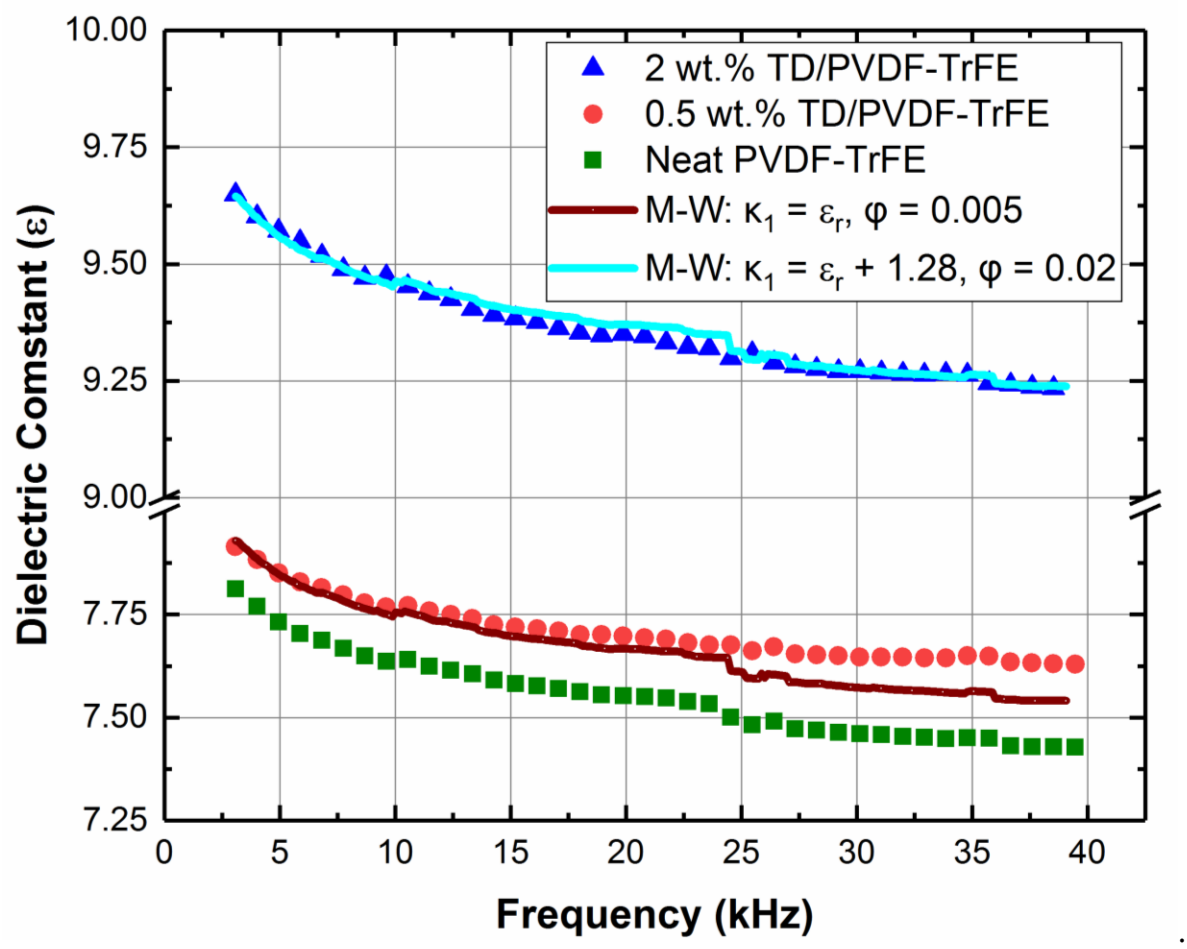

Figure 1-2: Experimental and predicted relative dielectric values for neat, 0.5 wt.% and 2 wt.% Terfenol-D/PVDF-TrFE composite as a function of frequency.

The effective permittivity (ε_{eff}) for composite materials with different volume fractions of Terfenol-D (φ) and the percolation threshold (φ_c) for 0-3 conductor-dielectric composite can be predicted with the Random Resistive Network (RRN) Model given by

$$\varepsilon_{eff} = \varepsilon_m \left(\frac{\varphi_c - \varphi}{\varphi_c}\right)^{-s} \tag{1-1}$$

where, ε_m is the permittivity of the neat sample and s is a curve fitting parameter valued between 0.27 and 1.46. In general, the value of the fitting parameters (φ_c and s) are highly dependent on

the fabrication process of the composite, the geometry and dispersion of the particles, and the material properties of the constituents. Previous research on 0-3 conductor-dielectric composite reported that the permittivity increases exponentially with an increasing volume fraction of the conductive particulate until the percolation threshold is reached. At which point, the composite no longer behaves as a capacitor, rather it becomes a resistor. Therefore, the conductivity of the embedded Terfenol-D particles contributes to the increase in the overall dielectric constant of the 0-3 composite Terfenol-D/PVDF-TrFE samples. The values of the percolation threshold and exponent associated with the RRN model for the Terfenol-D/PVDF-TrFE composites were found to be 35.7 *wt.*% and 1.16, respectively, when using relative permittivity values of the copolymer matrix 7.78 and 9.06 for the 0.5 *wt.*% and 2 *wt.*% composite samples. The rationale of the selection of these permittivity values becomes apparent in the proceeding discussion. It is worth noting that the percolation threshold reported herein is significantly lower than percolation limits for other material systems. For example, percolation thresholds of Nickel nanoparticles suspended in un-polarized PVDF-TrFE matrix was previously reported to be 60 *wt.*%. Such disparity of the percolation limit threshold can be attributed to the state of polarization of the matrix as well as the difference in the electrical conductivity of the fillers.

By further examining Figure 1-2, the addition of Terfenol-D micro-particles as the conductive filler to the PVDF-TrFE electroactive matrix act as a polarization barrier. This can be concluded by comparing the values of the dielectric constant of the different samples at 2.5 kHz, for example, which found to be 7.78, 7.88, and 9.51 for neat, 0.5 wt.% and 2 wt.%, respectively. It is worth noting that it had been reported that the dielectric constant for un-poled neat PVDF-TrFE is greather than that of polarized PVDF-TrFE[63]. For un-poled PVDF-TrFE, the dielectric constant is reported to typically range from 11 to 15.9, which is dependant on fabrication

conditions.[64] Regardless of where our un-poled samples would fall within this range, unpoled PVDF-TrFE has a dielectric constant 115-163% greater than that of the 2 wt.% and 141-203% greater than the polarized neat sample discussed herein. That is to say, increasing the conductive filler prevents the PVDF-TrFE electroactive polymer from reaching higher levels of polarization indicated by the higher dielectric constant in comparison to unfilled matrix, relating to the discussion in the polarization section. Therefore, in seeking an optimal weight ratio for the performance of these composite for magnetoelectric couple, two competing phenomena must be considered, namely percolation and reduction in dielectric constant, such that an increase in weight fraction of Terfenol-D will increase the magnetoelectric coupling but simultaneously compromises the dielectric constant of the electroactive matrix while approach the percolation threshold. As mentioned earlier, in search for such optimal ratio, the sample may change from an insulator to a conductor.

Finally, the effective dielectric constant of a composite consisting of a conductive filler in an insulator matrix can be predicted using a modified Maxwell-Wagner model

$$\varepsilon_{eff} = \varepsilon'_m \left[1 + \frac{3\varphi(\varepsilon_p - \varepsilon'_m)}{2\varepsilon'_m + \varepsilon_p}\right]\left(1 + \frac{\frac{9\varphi\varepsilon'_m}{2\varepsilon'_m + \varepsilon_p}}{1 + \omega^2\left(\frac{2\varepsilon'_m + \varepsilon_p}{4\pi\sigma}\right)^2}\right) \quad (2)$$

where, $\varepsilon'_m = \varepsilon_m + \zeta$ such that the value of ζ is bounded between 0 and 7 representing the partial state of polarization of the dielectric matrix material used herein. Taking 1.5×10^{16} e.s.u. for the conductivity (σ) of Terfenol-D and assuming a relative permittivity of 1000 for Terfenol-D, the predicted dielectric constant of the 0.5 *wt.*% of TD/PVDF composite was found to be in a good agreement with the measured values as shown in Figure 1-2. While performing the prediction for the 0.5 *wt.*% composite sample, the dielectric constant of the neat PVDF-TrFE was used since the matrix was considered to be fully polarized based on the comparison of our polarization values

with previously published ones.[65] However, as discussed earlier, the addition of Terfenol-D micro-particles inhibit the polymer matrix to reach the full state polarization, the value of the dielectric constant of the partially polarized matrix was iterated to predict the dielectric constant of the composite using the modified Maxwell-Wagner model for 2 *wt.*% samples. As a result, the addition of 2 *wt.*% of Terfenol-D micro-particles yielded a 82% polarization of PVDF-TrFE matrix. Thus, the modified Maxwell-Wagner model in conjunction with the protocol presented above can be used to experimentally determine the state of polarization in any conductor-dielectric composite.

1.3.3 Piezoelectricity of 0-3 Terfenol-D/PVDF-TrFE Composites

The applied electric field and the corresponding induced piezoelectric strains of the neat polymer and composite samples are plotted with respect to time in Figure 1-3. The negative piezoelectric nature of PVDF-TrFE is shown in Figure 1-3, where the strains have the opposite sense of the electric field. While the amplitude of the strains remains constant at $4.36\pm0.03\times10^{-3}$, regardless of the weight ratio of the Terfenol-D, the temporal response of the induced piezoelectric strains was found to lag with respect to the electric field. The time lag for the neat, 0.5 *wt.*%, and 2 *wt.*% composite samples were found to be 4.48, 4.51, and 5.40 μsec, respectively. Using the data from Figure 1-3, the complex piezoelectric coefficients ($d_{33}^{*} = d_{33}' + id_{33}''$) were calculated and summarized in Table 1-1.

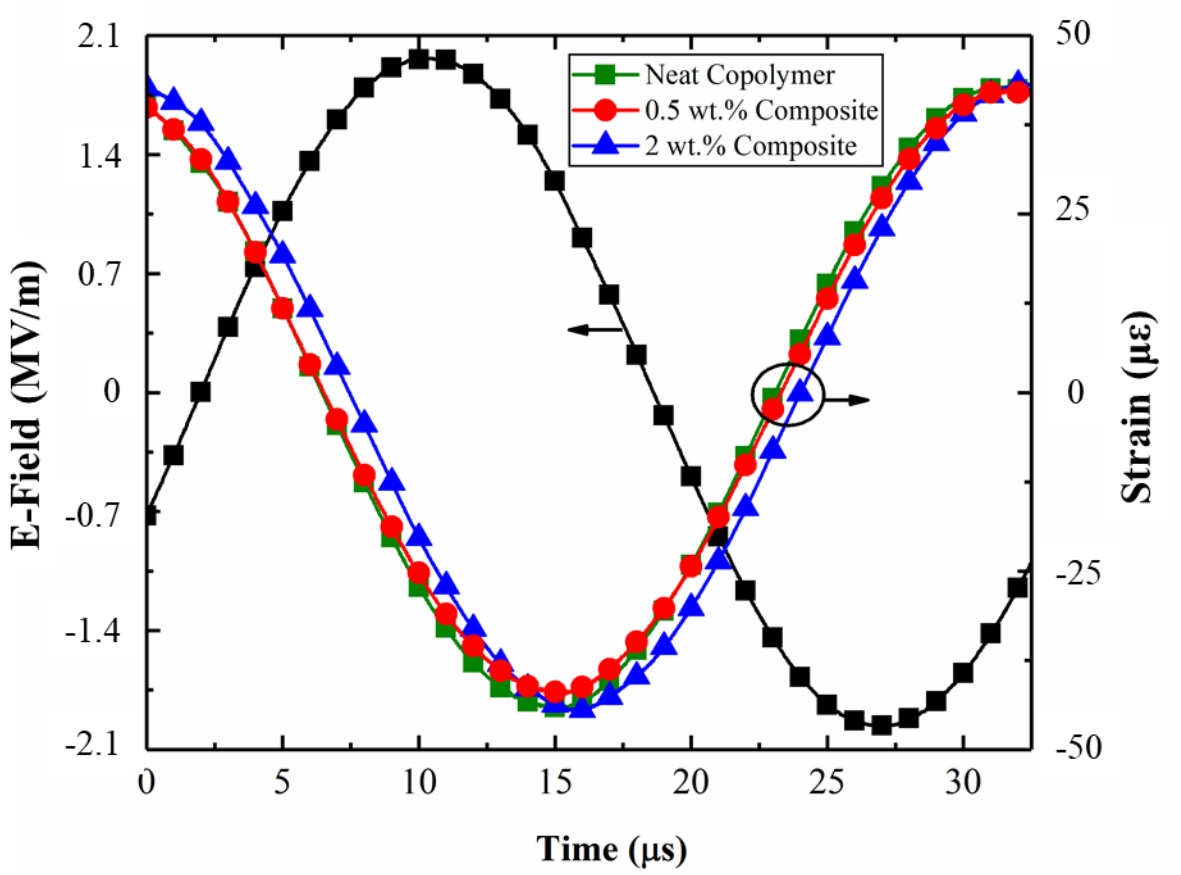

Figure 1-3: Induced piezoelectric strain of neat and conductive-dielectric composite showing the negative mechanical strain response based on properties of the PVFD-TrFE copolymer matrix.

The data suggests that the real and imaginary piezoelectric coefficients of the neat polymer and the 0.5 *wt.*% composite samples to be nearly identical, while the coefficients were drastically different for 2 *wt.*% loading of Terfenol-D. These results are congruent with those reported for the dielectric constant reported in the previous section. In general, the piezoelectric coefficients of a dielectric material are dependent on the state of polarization, where higher polarization is associated with higher coefficients. For example, the d_{33} piezoelectric coefficient of PZT when poled with an electric field of 1000V/mm are twice as large as when poled with an electric field of 750V/mm [66]. Since the Terfenol-D particles act as barrier to reach the full state polarization as discussed before, the overall electrically induced strain of these composites will be suboptimal for

strain-mediated magnetoelectric composite multiferroic. Nonetheless, since the strain generated is order of magnitude higher than the ceramics based piezoelectric materials, the transduced strain is expected to be higher resulting in higher magnetoelectric coupling[67]. This is a subject for future investigations.

The induced strains are shown to be constant regardless of the addition of the Terfenol-D particles with orders of magnitude higher elastic modulus than the matrix's modulus. At the first inspection, the strain results seem to be counterintuitive, however further investigation of the loading conditions in conjunction with the consideration of the actuator equation for linear piezoelectric materials support the validity of the experimentally observed data. According to the scaling laws ($Y_c = \varphi_p Y_p + (1-\varphi)_m Y_m$), the elastic modulus of the composite (Y_c) should lie between the moduli of the compliant matrix (Y_m = 2GPa) and the stiff Terfenol-D micro-particles (Y_p = 55GPa) depending on the volume fraction of each of these constituents (φ_p and φ_m, respectively). Therefore, the elastic modulus of the 0-3 Terfenol-D/PVDF-TrFE composite is 2.05GPa and 2.27GPa for the 0.5 *wt.*% and 2 *wt.*%, respectively, which implies lower mechanical strains as the volume fraction of Terfenol-D particles increases. Nonetheless, the samples investigated were under traction free boundary conditions and thus the recorded strains are only the results of the piezoelectric properties with no contributions of the mechanical stress, i.e., first term in $\boldsymbol{s} = S\boldsymbol{\sigma} + d\boldsymbol{E}$ is zero since no applied stresses are present. Nonetheless, the disparity in the elastic moduli of the PVDF-TrFE and Terfenol-D poses a challenge for the continuity conditions, hence may compromise the strain transudation at the matrix/particle interface and in turn may affect the efficiency of the magnetoelectric coupling. The effect of the difference in elastic properties on the effectiveness of 0-3 PVDF-TrFE and Terfenol-D composite warrants additional experimental investigations.

1.4 Conclusion

In closing, a novel 0-3 composite samples consisting of well-dispersed micro-particles of magnetostrictive Terfenol-D and PVDF-TrFE electroactive copolymer were synthesized and successfully poled overcoming challenges of percolation and electric breakdown experienced by previous researchers. The addition of Terfenol-D particle at low weight percentage (0.5 *wt.*%) was found to enhance the polarization of the electroactive matrix, however, further increase was found to be counterproductive. Such reduction of the polarization of the 2 *wt.*% Terfenol-D resulted in a larger permittivity, which was found to be a good agreement with predictions by the modified Maxwell-Wagner model. The enhancement of the permittivity of the polymer matrix due to the addition of Terfenol-D particles was consistent with behavior ascribed by the Random Resistive Network model. Finally, the piezoelectric-induced strain of the 0-3 composite samples lagged behind that of the neat PVDF-TrFE polymer without having a notable effect on the amplitude. Consequentially, the addition of 2 wt.% Terfenol-D to the PVDF-TrFE matrix has a notable increase in the dielectric constant while maintaining a similar piezoelectric response to that of the neat sample. In all, the data presented are the basis for future modeling and device innovations for strain-mediated multiferroic composite structures.

1.5 Experimental Section

Terfenol-D particles (Etrema Inc) with diameters ranging between 200 and 300μm were jar milled with heptane and oleic acid (Fischer Scientific) for 15 hours by closely following the process from.[68] Figure 1-4 emphasizes the effect of the jar milling process on the size of the Terfenol-D particles using a scanning electron microscope, where Figure 1-4a shows a micrograph of as-received particles and Figure 1-4b is an SEM image of a substantially reduced-size particles

after jar milling. Thereafter, the milled Terfenol-D particles were filtered through a 2-micron pore size paper sieve (VWR) to remove any remaining large particles. The particles that passed through the sieve were placed into a dimethyl formamide (DMF) solution, which was ultrasound mixed for 2 hours to disrupt any agglomeration of the particles. PVDF-TrFE pellets (Solvay Solvene 250) were added to the solution while the ultrasonic agitation continued for an additional 2 hours at 80°C. Finally, the solution was poured into a clean glass mold and placed in a vacuum environment at ambient temperature for 3 hours to eradicate voids, followed by a DMF evaporation process at 120°C for 2 hours. The process was repeated to make samples of 0%, 0.5% and 2% weight fractions of Terfenol-D. The final thickness of each sample was measured to be between 85 and 110 microns.

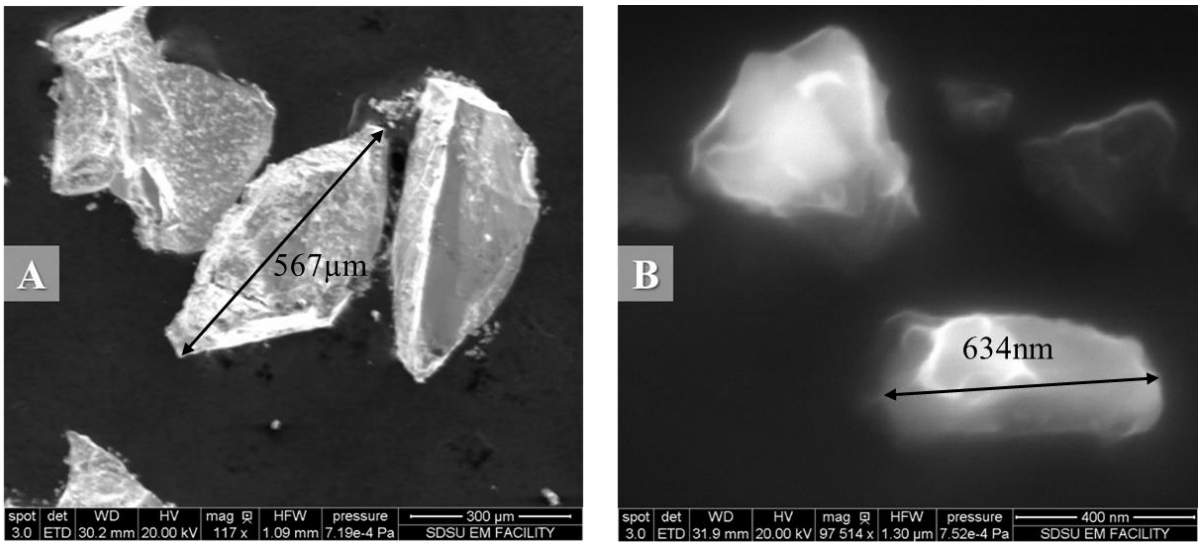

Figure 1-4: Micrographic comparison between Terfenol-D particles (A) before and (B) after jar milling.

The electroactive characterization protocol consisted of three steps to measure the polarization, piezoelectric strain and dielectric constant while an electric field was applied. In the first step, a 10 Hz, 150$V_{P\text{-}P}$/μm electric field was applied using an amplifier (Trek 609B) connected across the thickness of the sample that was submerged in silicone oil. The voltage across a Sawyer-Tower circuit was concurrently recorded using a digital oscilloscope (Tektronix DPO 2012b). The polarization versus electric field hysteresis loop was then plotted to quantify the coercive field, maximum polarization, and remnant polarization as well as to elucidate the effect of conductive Terfenol-D particles on the electroactive properties of the PVDF-TrFE copolymer. After the AC polarization data was collected, the sample was DC poled at 75V/μm for 4 minutes to ensure a remnant polarization persisted for subsequent steps. In the second step, the converse piezoelectric properties of the sample were characterized by applying a 2V/μm sinusoidal electric field with 30kHz frequency across the thickness while recording the piezoelectric induced displacement using a laser ultrasonic (BossaNova Tech, Tempo 2D). Finally, the dielectric constant of the sample was calculated from capacitance measurements using an LCR meter (BK Precision 891). These steps were repeated for 0-3 composite samples with different Terfenol-D weight fraction as well as neat copolymer samples.

Table 1-1: Properties of 0-3 Terfenol-D/PVDF-TrFE Composites

	Ferroelectric			Dielectric				Piezoelectric	
Sample	P_m $\mu C/cm^2$	P_r $\mu C/cm^2$	E_c V/μm	ε @ 3kHz	τ	A	ε_∞	d33' (pm/V)	d33'' (pm/V)
Neat	5.8	4.4	48	7.78	21.624	0.478	7.350	14.5	16
0.5wt.%	6.7	5.5	48	7.88	12.922	0.346	7.616	14.3	16
2wt.%	5	3.24	40	9.51	14.590	0.509	9.208	11.5	19

1.6 Acknowledgements

Chapter 1, in full, is a reprint of the material as it appears in Composites Part B: Engineering, 2019. Youssef, George. The dissertation author was the primary investigator and author of this paper.

Chapter 2 Microscale Magnetoelectricity: Effect of Particles Geometry, Distribution, and Volume Fraction

Scott Newacheck and George Youssef

2.1 Abstract

Achieving efficient magnetoelectric coupling of core-shell and particulate multiferroic composites has been a challenging hurdle; however, research has shown unwavering interest to overcome this barrier in pursuit of their implementation into promising potential applications. Herein, a fully-coupled computational model of core-shell and particulate composites is developed and verified to investigate the magnetoelectric interactions of the particle and matrix on the microscale. The effects of particle geometry, settling, and agglomeration were exhaustively studied by investigating seven different shapes and a wide range of vertical and lateral particle spacing. Overall, it was found that utilizing particle geometries and positioning that closely resemble a laminate configuration, such as a prolate ellipsoid and horizontal particle alignment, enhances the magnetoelectric coupling of the composite structure. The results coincided with the experimental results concerning settling and agglomeration.

2.2 Introduction

As scientific advancement continues, the incentives for replacing electromagnetic technology with magnetoelectricity, i.e., the coupling of polarization and magnetization, become increasingly popular. Magnetoelectricity has many enticing advantages linked to voltage-controlled magnetism, contrary to electromagnetism that is current-dependent. For example, switching from current-based to voltage-based technology substantially reduces the energy requirements, relief of joule heating, and aptitude for nanoscale adaptation [1]. Nevertheless, magnetoelectricity still has shortcomings slowing its widespread implementation, stemming from its scientific infancy compared to electromagnetism. These disadvantages include a limited range of magnetic fields and the directionality and state of magnetism, which are being relieved by the aggressive research efforts on magnetoelectricity [2], [3]. A significant enabler for researchers to overcome these challenges is the diverse mechanisms to achieve magnetoelectric couplings, such as intrinsic multiferroic, strain-mediated composite, and charge-transfer composite materials [4]. For example, the charge-transfer coupling mechanism was exploited to switch the state of magnetization, while strain mediation was used to extend the utility of magnetoelectric structure in a high magnetic field [2]. Although each magnetoelectric coupling mechanism has its merit, strain-mediated composites are one of the most scientifically exciting mechanisms granted by a large selection of materials, limitless potential geometries, and highly customizable configurability [5].

The material system required for strain-mediated magnetoelectric coupling primarily consists of piezoelectric and magnetostrictive constituents arranged in various forms and configurations [6]. Piezoelectric materials intrinsically couple polarization with strain, while magnetostrictive materials couple strains with magnetization [7], [8]. Although many types of magnetostrictive and piezoelectric materials exist, they almost all belong to metals or ceramics,

except for a few piezoelectric polymers [9]. Notably, this means a majority of strain-mediated magnetoelectric composites are brittle and rigid. Regarding composite configurations, the most popular are particulate-matrix, stack laminate, rod-matrix, and core-shell, also referred to as 0-3, 2-2, 1-3, and pseudo-1-D, respectively [5]. Each configuration has different benefits; such as 2-2 composites being highly studied and easily modeled [10]–[17]. However, a key advantage of the 0-3 composite structure is its potential to be soft and flexible, positioning them for applications in passive tactile sensors, wearable technology, and soft robotics [18]. By embedding magnetostrictive particles into a polymeric piezoelectric matrix, the mechanical properties of the composite material would mainly adopt the matrix properties, which can be orders of magnitude more compliant than ceramics- or metal-based magnetoelectric composites [19]–[21]. There is a need for scientific attention to enhance the magnetoelectric coupling of soft 0-3 composites since their performances have been orders of magnitude lower than the brittle 2-2 composite counterparts. Although 0-3 composites are often predicted to yield 'giant' magnetoelectric coupling through analytical models, experimental results usually fall short to meet those analytical expectations [22]. The discrepancy between analytical and experimental results is attributed to the neglect of the fabrication effects (e.g., particle settling and agglomeration, electrical percolation, alteration of material properties) and oversimplified assumptions of the analytical models.

Two of the most debilitating limiters for 0-3 composite materials imposed on them during fabrication are the percolation of the magnetic particles and the dielectric breakdown of the piezoelectric matrix [23]. The size of the magnetostrictive particles must be kept much smaller than the thickness of the matrix to remedy the percolation issue, and the volume fraction of the particles should be minimized (theoretically less than 30%) to avoid path connectivity [23]. Most investigated 0-3 composites take the form of thick films at a thickness of a few hundred microns;

therefore, the size of the particles must be limited to less than a few microns. Several magnetic particles were studied, including CoFeO, NiZnFeO, and Terfenol-D, since they can attain the size limit and retain their magnetic properties [24]–[26]. A byproduct of the size reduction process (e.g., jar milling) is the non-uniform geometry, resulting in particles with jagged edges and flat surfaces [27], [28]. The rotating ball mills cleave the brittle magnetic particles due to the localized impact between the former and the latter as the milling process takes place [27]. Figure S1a shows scanning electron micrograph milled Terfenol-D particles signifying the sharp edges at cleaved surfaces. It is worth noting that the geometry of the particles constitutes another deviation between the experimental and analytical results, where the latter commonly simplify the particle to spherical or ellipsoidal shapes [22]. On the other hand, the dielectric breakdown is associated with the piezoelectric matrix, which can be made of polymers such as cellulose, polyvinylidene fluoride (PVDF), and copolymers such as trifluoroethylene (TrFE) [26], [29]. The fabrication process of Terfenol-D/PVDF-TrFE composites is prolonged over a few hours, where the PVDF-TrFE change from the liquid to the solid phase. Terfenol-D particles may settle during processing because of the disparity between the physical properties of the particle and the matrix. The settling may result in particle agglomeration, affecting dielectric breakdown (Figure S1b and S1c).

The research leading to this paper aimed at explicating the interactions of the constituents, leading into insights into the mechanisms responsible for the magnetoelectric coupling in Terfenol-D/ PVDF-TrFE composite materials. Specifically, a finite element method was employed to model the magnetoelectric behavior of particulate polymer matrix composite materials while minimizing potential oversights. The flexibility of the computational framework allows the investigation of material behaviors that are otherwise unachievable with current analytical models. In our computational model presented below, the particle geometry, orientation, volume fraction, and

particle-to-particle interactions can be modeled and exploited for magnetostrictive and piezoelectric couplings. The efficacy of the magnetoelectric coupling hinges on the intrinsic interactions between strain, electric field, and magnetic field, which was recently shown to have notable contributions and should not be disregarded [30]. In short, the outcomes of this computational unveiled microscale effects and offer strategies to enhance the magnetoelectric coupling of magnetostrictive particulate piezoelectric polymer matrix composite materials.

2.3 Particulate Multiferroic Computational Model

At its essence, a 0-3 composite material can be visualized to consist of a single (or a collection) magnetic particle surrounded by a piezoelectric polymer matrix; hence, a representative element volume (REV) was computationally modeled to investigate the microscale behaviors of this fundamental unit. The shape and dimensions of the particle were varied to investigate their associated effects, as discussed next, while the matrix was assumed to be a cube with different dimensions to elucidate the magnetoelectric response as a function of the volume fraction (φ). The particle volume was chosen to be small enough to satisfy experimental requirements and large enough to ignore micromagnetics. A Multiphysics simulation (COMSOL® 5.3a) was built to couple the physical domains of electrostatics, magnetics, and mechanics.

2.3.1 Particle Geometry

The spherical particle geometry is ubiquitous in the analytical modeling approach of particulate magnetoelectric composites since it lends itself to many simplifying assumptions; see Nan *et al*. [22]. Therefore, the first set of simulations was based on a spherical particle with 2 μm diameter, where the size was based on prior experimental observations to prevent dielectric breakdown and electrical percolation. The volume of the PVDF-TrFE cube was first set to $8/3\pi$ μm^3 then was changed to $8000/3\pi$ μm^3 in logarithmic increments of 10 steps per decade,

representing a change in the volume fraction ranging from 0.2% to 50%. The upper bound of the volume fraction was based on the particle-packing factor, complete containment without tangency of the conductive particle to the sides of the cube, and the computational stability of the model. It should be noted that the maximum volume fraction in experiments is often below 16% to prevent the dielectric breakdown of the matrix through percolation.

The shape of the magnetic particle gives rise to intricate interactions between the bias magnetic field and the resulting state of magnetization, including the stray field emanating from the particle continuum. These complex interactions are commonly smeared in analytical modeling since the approach hinges on effective media response or, in other words, the homogenized response. Here, four additional geometries were considered to elucidate the effect of the particle shape on the resulting magnetoelectric coupling coefficients, including ellipsoidal, cube, octahedron, and dodecahedron. The consideration of such a broad range of particle geometries (ranging from spherical to dodecahedron) signifies an additional novelty of this research. In the case of the ellipsoidal geometry, the aspect ratio (AR) was changed to sweep the form of the particle from a disc (AR=0.25) to a rod (AR=2), which inclusively represented two additional composite configurations, namely quasi 2-2 and 1-3, respectively. Analogously, the magnetoelectric response was hypothesized to depend on the relative orientation of the platonic geometries with respect to the direction of the bias magnetic field; henceforth, the alignments of an edge, a surface, or a vortex with the bias field were also investigated. Regardless of the particle geometry, the particle volume was held constant at $4/3\pi\ \mu m^3$, congruent with the spherical particle volume.

The flexibility of computational modeling, using the fundamental unit approach of 0-3 composite material (i.e., REV), was utilized to explicate the particle-to-particle interaction

encompassing the magneto-mechano-electric correspondence in the vicinity of each particle. Specifically, the number of REVs (2 vs. 4), lateral and axial stacking configurations, and the particle distribution were investigated to elucidate their individual and combined effects on the resulting magnetoelectric coupling coefficient.

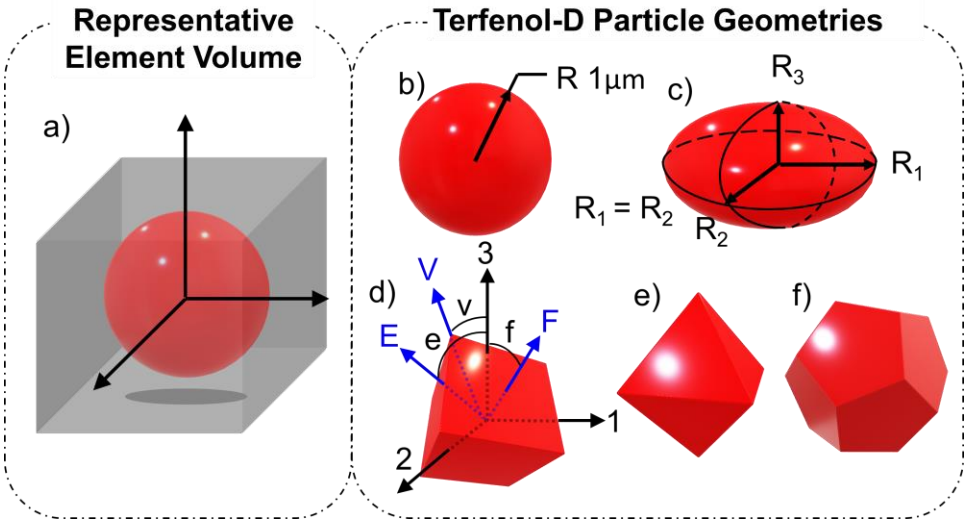

Figure 2-1: (a) schematic representation of the representative element volume (REV) with PVDF-TrFE matrix surrounding a spherical Terfenol-D magnetic particle. The REV is (a) was used to benchmark and validate the results of the computational model. (b-f) Five different particle geometries investigated herein to elucidate the effect of geometry on the magnetoelectric coupling coefficient. The inclusion of platonic geometries is inspired by the effect of physical sample preparation process as discussed in [26].

2.3.2 Material Modeling

The behavior of the PVDF-TrFE matrix was modeled using a transverse isotropic linear constitutive relationship in the stress-charge form (Equation 2-1) since it was able to capture the electromechanical response satisfactory.

$$D = eS + \varepsilon_S E\ , \qquad T = c_E S - e^T E \tag{2-1}$$

Where, D, T, S, and E are the electric displacement, stress, strain, and electric field, respectively, c_E is the stiffness at constant electric field, e is the piezoelectric coupling factors, and ε_S is the permittivity at constant strain. The linear piezoelectric model was found to be sufficient for the

scope of the study; however, future research can extend the applicability of this computational analysis to include nonlinear piezoelectric, e.g., Langevin function, and time-dependent mechanical behavior, i.e., viscoelasticity. On the other hand, the magneto-mechanical response of the Terfenol-D particle was described using nonlinear isotropic magnetization and magnetostrictive models to mimic the experimental behavior best. The stresses from mechanical strain (S_{el}) and magnetostriction (S_{me}) within the magnetic particle was calculated using

$$T = Y_H[S_{el} - S_{me}(\boldsymbol{M})] \tag{2-2}$$

where, Y_H is the Young's modulus. It is important to note that the emphasis here is on elucidating the magnetic shape anisotropy and particle distribution and their effects of the magnetoelectric coupling. Future research focusing on anisotropic elastic response may consider replacing the Young's modulus in Equation 2-2 by the second order elastic constants (beyond the scope of the current study). The magnetostriction is a function of the magnetization given by

$$S_{me} = \frac{3\lambda_s}{2M_s^2} dev(\boldsymbol{M} \otimes \boldsymbol{M}) \tag{2-3}$$

where, λ_s and M_s are the magnetostriction and magnetization at saturation. To model the magnetization (Equation 2-4), the Langevin model was employed in its nonlinear form.

$$\boldsymbol{M} = M_s \left[coth \frac{3\chi_m |\boldsymbol{H}_{eff}|}{M_s} - \frac{M_s}{3\chi_m |\boldsymbol{H}_{eff}|} \right] \frac{\boldsymbol{H}_{eff}}{|\boldsymbol{H}_{eff}|} \tag{2-4}$$

Where, χ_m is the initial magnetic susceptibility and the effective magnetic field is given by

$$\boldsymbol{H}_{eff} = \boldsymbol{H} + \frac{3\lambda_s}{\mu_0 M_s^2} T_{dev} \boldsymbol{M} \tag{2-5}$$

where, μ_0 is the permeability of free space. The second term of Equation 2-5 is the magnetoelastic contribution, i.e., the effect of the mechanical stress on the induced magnetic field. Finally, the interface between the particle and surrounding matrix was assumed to be a perfect bond, in other words, the displacement is identical for each material at the interface. This assumption can be

relaxed in future studies to explicate its influence on the coupling efficacy. The material properties used in the simulations are listed in Table S1.

2.3.3 Boundary Conditions

The only imposed mechanical boundary condition was fixing three corners of the PVDF-TrFE cube to prevent rigid body motion, where two corners were completely restrained in two directions while the remaining corner was prevented from moving in all directions. The entire bottom surface of the cube was prescribed as an electrical ground, while the particles were considered perfect electrical conductors such that they exhibit no electric field gradient. A bias magnetic field was applied in the z-direction with a magnitude of 0.03 T. The average voltage on the top surface was measured and was used to calculate the direct magnetoelectric coefficient (DME) by taking the ratio of the average voltage and the product of the applied magnetic field and composite thickness ($\alpha = V/tH$). The spatial discretization for each particle geometry and composite configuration is discussed in the Supplementary Material (Table S2).

2.4 Model Validation

Before embarking on utilizing the computation framework to elucidate the magnetoelectric response of 0-3 composite material, it is imperative to validate its performance with other established analytical and experimental approaches. For a single REV with a spherical particle, the computational DME coefficient was calculated to be 0.39 V/A. Nan *et al*. analytically reported a DME coefficient of 0.58 V/A for the same configuration, where both were solved for $\varphi = 0.10$ [22]. The DME from our computational framework was considered to agree with the previous analytical results considering two differences. First, the material properties of the magnetic particles used in the analytical model were more than twofold higher than the commonly known attributes of Terfenol-D used herein and in the broader body of literature. Second, the

dimensionality of the analytical model was restricted to a 2D homogenized formulation, while the computational model was a 3D full-field simulation. The agreement in the DME prediction constitutes the first aspect of validation.

The second point of validation is based on the experimental results of a similar composite material characterized in the converse magnetoelectric coupling paradigm (see Supplementary material). Experimentally, the converse piezoelectric coefficient was found to be insensitive to the addition of small fractions of Terfenol-D particles (below 2wt.%). The difference between the experimental piezoelectric coefficient for 0.5wt.% and 2wt.% composites was found to be 3.3%, which agreed with the computational results, showing a difference of 0.5% for the same conditions. Nonetheless, such small volume fractions of the magnetic particles had a pronounced effect on the polarization and mechanical responses of the piezoelectric polymer matrix. Specifically, the addition of the conductive magnetic particles resulted in electric field localization, hence improving the polarization by 108.6% (in the experiment) when comparing neat PVDF-TrFE to the 0.5 *wt.*% TD/PDVF-TrFE composite [26]. The embedded particles acted as intermittent electrodes throughout the thickness of the polymer matrix, resulting in a higher local electric field between successive particles and a higher state of polarization [31], [32]. The computational results were able to replicate these effects by calculating a 106% polarization enhancement with the inclusion of Terfenol-D, as illustrated in Figure S3.

2.5 Results and Discussion

The structure of the following subsections reflects the research steps taken to elucidate the interrelationship tying the magnetoelectric coupling performance of particulate multiferroic composites to the arrangement and configuration of the magnetic particles within the electroactive polymer matrix. The reductionist approach adapted herein using computational investigations

provided a pathway to decouple the contribution of several variables, including the volume fraction, particle geometry, stacking configuration, and particle arrangement. The outcomes of each subsection substantiate the rationale for subsequent sections, culminating the overall objective of this research study.

2.5.1 The Effect of Volume Fraction

The interplay between electric and magnetic energies via strain mediation in 0-3 composite materials implies a highly nonlinear magnetoelectric coupling coefficient as a function of the magnetic filler content. Here, a simplified or homogenized rule of the mixture cannot capture the correct response for the entire range of volume fraction. Figure 2-2a shows a comparison between the predicted DME response using the computational framework presented above and the analytical results of Nan *et al*. [22] as a function of the volume fraction of the spherical Terfenol-D particles. The computational results elucidate the nonlinear dependence of the DME on the content of the conductive magnetic particles while signifying two transition points at $\varphi = 0.08$ and $\varphi = 0.30$, at which a reversal in the DME trend is observed. The computational DME exhibits a quasi-linear increase to $\varphi = 0.08$, reversing to a downtrend behavior until the volume fraction reaches 0.30, followed by an uptrend until the end of the investigated range. The results from Figure 2-2a show that the analytical model below $\varphi = 0.06$ under-predicted the DME coefficient; thereafter, it over-predicted the response.

The evolution of the computational DME response as a function of the volume fraction is elucidated by examining their magneto-mechano-electric distributions within a REV unit, plotted in Figures 2-2b-f with an increasing volume fraction of the magnetic particle. The amplitude and coherence of the magnetic flux show a monotonic increase as the volume fraction of the Terfenol-D particle ascends due to the proximity of the particle to the observation surface (i.e., top

electrode). Otherwise, the magnetic flux distribution is nearly identical regardless of the volume fraction, which is attributed to the applied bias magnetic field corresponding to the magnetic saturation of Terfenol-D. On the other hand, the evolution of the strain field within the particle mirrors the behavior of the DME effect shown in Figure 2-2a, where the strain initially increased from 164 ppm to 517 ppm as the volume fraction ascended from 1% to 14%, respectively. This initial strain change is also signified through the increasing spread of strain through the matrix, as shown in Figure 2-2b-e. Thereafter, the strain appears to decrease before reaching a maximum at φ=0.5, but the strain distribution evolved into a highly localized case for the final volume fraction. A substantial change in the electromechanical response is observed between $\varphi = 0.14$ in Figure 2-2e and $\varphi = 0.42$ in Figure 2-2g. The unique electric potential behaviors at different volume fractions are related to how the magnetostrictive particle alters the mechanical strain within the piezoelectric matrix. At volume fractions within the first increasing region ($\varphi < 0.08$), the lowest electronegative response on the measured surface lies directly above the particle, as illustrated in Figures 2-2b-d. In the presence of a magnetic field, the Terfenol-D particle elongates in the axial direction and shrinks in the lateral direction due to the Poisson's effect. In turn, the lateral contraction of the Terfenol-D particle induces a tensile strain on the top surface while the matrix material under the surface is squeezed between the taut top surface and the elongated particle. At $0.08 < \varphi < 0.3$, the elongating magnetic particle occupies a larger portion of the REV while reducing the piezoelectric material entrapped between the top surface of the particle with the top electrode, or in other words, making the particle closer to the surface. Hence, the presence of the particle due to the magnetostriction effect changes the strain distribution on the top surface resulting in a lower electromechanical response, explicating the downtrend of the DME. This tread continues until the second and final inflection point (i.e., $\varphi = 0.3$), where the particle becomes

increasingly close to the measurement surface such that the compressive strain due to the elongation of the particle overcomes the effect of the tensile surface strain resulting in another region of increased DME.

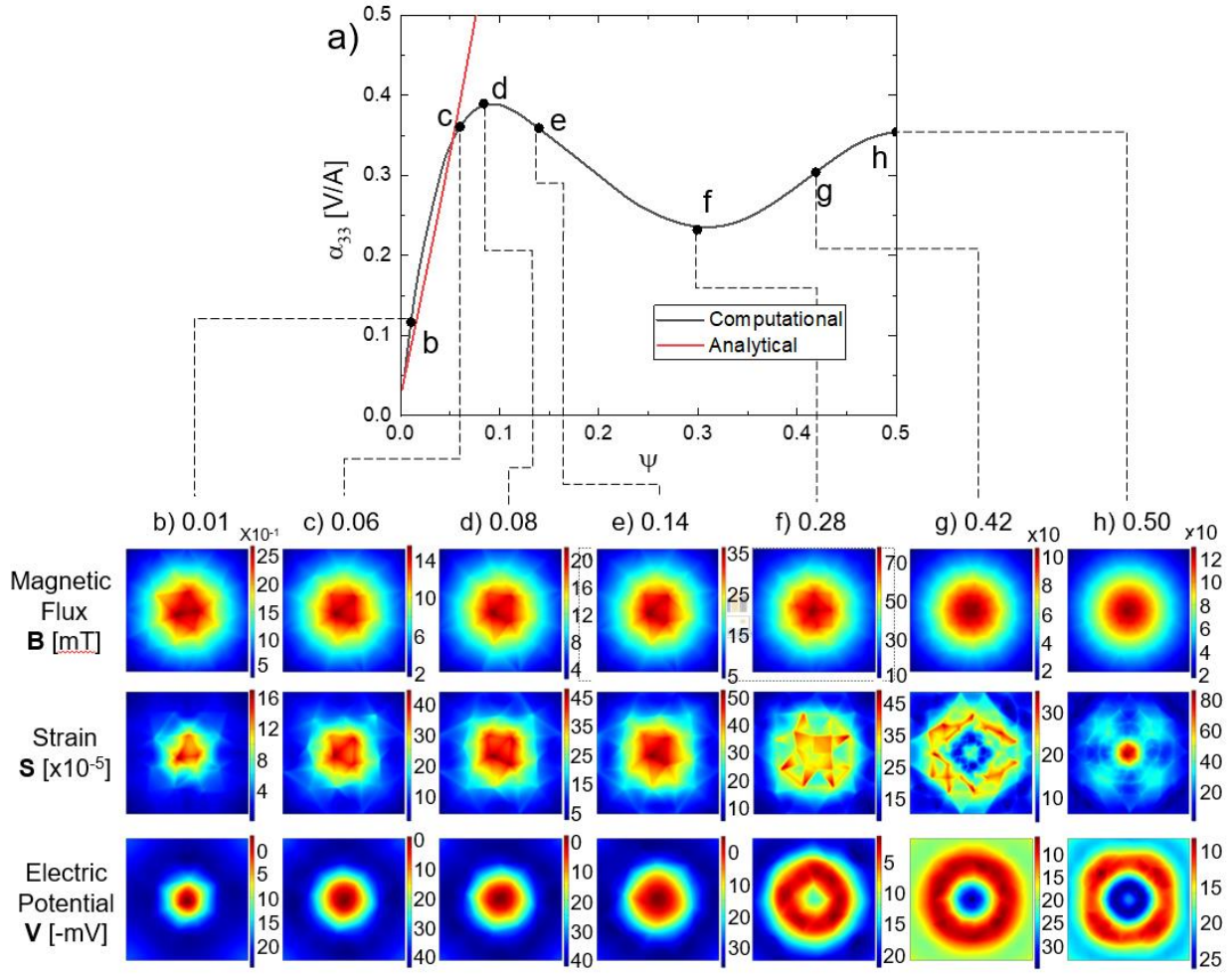

Figure 2-2: (a) Comparison of the analytical and computation direct magnetoelectric coupling coefficient with respect to the volume fraction of the Terfenol-D phase. (b-h) Contour plots of the magnetic flux, strain, and electric potential distributions observed from the top surface of the REV, showing the effect of the volume fraction on the distribution of these parameters and on the resulting DME. The results exemplify an optimal volume fraction for this type of magnetoelectric composites.

2.5.2 The Effect of Particle Geometry

Due to the jar milling process, the non-uniform geometry of the magnetic particles is expected to play a significant role in the overall magnetoelectric response. In lieu of the digitization of the numerous resulting particle geometries from electron micrographs, parametric shapes of centrosymmetric and non-centrosymmetric characteristics were selected to elucidate the interrelationship between geometry and response. The volume fraction corresponding to the maximum reported DME (10%) is utilized throughout the discussion based on the preceding

results. The spherical particle geometry is the centrosymmetric shape, while the remaining geometries (ellipsoid, cube, octahedron, dodecahedron) are non-centrosymmetric. Figure 2-3a shows the numerical simulation results as these geometries were situated within the REV in a nominal orientation, generally at f = 0. The magnetoelectric voltage was 39.01 mV for the spherical particle, while voltages of 47.4, 70.4, 56.8, 46.6 mV were calculated for prolate ellipsoid, cube, octahedron, dodecahedron, respectively. The increase in the number of surfaces of the filler particle in direct view of the top electrode results in a decrease in the DME response. For example, the dodecahedron with six faces facing the top electrode has an average response that is 33.8% less than the average response of the cube with only one face directly opposing the top electrode. Therefore, the sphere elicits the least DME response as it has an infinite number of faces. This is attributed to the change in the charge accumulations on the top electrode as the spatial variance between the top electrode and the viewing surfaces of the particle monotonically increases (e.g., compare cube to a sphere). Additionally, the results plotted in Figure 2-3b demonstrate the sensitivity of the DME response to the rotation of the particle geometry about the 3-direction. The DME response of the spherical particle is rotation-independent about the 3-axis due to the centrosymmetry, while the platonic geometries of the magnetic particles are sensitive to such rotation. For example, the DME voltage of the cube particle varied between 70.63 mV and 59.4 mV as the particle rotated to 45° around the 3-direction while maintaining f = 0. On the other hand, the DME response becomes less sensitive to rotation around the 3-direction as the dimensionality of the geometry facing the top electrode decreases (face to edge to vertex).

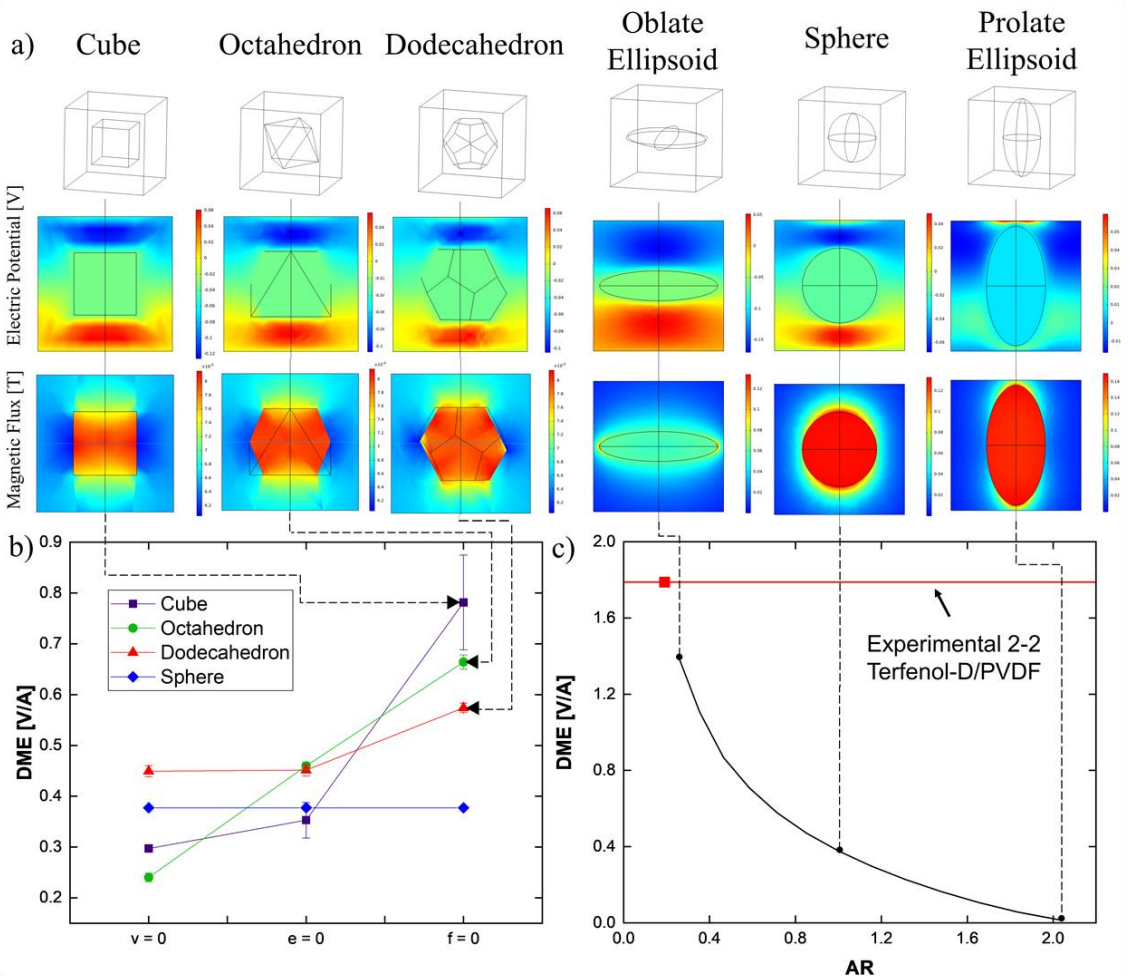

Figure 2-3: (a) The sectional distribution of the electrical potential and magnetic flux distributions for sphere, oblate ellipsoid, prolate ellipsoid, cube, octahedron, and dodecahedron shaped Terfenol-D particles. (b) The DME for the platonic geometries for f = 0 (face align with the direction of the magnetic field), e = 0 (edge align with the direction of the magnetic field), and v = 0 (vertex align with the direction of the magnetic field). Face-aligned geometries yielded the highest direct magnetoelectric coefficient. The error bars plot the variance for different particle rotations about the 3-direction. (c) Direct magnetoelectric coupling of the REV as a function of the aspect ratio of the ellipsoidal particle, showing excellent agreement with previous experimental results [33]. The red square represents the AR when the oblate ellipsoid would protrude the sides of the matrix to be a 2-3 composite by definition.

Remarkably, the ellipsoidal geometry sheds a unique perspective regarding the effect of the surfaces in the direct view of the top electrode, consistent with the standing notion concerning the performance of the magnetoelectric composite materials [4]. As discussed above, when the

ellipsoid is at the nominal orientation with an aspect ratio of 2.02, representing a rod surrounded by the PVDF-TrFE matrix (pseudo 1-3 configuration), the DME value is 410% smaller than the opposing orthogonal orientation. In the latter, an ellipsoid with an aspect ratio of 0.25 (representing a disk in the middle of the REV) reported a DME of 1.944 V/A, signifying a pseudo 2-2 configuration (officially a 2-2 configuration when AR = 0.191) and closely predicting the response of a 2-2 composite of a Terfenol-D/PVDF composite reported in [33]**.** Moreover, this reported behavior is in excellent agreement with prior experimental studies of 0-3, 1-3, and 2-2 magnetoelectric composite configurations [5], [34], where the latter consistently yields the highest magnetoelectric coupling coefficient for the same material system. For example, experimental values for 0-3, 1-3, and 2-2, Terfenol-D/PZT composite reported non-resonant DME responses of 30, 399, and 4720 mV/A, respectively [5], [34]. Moreover, the change of the aspect ratio of the ellipsoid signifies the physical phenomena responsible for the DME response shown in Figure 2-3c. At AR = 1, the ellipsoid becomes a spherical geometry where the response is in good agreement with previous results presented above. However, as the AR increases, the DME coefficient descends at a rate of 1.07 to nullify the response as AR $\rightarrow$ 2.08, where the slender ellipsoid pierces through the electrodes creating a conductive path, hence negating the direct magnetoelectric effect. At this AR, the particle acts as a percolated conductive path, neutralizing the voltage distribution across the top and bottom surfaces. Alternatively, the AR below unity decrease indicates a change in the ellipsoidal geometry to a pancake situated in the middle of the REV, as discussed before. It is important to note that a percolated conductive path is ineffective and undesirable for magnetoelectric applications for two reasons. First, the conductive path will electric current to path through the composite, deeming the magnetoelectric structure as a resistor, where the value of which would dictate the amount of energy loss through Joule heating. Second, while the

conductive path carrying an electrical current can also be used to generate magnetic field (i.e., traditional electromagnetic paradigm), the magnetic field strength is expected to be weak with negligible magnetostriction, hence, the electroactive polymer is merely an adhesive. As indicated, a conductive path is detrimental to the operation of magnetoelectric composites.

2.5.3 REV stacking- Composite Configuration

The concept of the REVs was used to demonstrate the overall response of a 0-3 composite by stacking two fundamental units into two configurations, namely vertically (*2v*-REV) and laterally (*2h*-REV). Figure 2-4 shows the magneto-mechano-electric behavior of vertically and laterally stacked REVs with $\varphi = 0.1$ by plotting the magnetic flux and electric potential distributions with deformation superimposed on both contour plots (scaling factor of 300). The DME coefficients for a single REV, *2v*-REV, and *2h*-REV magnetoelectric composite were 392.7, 118.7, and 646.6 mV/A based on the average electrode voltage of 32.0, 19.7, 53.6 mV, respectively, and a bias magnetic field of 300 mT. Intriguingly, the vertical stacking tarnishes the resulting DME, while the horizontal layout was found to be beneficiary with a 547% increase in the response over its vertical counterpart. The interaction of the bias magnetic field and the arrangement of the particles within the 0-3 composite material altered the mechanical and electrical behaviors, leading to a response disparity. The Mises strain for the horizontal stacking configuration ranged between 2.34 ppm and 1330 ppm, while it changed between 3.14 ppm and 1410 ppm for the *2v*-REV. The results in Figure 2-4 reveal two insights about the microscale response that, while probe unobtainable experimentally, provide a fundamental understanding of the underlying mechanisms dictating microscale magnetoelectricity.

First, the bias magnetic field induced drastically different deformation behavior in otherwise identical spherical particles at the onset of stimulation. The deformed particle geometry,

in turn, resulted in distinct particle-to-particle interactions with a pronounced difference in the magnetoelectric response, as discussed above. On the one hand, the particles in the *2v*-REV configuration are deformed into ellipsoids, where the major axis is aligned with the bias magnetic field direction that corresponds to magnetic saturation. The resulting elongation along the magnetic field was uniform throughout the magnetostrictive particles. However, the location of the deformed particles within the PVDF-TrFE matrix exhibits a repulsive response, where the particles appear to have elongated outwardly more than towards each other. Specifically, the geometric center of the deformed ellipsoidal particle has shifted 0.435nm towards the undeformed surface. This positional shift is thought to result from the force imbalance between the magnetic attraction of the inner opposite poles and the reactive force due to the compression of the entrapped piezoelectric matrix between the particles. This distinct spatial arrangement of the particles in the *2v*-REV resulted in a nearly uniform magnetic flux between the particles of 55±10 mT. On the other hand, the *2h*-REV particles deformed inwardly into reniform shapes, signifying the non-uniform interaction between the magnetic field and the magnetic particles. The reniform shape is due to a non-uniform state of magnetization, where the inward concaved surfaces elicit a 75.6% lower magnetic flux than the convex contoured surfaces. The horizontal arrangement of the magnetic particles within a uniform vertically emanating magnetic field results in a differential crowdedness of the magnetic field lines towards the equator with lower magnetic flux passing between the particles. In other words, the non-uniform magnetization in the particles is due to the magnetic flux from the bias magnetic field splitting between the particles. This can be thought of as a pseudo-shielding effect, as in the case of a hollow sphere or cylinder geometry [35]. Hence, the inward orientation of the reniform geometry is justified. Finally, the magnetic flux between the horizontally aligned particles is 29±5 mT, which is 52% lower than the *2h*-REV configuration.

Subsequently, the resulting electrical distribution exhibits the dependency of the stacking configuration, consistent with the overall direct magnetoelectric paradigm [4]. The applied magnetic field resulted in a strain that induces a change in electrical displacement within the piezoelectric matrix. There are three distinct behavioral differences between the *2h*- and *2v*-REV stacking configurations. The average electronegativity in the overall stacked fundamental units was primarily found to be 9.7 mV and 26.7 mV for the *2v*- and *2h*-REVs, respectively. Such a disparity in the response is attributed to the full-field strain distribution within the matrix based on the aforementioned magnetostrictive response. Secondarily, the electrode surface of the *2v*-REV is nearly in the state of electropositive, while the *2h*-REV is highly electronegative. The latter is preferred given the negative piezoelectric nature of PVDF-TrFE, explicating the drastic difference in the DME coefficient between these two configurations. Finally, the state of strain in the 2*v*-REV was found to be nearly uniform in the matrix (Figure S4) between the particles based on the magnetostriction response based above. In contrast, the *2h*-REV exhibited a nonuniform state of strain (Figure S5) between the particles inducing the electroactive response shown in Figure 2-4 and, in turn, enhancing the overall DME coefficient.

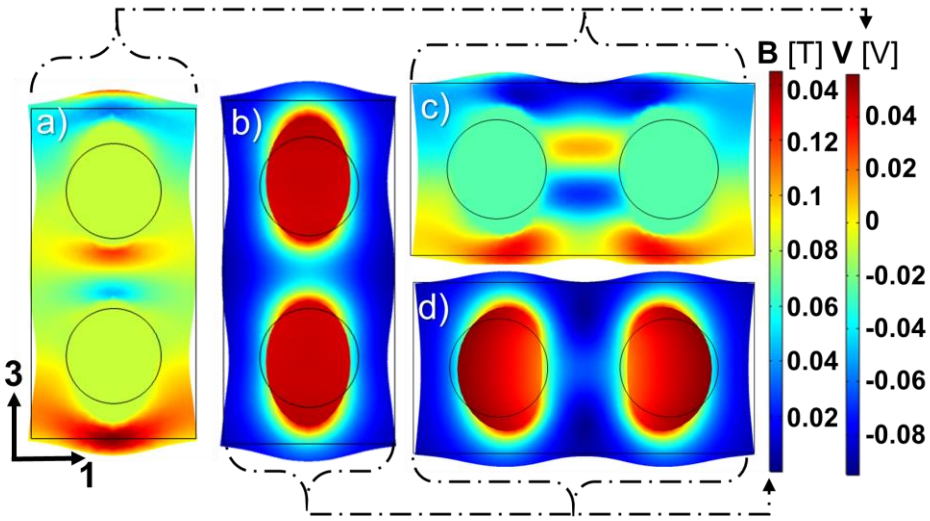

Figure 2-4: Sectional distribution of the magnetoelectric response of 2-REV composites, demonstrating the dependence of the coupling coefficient on the orientation and stacking. (a) The electric potential exhibiting a nearly uniform distribution along each particle and (b) magnetic flux entrapped within the magnetic particles of a *2v*-REV. (c) The electric potential exhibiting a spatial distribution between and along the particles and (d) magnetic flux non-uniformly deforming the magnetic particles of a *2h*-REV.

2.5.4 Particle Arrangement

The previous discussion indicates that particle-to-particle interactions significantly affect the overall magneto-mechano-electric response, while such control on the particle positioning is experimentally challenging (unless the particles exhibit some self-assembly behavior). A virtual experiment was then developed to deduce the effect of positioning on the overall response, where the distance between multiple particles is forecasted to alter the particle-to-particle interactions and the resultant DME coupling. Figure 2-5a schematically shows a composite structure consisting of four REVs with a volume fraction of 10%. The particle position was defined using two variables to describe the proximity of the particles to the top electrode (i.e., vertical spacing) and each other (i.e., separation). In total, nine different configurations were envisioned, and their response was calculated. In essence, the vertical separation parameter indicates that particle settlings may occur during manufacturing, while the particle separation is associated with agglomeration due to particle size and the jar milling process [26]. The DME as a function of the particle separation and

vertical positioning is plotted in Figure 2-5b. In all, the contour plot in Figure 2-5b signifies the reliance of the DME on the relative particle positions with different degrees of dependency of agglomeration and settling.

The results indicate the DME sensitivity to the particle separation, varying by 60.2±2.8% with 2.1<d/R<5.5, regardless of the vertical position. The latter resulted in merely a 5% deviation in the calculated response. Independent of the vertical position, the inverse relationship between the DME values and the particle separation is attributed to particle-to-particle interactions, as discussed in the previous section. When the four particles are at d/R=2.1, nearly creating a uniform magnetic flux emanating from the particles (see Figure S6), the DME was found to be 1.149 V/A. At the other extreme, i.e., d/R=5.5, where every particle has a different magnetic response (Figure S5), the DME was expectedly lower at a value of 0.502 V/A. This is consistent with the conclusion stated above for the case of an ellipsoidal particle with the same volume fraction, where the major axis was parallel to the global 1-direction. In simple, the agglomeration of the particles is shown to be beneficial to the resulting magnetoelectric response since it enhances the electronegativity of the composite. These computational results then suggest that particle agglomeration is a lower importance experimental issue, as far as it does not create a percolation path that defies the entire coupling paradigm.

The DME value remained nearly constant for any given scenario of particle separation (2.1<d/R<5.5). The DME insensitivity to the vertical particle location is attributed to the simulated volume fraction of 10%. The latter results in an allowable vertical shift of only ~15% without permitting any of the particles to short circuit with the top or bottom electrodes. The effect of volume fraction on the overall response was summarized previously in Figure 2-2. The distance between the top electrode and the pole of the particle changed from 0.886 μm to 0.586 μm,

corresponding to a change in the electric field of 19.8 and 50.8 V/mm, respectively, for the geometrical configuration of d/R = 3.47. The variance in the resulting electric field (see Figure S7) represents the 5% change in the overall response mentioned above. Similar observation (but different values) was consistent throughout the entire d/R range. Therefore, the computational data points to the potential independence of the DME coefficient from particle settling, as far as the particles are sufficiently separated from the electrodes. This conclusion, along with the one based on particle agglomeration, supports the standing state-of-the-art experimental challenge in realizing and polarizing 0-3 composite materials. That is, the major limiting factors of consistently producing 0-3 composite are the thickness of the PVDF-TrFE that allows polarization using available voltage sources and the quality of the matrix being free of voids or holes that prevent the reliable application of polarizing electric fields.

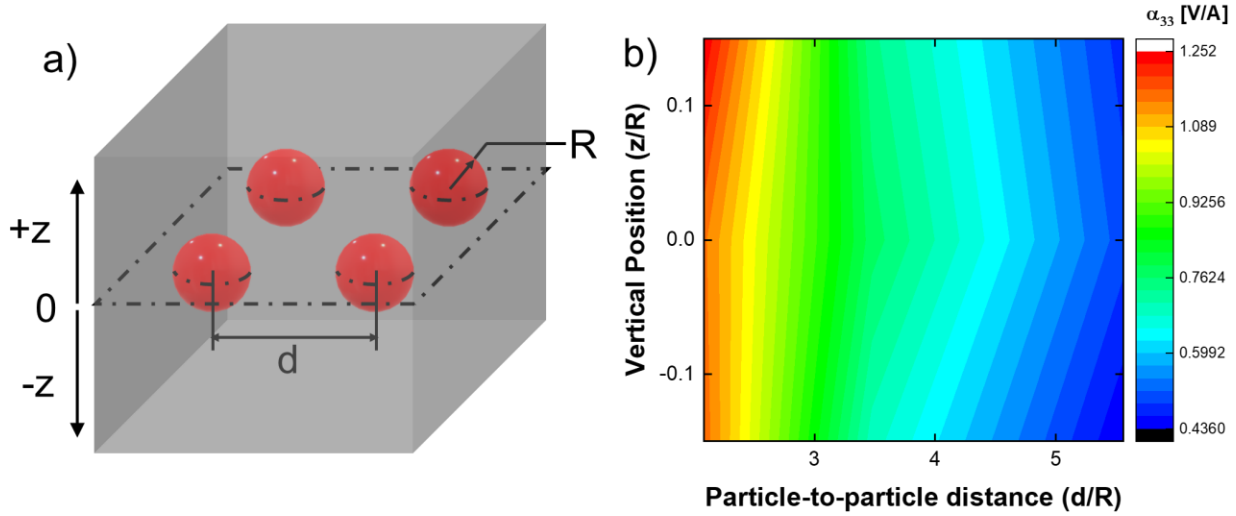

Figure 2-5: (a) Schematic representation of a composite with four identical spherical particles on the same Z-plane. (b) Contour plot of the DME as a function of the vertical position (z) and the center-to-center distance (d) of the particles normalized by the radius. The magnetoelectric results indicate the importance of spatial distribution (i.e., lack of agglomeration) and the independence from the settling of the magnetic particles, which recently substantiated by the experimental work reported in [36].

2.6 Conclusion

The pursued of compliant magnetoelectric composite materials for wearable and flexible electronics highlight the need for insights into the interactions between the constituents based on their material properties and ratios. To this end, a fully-coupled computational model was developed and verified to observe the microscale magnetoelectric behavior of Terfenol-D/PVDF-TrFE core-shell and 0-3 composites. The magnetic, elastic, and electric responses for single-particle composites depend on their geometric attributes and particle-to-particle arrangement with respect to a comprehensive set of magnetic, mechanical, and electrical boundary conditions. This research elucidated the interrelationship between the magnetoelectric coupling coefficient and several geometrical attributes, leading to insight at the microscale.

Previous experimental research revealed the particle geometry after size reduction processes severely depart from the simplified spherical geometry commonly pursued in analytical models. This research study considered several platonic geometries (e.g., cube, octahedron, and dodecahedron), comparing their impact of the magnetoelectric performance with analytical models and spherical and ellipsoidal geometries. The magnetoelectric response was enhanced when using geometries that bared resemblance to a 2-2 composite structure, such as particles shaped as a face-aligned cube (when f=0) or an oblate ellipsoid. Conversely, particles that were similar to a 1-3 composite, such as the prolate ellipsoid or the vertex-align cube (v=0), exhibited a negative correlation with the magnetoelectric coupling. Thus, non-centrosymmetric particle geometries (i.e., any geometry other than the sphere) can be used to tune the magnetoelectric coupling coefficient, depending on their orientations.

The computational framework used in this research study also allowed for investigation of different stacking configurations and particle arrangements in relation to the resulting

magnetoelectric coupling coefficient. The magneto-electro-mechanical responses were significantly altered by their neighboring particles, such that the magnetoelectric response is enhanced with particles side-by-side and hindered with top-and-bottom alignment. Moreover, the magnetoelectric response was also improved when the particles were agglomerated while vertical positioning bared negligible. The non-uniform voltage distribution of the spherical REV can be utilized in applications such as serving the media of nanoscale dielectrophoretic particle motion or can enhance the magnetoelectric coupling if intelligent probing is employed.

In all, the computational model provides a utility to supplement the existing experimental results while allowing a unique insight into the performance of 0-3 magnetoelectric composites. Future research can leverage the outcomes of this study in developing efficient particulate multiferroic composite materials for wearable and flexible electronics.

2.7 Acknowledgements

Chapter 2, in full, has been submitted for publication of the material as it may appear in Intelligent Materials and Structures 2021. Youssef, George. The dissertation author was the primary investigator and author of this paper.

Chapter 3 Exploring Terfenol-D/P(VDF)-TrFE 0-3 Composite for Energy Applications

Scott Newacheck, Anil Singh, and George Youssef

3.1 Abstract

In the current work, quantitative analysis of magnetoelectric particulate composite material system explicated the main mechanisms responsible for the below-optimal performance of this class of materials. We considered compliant particulate composite materials, with constituents relevant to technological and scientific interest, leading to 0-3 Terfenol-D/PVDF-TrFE composite samples. To this objective, thick Terfenol-D/PVDF-TrFE films (10-15 μm) were fabricated and analyzed for chemical, mechanical, and magnetic properties to demonstrate their suitability for energy applications in harsh environmental conditions. The vigorous experimental characterization of the composite exemplified the multifunctional properties, quantifying the interrelationship between the composition and performance. We observed that the addition of magnetic particles to the electroactive copolymer matrix resulted in improvement in the mechanical and electrical properties since the particles acted as pinning sites, hindering the deformation of the chains and enhancing polarization. The effective modulus model was amended to account for the crystallization-induced change in material stiffness. We also measured and computed the magnetic particles motion to explicate the detrimental effect of mobility and migration on the overall magnetoelectric coupling performance of the composite. Thereby, we derived an analytical model based on the magnetic force due to the co-presence of alternating and constant magnetic fields, and the viscous drag force due to the viscoelastic properties of the electroactive copolymer matrix. We demonstrated that the mobility of the particles plays a crucial role in the short and long term performance of magnetoelectric coupling in multiferroic particulate

composites, uncovering the underpinnings of the dichotomy in performance between experimentally measured and analytically predicted coupling coefficients., thus, allowing for the proposal of new approaches to realize the scientific potential of magnetoelectric particulate composites in energy applications.

3.2 Introduction

The availability of electrical energy is imperative for improving and sustaining the quality of life, where the mode of transferring the energy from the generator to end-use devices also plays a significant role. Therefore, the general pursuit of energy harvesting technology hinges on the need for broader and easier access to power electronic devices and the necessity for simplification of ever-complex engineered systems. The accessibility challenge provides unprecedented opportunities for innovation, extending from powering implanted biomedical devices, charging a drone en route for package delivery, or beam energy to spacecraft in deep space [1]. The ability to efficiently receive energy wirelessly can also be leveraged at the microscale to develop bus-less printed circuit boards or triggering communications at the nanoscale with self-assembled nanoparticles and deployed nanobots without umbilical cords. Furthermore, energy harvesting is beneficial in reducing the complexity of engineered systems with far-reaching advantages beyond the design stage by simplifying troubleshooting and maintenance due to the reduced system topology. A non-obvious byproduct of energy harvesting reduces the weight of the system by the elimination of wires from the source to the powering terminals of each device, hence also reducing operating cost.

Among the many mechanisms which can harvest energy, magnetoelectric composites stand out for their ability to perform on a wide range of length (nm to cm) and time (ps to ms) scales. The magnetoelectric composite system utilizes piezoelectric and magnetostrictive materials to harvest magnetic energy and convert to electric displacement with strain as a mediator. A critical limitation of the current state-of-art in strain-mediated magnetoelectric composite systems is the reliance on lead-based brittle ceramic materials, specifically the piezoelectric PZT or PMN-PT. Lead-based piezoelectric ceramics offer high electromechanical coupling, ideal for optimizing the

magnetoelectric efficiency, but are very brittle for soft-robotic applications and toxic to be used in wearable or biomedical devices [2]. This shortcoming has motivated the current research in organic-inorganic particulate multiferroic composites, where inorganic magnetostrictive particles are embedded into an organic piezoelectric polymer matrix. Organic polymers possess traits suitable for biomedical devices and soft robotics, such as flexibility, ductility, and biocompatibility, lending these desirable attributes to the composite structure [3]. The development of efficient particulate multiferroic composite materials is a twofold approach. First, the selection and optimization of an efficient electroactive polymer matrix can tune the response based on its molecular structure. Some organic piezoelectric polymers noteworthy for their high electromechanical coupling include cellulose, polyvinylidene fluoride (PVDF), and copolymers of PVDF with trifluoroethylene (TrFE), 1,1-chlorofluoroethylene (CFE), and chlorotrifluoroethylene (CTFE) [3]. Second, the choice of magnetic particles capable of retaining their magnetic and magnetostrictive responsiveness regardless of the length scale. In the previous organic-inorganic technologies, cobalt ferrite, iron oxide, and nickel nanoparticles were used as the magnetic materials; however, higher quality materials such as Terfenol-D or Galfenol may be used instead [4].

Of the available organic piezoelectric polymers, PVDF and its copolymers exhibit excellent resistance to a wide range of chemicals, UV radiation, aging, and other harsh environmental conditions, granting even more widespread usability for PVDF-based multiferroic composites. Processing PVDF for piezoelectric applications is a standing challenge, necessitating special steps to form chains with polar stereochemical conformations of trans (T) and gauche (G) linkages. For example, the β-phase (TTTT) and γ-phase (TTTGTTTG) configurations are desirable

for piezoelectric properties while the α-phase (TGTG) is unfavorable [5]. Increasing the content of the desirable polar β-phase in PVDF can be accomplished through poling, stretching, doping, or the addition of TrFE [6]. Ensuring a high content of β-phase is essential for optimizing the magnetoelectric efficiency of organic-inorganic PVDF and PVDF-TrFE matrix multiferroic composites. The content of β-phase can be quantified through spectroscopy based on specific bond vibrational modes of each phase [5]. Moreover, diffraction techniques can be used to identify the crystallinity of each phase qualitatively [6]. Remarkably, a byproduct of the addition of magnetic particles as a constituent of the particulate multiferroic composites is enhancing the formation of β-phase in PVDF and its copolymer derivatives, as will be discussed later.

As is the case in processing the electroactive polymer matrix, the preparation of magnetic particles also faces a set of challenges, including size reduction without breaking down functionality. Terfenol-D exhibits the highest reported magnetostriction properties of all previously used materials at room temperature. Terfenol-D is an alloy of iron, terbium and dysprosium, with a specific volume fraction of each of the constituents to achieve such high magnetostriction, further complicating the size reduction process [7]. For example, reducing the size of Terfenol-D particles from a few hundred microns to less than two microns poses a significant obstacle because of the susceptibility of oxidation and agglomeration. To overcome the former, the particles are usually suspended in heptane and oleic acid to inhibit the latter [8]. Previously, the authors successfully demonstrated reducing the Terfenol-D particle size before synthesizing a multiferroic composite structure using the PVDF-TrFE matrix [9]. It is imperative to note the achieving a small magnetic particle size enables the polarization of the PVDF-TrFE matrix to access higher β-phase content. Therefore and in overcoming all these challenges,

Newacheck *et al.* demonstrated that the inclusion of low weight percentages of Terfenol-D enhanced the polarization of the PVDF-TrFE and the dielectric properties of the composite structure, while showing a negligible effect on the piezoelectric properties [9]. In addition to Terfenol-D, other researchers pursued other magnetic particles (e.g., LCMO, NZFO, Fe_3O_4, and CFO) with different weight fractions to attain measurable magnetoelectric composites with long-term performance [10]–[13]. Thus far, the experimental performance of these composites did not match the forecasted magnetoelectric coupling coefficient based on theoretical and computational models. This dichotomy is quantitatively pursued and explicated in this paper, primary research novelty.

It is then the overarching objective of the research leading to this paper to vigorously and quantitatively investigate the fundamental mechanisms responsible for the magnetoelectric performance of PVDF-TrFE/Terfenol-D composites. In anticipation of harsh environmental, loading, and operating conditions during deployment of devices, an emphasis was given to elucidate the mechanical, hygrothermal, magnetic, and magnetoelectric properties, as well as the microstructural characteristics of the composite material.

3.3 Materials and Methods

3.3.1 Sample Preparation

The addition of magnetic particles to the piezoelectric PVDF-TrFE polymer matrix has been shown before to enhance the electroactive response but with several fabrication and functionalization challenges. From the fabrication point of view, the dispersion of the relatively heavier Terfenol-D particles is prone to agglomeration or settling during the solidification of the PVDF-TrFE solution. Subsequently, and during poling, the conductive magnetic particles may

create a percolated pathway, resulting in electrical breakdown and deeming the composite unfunctional. Therefore, the sample preparation step of this research investigation sought to study the effect of increasing the weight ratio of the magnetic particles on the overall performance. The first step was to reduce the particle size since the as acquired Terfenol-D particles (Td-Vib), with a diameter ranging from 200 to 300 µm, are susceptible to electrical breakdown failure due to being larger than the permissible thickness of the piezoelectric matrix. The Terfenol-D particles were then jar milled for 15 hours in heptane as a milling medium (Fischer Scientific, CAS: 142-82-5) and oleic acid as a dispersion agent (Fischer Scientific, CAS: 112-80-1). The jar milled Terfenol-D particles were subsequently filtered through a 2-micron pore size paper sieve (VWR 28430-109). The remaining < 2 µm particles at different weight ratios were mixed with dimethylformamide (Fischer Scientific, CAS: 68-12-2), using an ultrasound mixer for 2 hours to disperse the particles evenly. PVDF-TrFE beads (Solvay Solvene 250) were then added to the solution while continuing ultrasound mixing for an additional 2 hours. The solution was spin-coated at 400 RPM for 5 minutes, followed by a curing process at 120°C for 2 hours. This process was repeated to make samples of 0.5 *wt.*%, 2 *wt.*%, and 10 *wt.*% of Terfenol-D and in the absence of any magnetic particles to create neat polymer sheets. The average final thickness of the stock sheets ranged between 10 and 15 microns. Specimens with different geometries were extracted from these sheets depending on the characterization techniques, as discussed in the following sections.

3.3.2 Micrographic Analysis

The morphology, topography, and magnetic phase scans of the samples were acquired using scanning electron (SEM) and magnetic force (MFM) microscopes. To minimize charge accumulation and interaction between the accelerated electron beam and the active polymer

matrix, a thin platinum layer of ~6nm was deposited in an argon environment using a Quorum Tech Q150T sputtering machine. Electron micrographs captured using an FEI Quanta 600 at an accelerating voltage of 20 kV when imaging the particles and 8 kV for the composites. The SEM micrographs were analyzed to elucidate the distribution of the magnetic particles within the electroactive polymer matrix and the morphology of the samples.

One of the persistent issues associated with the fabrication of 0-3 composites using Terfenol-D as the magnetic phase is loss of magnetization due to oxidation. Here, heptane was used to prevent oxidation during the jar milling and particle aggregation with the PVDF-TrFE matrix solution, based on the work of [8]. MFM magnetic phase scans were obtained by an AFM Workshop TT1 using Bruker MFMV magnetic tips to confirm retention of the magnetic properties of Terfenol-D particles within the electroactive polymer matrix.

3.3.3 Chemical Structure Analysis

Fourier-transform infrared spectroscopy with attenuated total reflectance (FTIR-ATR) was carried out using a Thermo Scientific Nicolet iS5 with air as the background. For this spectroscopic characterization, neat and filled PVDF-TrFE samples were investigated. Three neat PVDF-TrFE samples were each scanned three times, and the spectra were averaged. Poled and unpoled (referred to as 'virgin' thereafter) samples were also scanned to elucidate the effect of polarization on β-phase transformation, favorable for electromechanical performance. However, a high percentage of electrical breakdown was observed; hence, the polling setup was modified by including an ultrathin polyethylene separator between the sample and the electrodes to avoid premature electrical breakdown. Similarly, Terfenol-D filled PVDF-TrFE samples with varying volume fractions were investigated using the FTIR-ATR method, namely with 0.5 *wt.*%, 2 *wt.*%, and 10

wt.% weight ratio of Terfenol-D. In addition to delineating the effect of Terfenol-D on the β-phase transformation, data from polled samples without the separator was collected and compared with data from separator-polled samples. The FTIR spectra were then used to calculate the content of the β-phase of each sample.

The crystallographic interatomic spacing characterization was performed using Philips XPert XRD with a copper light source providing a wavelength of λ = 1.5405 Å. The samples were cleaned and placed on an amorphous glass substrate for measurement. The scanning angle (2θ) was varied from 2° to 70° at a rate of 2° min^{-1}. The wide range was chosen to ideally observe diffraction peaks of Terfenol-D, which were previously reported at 2θ of 34.5°, 40.7°, 42.6°, and 49.6°. However, these peaks were absent from the XRD spectra collected from the composite sample due to the low volume fraction and the complete surface coverage with PVDF-TrFE. The latter is attributed to the difference in the density of the magnetic particle with respect to the polymer matrix, giving rise to the settling or buoyancy of the particles. The interatomic distance (d) was calculated using Bragg's law, $2d \sin\theta = n\lambda$, where n is a positive integer. Therefore, the XRD results provided evidence of the phase transformation of PVDF-TrFE crystal structure. The XRD results were also used to calculate the average size of the crystallites (L) from the width of the peak (H) using Scherrer's equation, $H = \frac{\lambda}{L\cos\theta}$.

3.3.4 Thermomechanical Analysis

The high weight fraction of the polymer matrix leads to sensitivity of the mechanical behavior of the composite samples to temperature [14]. The glass transition of PVDF-TrFE is -37 °C, while the melting temperature is 146 °C, providing a wide range of operating temperatures for numerous electronics applications. Thus, the dynamic thermomechanical properties of the

Terfenol-D/PVDF-TrFE 0-3 composite were characterized using a dynamic mechanical analyzer (TA Instruments, Q800) in tension at temperatures ranging from -80 °C to 125 °C at a rate of 2 °C/min, where the gas controlled accessory to the DMA (TA Instruments, GCA) maintained the cryogenic temperature. The dimensions of the samples were ~5 mm long, ~5 mm wide, and ~0.11 mm thick. The samples were preloaded with 0.1 N and loaded at 1 Hz, 0.1% strain. At the onset of testing, each sample was cooled down to -80 °C and held at temperature for a 15 min soak time to reach initial isothermal conditions. The storage modulus and tanδ are reported as a function of temperature and magnetic particle weight fraction.

3.3.5 Thermogravimetric Analysis

The excellent hygrothermal properties of PVDF-TrFE position it as a material candidate for applications surrounded by the harsh environment (e.g., chemicals, high friction, and high strain rate) while maintaining inertness. The thermal and hygrothermal stability of the Terfenol-D/PVDF-TrFE 0-3 composite were investigated using a thermogravimetric analyzer (TGA, TA Instruments, Q50) of as-processed samples, as well as samples that were submerged in deionized water (diH_2O) or saline solution for 24 h. Other sample sets were exposed to ultraviolet radiation while being submerged in diH2O or saline with an exposure level of 1.1 J/cm^2. Generally, the TGA samples with a ~15.8 mm diameter were extracted using a circular hammer punch from the previously fabricated sin-coated sheets. In the TGA, the samples were heated at a rate of 2 C/min while ultra-high purity nitrogen gas at a 60 mL/min flow rate purged the TGA furnace throughout the measurements. A final set of samples were tested under the same conditions in the presence of a magnetic field. In this case, an electromagnet coil was wrapped around the external surface of the TGA furnace to apply a 500 Oe magnetic field in the axial direction to observe the effects of a magnetic field on the thermal decomposition of the composite.

3.3.6 Magnetization Analysis

A Quantum Design MPMS magnetometer was used in the DC mode to measure the magnetic properties of the 0-3 Terfenol-D/PVDF-TrFE composite samples. The samples were cut into 6 mm x 5 mm strips, and the magnetization was measured along the length direction. The bias magnetic field was first ramped up to 2000 Oe then ramped down to -2000 Oe, at which point it was ramped back up to 0 Oe in steps of 100 Oe at a rate of 700 Oe/s. All magnetic measurements were made at room temperature.

3.3.7 Magnetoelectric Analysis

Electrode-fitted 0-3 Terfenol-D/PVDF-TrFE composite samples were situated at the center of an electromagnet (GMW, 3470) that was powered by a programmable DC power supply (Sorenson, DLM 60-10). The applied magnetic field was monitored using a Hall probe (F.W. Bell, HTR81-0608-10) connected to Gaussmeter (F.W. Bell, 8030). An AC magnetic flux was applied with a Helmholtz coil powered by a TS250 Accel instruments waveform amplifier, while the AC flux was monitored using a search coil. An Agilent 33210A waveform generator was used to modulate the frequency of the AC magnetic field. The direct magnetoelectric voltage, i.e., across the sample electrodes, was then measured with an SRS 830 lock-in amplifier. The magnetoelectric characterization consisted of two cases, namely field-sweep and frequency-sweep. In the field-sweep case, the DC magnetic field was swept from 0 to 2700 Oe with a superimposed 16 Oe 4 kHz AC magnetic flux. Alternatively, in the frequency-sweep case, the frequency of the AC magnetic flux was swept from 1 kHz to 100 kHz while the DC magnetic field was held constant at 650 Oe. The DME was measured when the magnetic field was aligned along with the thickness or the length directions, separately, i.e., α_{33} and α_{31}.

3.4 Results and Discussion

The following subsections mirror the structure of the experimental investigations reported above. While each subsection is comprehensive within itself, it remains symbiotic with other subsections. The culmination of these subsections constitutes a comprehensive property map of the 0-3 Terfenol-D/PVDF-TrFE composites. At the outset, we present and discuss the elusive mechanism responsible for the persistent underperformance of magnetoelectric particulate composites while hypothesizing a future research direction to overcome this debilitating shortcoming.

3.4.1 Micrographic Analysis Results

Figure 3-1 is a collage of SEM micrographs, showing as-received Terfenol-D particles ranging from 300-600 μm (Figure 3-1a), the particles after 15 hours of jar milling effectively reducing the size (Figure 3-1b), the top surface morphology of a composite sample (Figure 3-1c), and the effect of prolonged exposure of the electron beam during imaging on the composite film (Figure 3-1d). When comparing the particles from Figure 3-1a to Figure 3-1b, the reduction in size and the formation of planar surfaces with sharp corners are due to the particles cleaving associated with the brittleness of Terfenol-D and the localized impact during the jar milling process. Figure 3-1b illustrates that jar milled Terfenol-D particles are better represented by platonic geometries rather than the ubiquitously assumed spherical shape in analytical and computational modeling efforts [15], [16]. The platonic geometries with planar surfaces were recently computationally shown to exhibit superior magnetoelectric response compared to spherical geometries in 0-3 composite materials [16]. The platonic geometry of the jar milled Terfenol-D particles is imprinted on the surface morphology micrograph shown in Figure 3-1c, where the size of the particle is ~2.3

μm, representing the expected size after jar milling and filtering. Reconnaissance of the sample surface using SEM confirmed the dispersion of the magnetic particles within the sample, where signs of agglomeration or fully exposed particles were absent from all collected SEM micrographs. The surface morphology was dominated by a fibrous texture regardless of the filler condition (see Figure 3-1c and its inset) with fibril length spanning 5 μm to 25 μm. This fibrous texture of the PVDF-TrFE matrix is attributed to the formation of semi-crystalline domains during the high-temperature curing process [17]. A higher degree of crystallinity is associated with enhanced electroactive response and stiffer mechanical properties [5]. Finally, the electroactive nature of the PVDF-TrFE matrix in the 0-3 composite samples challenged the examination under the SEM, where the accelerating voltage of the electron beam (on the order of 20kV) resulted in the inverse piezoelectric coupling (Figure 3-1d). The spot under the electron beam was marked with a sign of shrinkage strain (surface wrinkles) and localized cracking within a few minutes of beam exposure.

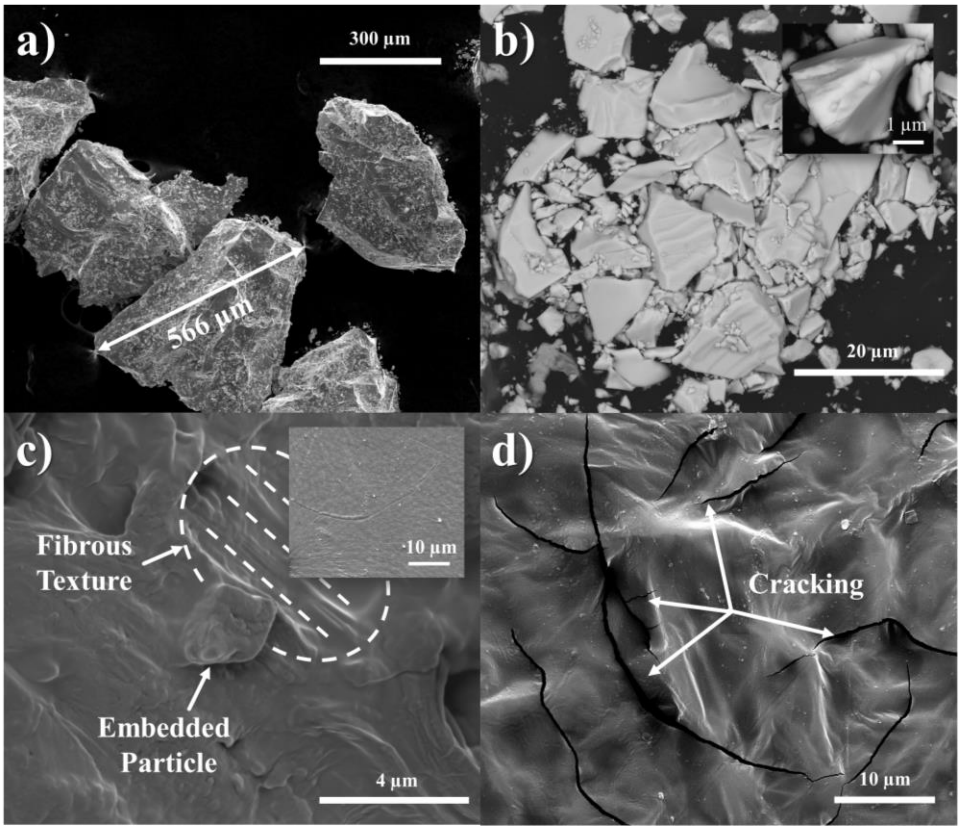

Figure 3-1: SEM micrographs of (a) as-received Terfenol-D particles, (b) the Terfenol-D particles after 15 hours of jar milling (inset showing an individual particle), (c) the top surface of a 0-3 Terfenol-D/PVDF-TrFE composite sample (inset showing a larger surface area), and (d) the top surface after a few minutes of electron beam exposure.

The retention of the magnetic behavior of the Terfenol-D particles is imperative for magnetoelectric coupling application and was demonstrated with MFM scans. Figures 3-2a and 3-2b show the topography and magnetic phase of a 0-3 Terfenol-D/PVDF-TrFE composite sample, respectively. The fibrous surface morphology previously observed on the SEM micrographs was also present in the AFM topography in Figure 3-2a. Four magnetic particles were detected in the magnetic phase scan in Figure 3-2b. The lack of representative features of the magnetic particles in the topography scan (Figure 3-2a) indicates that these particles were situated beneath the surface. Each of the four magnetic particles are less than 2 microns in breadth (characteristic of

the particles, as discussed in the sample preparation section), proving that Terfenol-D particles still exhibit magnetism after the harsh jar milling, filtration, and sample fabrication processes. Additionally, the four particles appear to be adequately separated, which is in good agreement with the SEM results discussed previously. Generally, MFM scans semi-quantitatively demonstrate the persistence of the particle magnetism, but the VSM results represented below quantify the magnetic behavior.

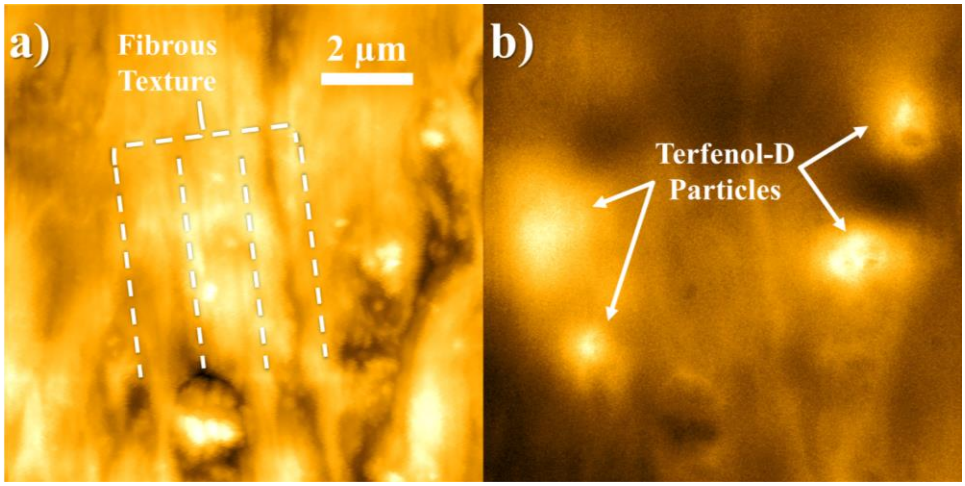

Figure 3-2: (a) Atomic Force Microscope topography scan of the 2 *wt.*% Terfenol-D/PVDF-TrFE composite sample and (b) corresponding magnetic phase scan, showing the Terfenol-D particles retaining magnetization.

3.4.2 Chemical Structure Analysis Results

The FTIR spectra for the Terfenol-D/PVDF-TrFE composites are plotted in Figure 3-3a. The trans- and gauche- conformations of the PVDF molecular structure contribute different vibrational peaks, which are also observed in PVDF-TrFE. Moreover, PVDF-TrFE exhibits several stereoregular orientations (e.g., α -, β -, and γ- phases), giving preference to enhanced piezoelectric and dielectric performances [6]. These structural phases have distinct spectra patterns of trans and gauche conformations in the FTIR spectra. Bands at 840 and 510 cm^{-1} are linked with

the desirable β-phase PVDF, whereas 530 and 614 cm^{-1} are associated with the α-phase [18]. The phase content can be calculated by emphasizing the major peaks commonly attributed to the α-phase at 530 cm^{-1} and the β-phase at 840cm^{-1}. Hence, the FTIR spectra in Figure 3-3a indicate virgin PVDF-TrFE has a 19.8% larger α-phase 530 cm^{-1} absorption, while the poled PVDF-TrFE has a 3.2% greater β-phase peak at 840 cm^{-1}. That is to say, the structure of the virgin PVDF-TrFE is biased towards higher α-phase content, which was transformed during the poling process, resulting in a higher polar β-phase in the poled PVDF-TrFE. The poling process induced the PVDF-TrFE chains to align their dipole moments (i.e., β-phase). The relative fraction of β-phase can be calculated based on the normalized absorption levels (A) at the 840 and 530 cm^{-1} bands by [19]

$$F(\beta) = \frac{A_\beta}{1.26A_\alpha + A_\beta}. \tag{3-1}$$

The numerical constant in the denominator (1.26) is based on the ratio of the absorption coefficients of the β- and α-phase which are 7.7 × 10^4 cm^2/mole and 6.1 × 10^4 cm^2/mole, respectively. The content of the β-phase was calculated to be 0.654 for the neat virgin PVDF-TrFE, and 0.707 for the poled version. The improvement from poling is in excellent agreement with [18].

The content of β-phase was found to be 0.6846, 0.6959, and 0.6817 for the 0.5 *wt.*%, 2 *wt.*%, and 10 *wt.*% of Terfenol-D/PVDF-TrFE composites, respectively. The results of the FTIR analysis are also summarized in Figure 3b as a function of the filler content fraction. The results in Figure 3b indicated that the addition of small weight fractions of the Terfenol-D magnetic filler enhanced the molecular structural orientation of PVDF-TrFE towards the preferred β-phase is

marked with enhanced ferroelectric properties, as discussed above and previously reported in [9]. The β-phase transformation in the presence of conductive particles is a commonly observed trait in 0-3 composites, such as the case of ZnO [20]. Recently, our group reported that the piezoelectric coefficient of Terfenol-D/PVDF-TrFE composite remained constant despite 0.5 *wt.*% and 2 *wt.*% of Terfenol-D [9]. The same composition resulted in a remarkable increase in the relative dielectric constant, changing from 7.6 for the neat PVDF-TrFE (poled) to 9.2 for the 2 *wt.*% Terfenol-D/PVDF-TrFE composite sample. The enhancement in the piezoelectric and dielectric properties of the composite was previously hypothesized to be associated with increasing the β-phase content, which is shown conclusively to be true based on the FTIR results presented herein. In all, the magnetic filler particles act as nucleation sites, around which the β-phase favorably formed. The application of the poling electric field then enhanced the latter.

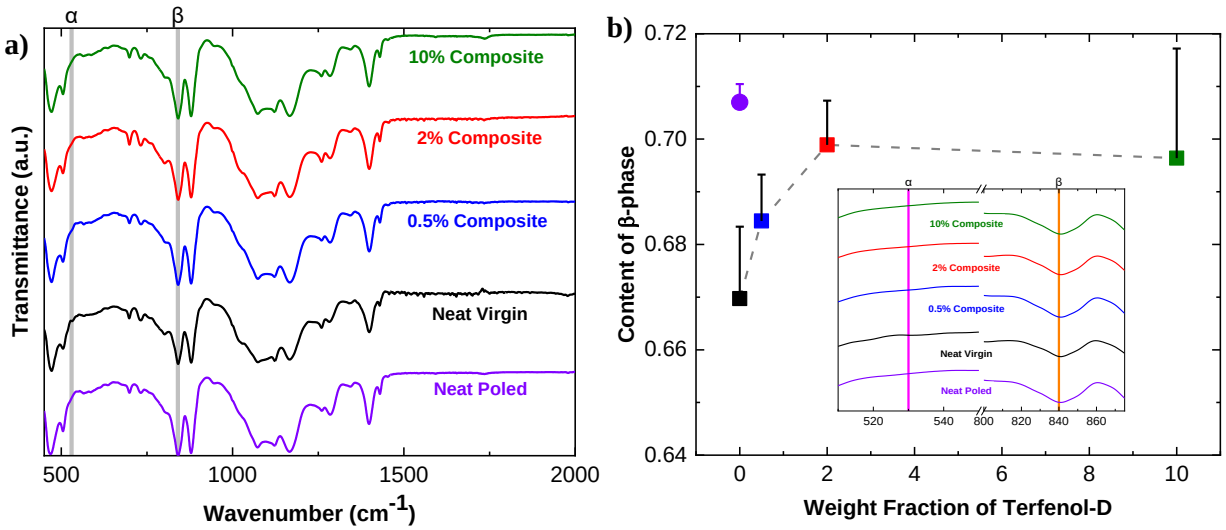

Figure 3-3: (a) FTIR spectra of neat PVDF-TrFE (poled and virgin) and composite samples of Terfenol-D/PVDF-TrFE, and (b) the content of the β-phase as a function of the weight fraction of the magnetic particles based on Equation 3-3.

Figure 3-4a plots the XRD diffraction patterns for neat PVDF-TrFE and the 0-3 Terfenol-D/PVDF-TrFE composites. Also included are the XRD patterns of the alternative newly-introduced poling strategy, which was also used subsequently to polarize the composite samples electrically. The XRD peaks were fitted into a Gaussian function to calculate the Full-Width Half-Maximum (FWHM) and the central 2θ angle, which were then used to calculate the crystallite size broadening. Additionally, the angle corresponding to the global maxima of the peak was used to calculate the interatomic spacing, as discussed before. Figure 4b summarizes the results of the crystallite size broadening and the interatomic spacing. Three observations are worthy of discussion based on Figure 4b in conjunction with the FTIR results discussed above. First, the poling method has a pronounced effect on the crystallite size, where the traditional poling (i.e., without a polyethylene separator) resulted in a decrease in size to 112.41 Å from 115.63 Å, corresponding to the neat virgin sample. Similarly, the modified poling with polyethylene separator decreased, but at a much higher rate, the crystallite size to 81.65 Å. Second, the addition of the magnetic filler particles resulted in a rebound in the crystallite size to 103.6 Å, 107.9 Å, and 120.0 Å, for the 0.5 *wt.*%, 2 *wt.*%, and 10 *wt.*% Terfenol-D, respectively, further substantiating the hypothesis of the magnetic particles acting as pinning sites during the curing process and localized electrodes during the poling cycle [9]. Finally, the interatomic spacing followed the same trend as the crystallite size, where the modified poling process decreased the spacing from 4.46 Å to 4.40 Å. The Terfenol-D particles have the same effect on the interatomic spacing as it did with the crystallite size. [21]. Khajavi *et al*. previously reported (110) semi-crystalline axis of the β-phase is associated with a larger 2θ of ~20° and smaller interatomic distance, which is in excellent agreement with the results presented above. In all, these observations point towards the coexistence of the conditions favorable for the formation of the desirable β-phase, resulting in a more efficient

electromechanical coupling. The molecular structure results from the analysis of the XRD patterns are congruent with the outcomes of the FTIR analysis.

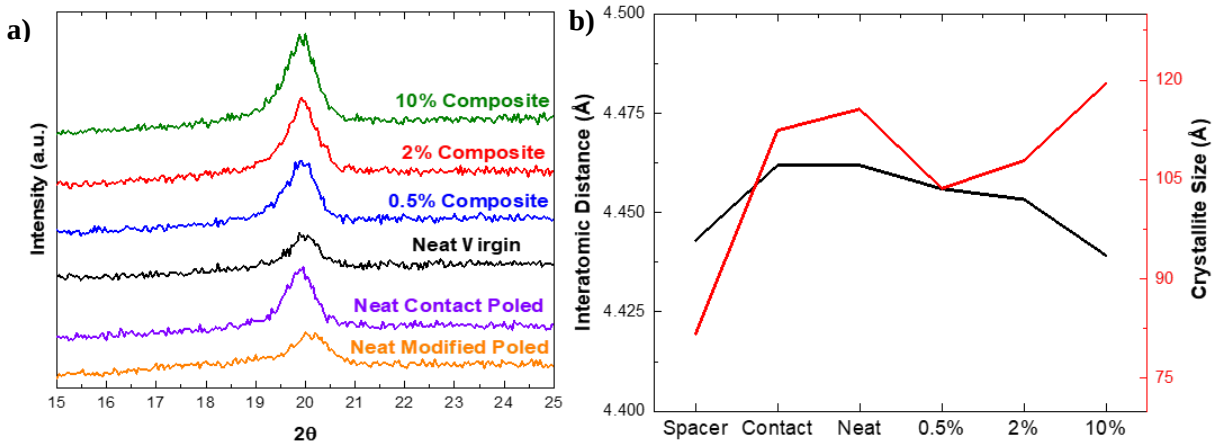

Figure 3-4**:** (a) XRD spectra of the neat PVDF-TrFE after different poling conditions and composite samples of Terfenol-D/PVDF-TrFE, and (b) the calculated interatomic distance and crystallite sizes from the XRD spectra bas on Equation 3-1 and 3-2.

3.4.3 Thermogravimetric Analysis Results

The thermal behavior of the 0-3 Terfenol-D/PVDF-TrFE composites was investigated while or after the exposure to three environmental conditions, namely magnetic field, humidity, and ultraviolet radiation. Figure 3-5a shows the thermal stability of the 0-3 Terfenol-D/PVDF-TrFE composites in the presence and absence of a constant magnetic field of 500 Oe based on the thermogravimetric analysis of the samples from room temperature up to 700 °C in an N_2 environment. The data in Figure 3-5a is bounded between 300 °C and 500 °C since no noticeable change in the thermal response was observed below or above these temperatures, i.e., major decomposition temperature is around 400 °C. Notably, the samples exhibited excellent hygrothermal stability until 350 °C, showing no drops in the weight fraction at 73 °C, 98 °C, 100 °C, or 240 °C and implying the insensitively of the materials to DMF (PVDF-TrFE organic

solvent), heptane (milling media for the Terfenol-D particles during jar milling), water (from the surrounding environment), and oleic acid (particle dispersion agent) respectively. Moreover, the samples were contamination-free of silicone oil, used during polarization to prevent electric breakdown, since the thermal spectra did not include a weight drop at 273 °C. Above 350 °C, the samples began the pyrolysis process, starting to lose weight from 400 °C to 475 °C rapidly. The primary decomposition temperature for each sample configuration was found based on the weight derivative with respect to temperature, as summarized in the inset of Figure 5a. Generally, it is concluded that the thermal response is sensitive to the weight fraction of the conductive particles while being insensitive to the presence of the magnetic field since the decomposition temperature shifted as a function of the former but not with the latter. Initially, increasing the Terfenol-D weight fraction from 0 *wt.*% to 0.5 *wt.*% then 2 *wt.*% resulted in a decrease in the onset of decomposition from 417.1±0.5 °C to 407±0.2 °C and 391.2±3.0 °C, respectively. However, adjusting the loading of Terfenol-D to 10 *wt.*% resulted in a similar decomposition temperature as the neat, specifically 413.0±2.7 °C. Here, there are two competing mechanisms. On the one hand, the addition of conductive particles with ~5400% higher thermal conductivity than the surrounding PVDF-TrFE matrix (~10.8 and ~0.2 W m^{-1} K^{-1}, respectively) acted as embedded heat sources that accelerated the decomposition process. On the other hand, the gradual phase change on PVDF due to the increase in temperature provides an additional degree of freedom to Terfenol-D by allowing it to settle to the bottom of the pan due to the decrease in PVDF viscosity, i.e., not contributing to the thermal process. The former mechanism is dominating for the case of 0.5 *wt.*% and 2 *wt.*% Terfenol-D while the latter is evident in the 10 *wt.*%. The insensitivity to the magnetic field is attributed to the correspondence of the Curie temperature to the onset of thermal decomposition,

giving dominance to thermal energy over magnetic. Later, we will discuss additional evidence on the potential migration of the magnetic particles in the presence of a magnetic field.

Figure 3-5b reports the effect of salinity and ultraviolet radiation on the thermal response of the 0-3 Terfenol-D/PVDF-TrFE composites when the pyrolysis process was done in an N_2 environment at temperatures ranging from room temperature up to 500 °C. In one set of measurements, the samples were first submerged in deionized water or saline solution (9 mg/mL) for 24 h before leaving to dry for 2 h in ambient conditions (23 °C and 30% relative humidity). The samples were then loaded and pyrolyzed in the TGA. In a separate set of measurements, the samples were concurrently exposed to ultraviolet radiation at 0.337 mW cm^{-2} while being submerged in deionized water or saline solution. The results in Figure 3-5b conclusively indicate the insensitivity of the Terfenol-D/PVDF-TrFE particulate composites to separate of combined effects of salinity and ultraviolet, hence, the suitability of this type if materials for operating under the direct magnetoelectric paradigm in harsh environmental conditions since the polarizability of the surrounding media is indifferent to an applied magnetic field. This should not be generalized for the converse magnetoelectric coupling case since the polarizability of the surrounding media plays a major role in being affected by the electric field.

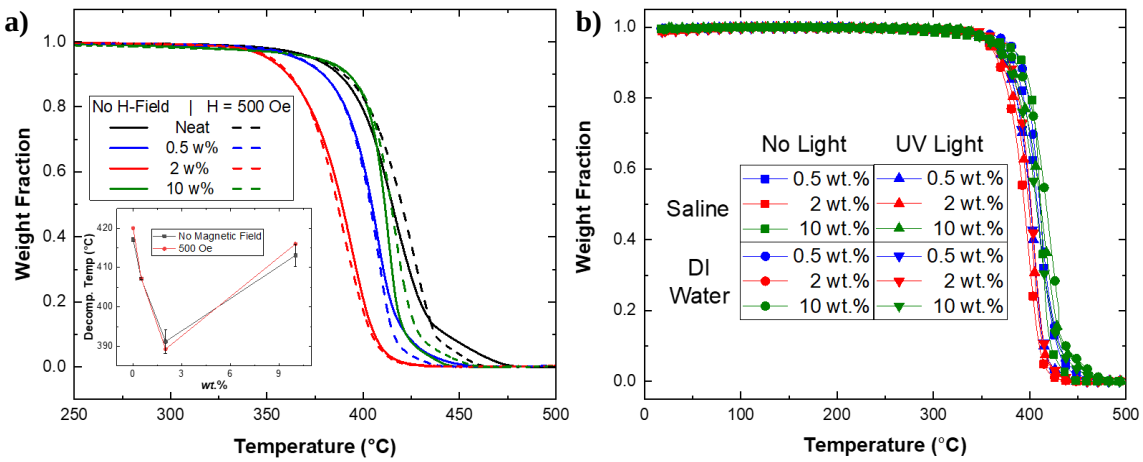

Figure 3-5: (a) TGA results of the neat PVDF-TrFE and Terfenol-D/PVDF-TrFE composites with and without a magnetic field, and (b) TGA results of Terfenol-D/PVDF-TrFE composites after 24-hr exposure to diH_2O or Saline, and UV light.

3.4.4 Thermomechanical Analysis Results

Figure 3-6 shows the thermomechanical spectra of the neat PVDF-TrFE and a representative composite sample with 2 *wt.*% Terfenol-D magnetic particles as a function of temperature ranging from -80 °C to 125 °C. The lower bound of the temperature was selected to be below the glass transition temperature (T_g) of PVDF-TrFE, while the upper bound limit was chosen to be in the melting region. The T_g of the neat PVDF-TrFE was found to be -24.53 °C based on the peak of the Tanδ curve, which is in agreement with the work of [22]. The glass transition temperature was found to be insensitive to the addition of magnetic particles, where T_g of the 2 *wt.*% magnetic particles was found to be -27.07 °C. A secondary transition within the rubbery region is observed at 28.42 °C, believed to be inspired by the crystalline structure of PVDF-TrFE and its composites. In other words, the T_c is associated with internal mobility within each crystalline region. Menard stipulated that transition within the rubbery plateau indicates crystal to crystal slip in semicrystalline polymer, which is consistent with the results discussed above, and the opinion of Clark and Scott [23]. It is worth noting that above T_c the storage modulus appears

to be insensitive to the addition of the magnetic fillers since the latter freely moving within the soften matrix, i.e., the mobility restrictions due to the crystalline phase is nullified. Above 100 °C the terminal thermal region commences where the polymer starts to liquefy.

Based on the difference in the mechanical properties of the polymer matrix and the magnetic filler particles, the addition of the latter in any percentage is expected to improve the mechanical stiffness of the composite material. Figure 3-6 shows that the addition of 2 *wt.*% Terfenol-D increased the storage modulus by 28% within the glassy region. A comparable increase in the stiffness was reported throughout the tested temperature range. Notably, a simple rule of mixture fails to account for the change in the storage modulus, as reported in Figure 3-6. Moreover, the predicted increase in the material stiffness cannot be accounted for using simple micromechanics models, including the Voigt and the Reuss limits [24]. However, the mechanical response of a material system consisting of spherical inclusions in a polymer matrix can be sufficiently and accurately predicted by the effective moduli model [24]. Attempts to adapt the effective moduli model underpredicted the effect of the magnetic inclusions on the overall mechanical response, as shown in Figure 3-6. The failure of the effective moduli model to accurately represent the response is attributed to two shortcomings that the model does not account for. First, the model is based on spherical geometry; however, as shown in the SEM images above, the jar milled Terfenol-D particles are better presented by platonic geometries. Analytical modeling of the various platonic geometries that may be assumed by the particles after jar milling was deemed impractical therefore amending the model for the geometry was abandoned. Second, the addition of Terfenol-D resulted in a substantial increase in the crystallite size, as elucidated by the XRD spectra. Such an increase in the degree of crystallinity points towards an increase in the

modulus. Since the analysis of the XRD spectra indicated a 30% increase in the crystallite size after 2 *wt.*% Terfenol-D addition, it was assumed that such increase could be predicted in the modulus. Remarkably, adjusting the modulus of the matrix phase by changing the crystallite size yielded excellent agreement of the prediction with the experimental data. The details of the model are presented next.

The modulus of the composite was calculated using the effective modulus theory for spherical particle inclusions in a homogeneous elastic media discreetly at each temperature step based on the bulk modulus and shear modulus of each constituent. The bulk (k) and shear moduli (μ) for each constituent were calculated assuming a linear elastic behavior using

$$k_{m,i} = \frac{E_{m,i}}{2(1+\upsilon_{m,i})}, \qquad \mu_{m,i} = \frac{E_{m,i}}{3(1-2\upsilon_{m,i})} \tag{3-2}$$

where, subscripts m and i correspond to the matrix (PVDF-TrFE) and the inclusion (Terfenol-D), respectively. While υ and E are the Poisson ratio and the elastic modulus. For Terfenol-D, the modulus was taken to be 23 GPa and the Poisson ratio was 0.25. The storage modulus from Figure 3-6 was taken to be the modulus of the PVDF-TrFE matrix with a Poisson ratio of 0.4. Under the assumption of a dilute particle inclusion, Christensen formulated the bulk and shear moduli for the 0-3 composite (subscript c) as

$$\frac{\mu_c}{\mu_m} = 1 - \frac{15\phi(1-\upsilon_m)[1-(\mu_i/\mu_m)]}{7-5\upsilon_m+2(4-5\upsilon_m)\frac{\mu_i}{\mu_m}} \tag{3-3}$$

$$\frac{k_c - k_m}{k_i - k_m} = \frac{\phi}{1 + \left[(1-\phi)(k_i - k_m)/\left(k_m + \frac{4}{3}\mu_m\right)\right]} \tag{3-4}$$

where ϕ is the volume fraction of the Terfenol-D inclusion [24]. Finally, the Young's modulus of the composite is then calculated using

$$E_C = \frac{9k_c\mu_c}{3k_c + \mu_c}. \tag{3-5}$$

Initial attempts to calculate the composite modulus found a large deviation between the predicted and experimental values, as shown in Figure 3-6b. As discussed above, the source of the deviation was attributed to the increase in crystallinity of the polymer matrix upon the addition of the magnetic particles, resulting in a stiffness enhancement that is currently absent from the effective modulus model. Hence, a modulus modifier (ζ) was added to the model to account for the effect of the larger crystallinity of the polymer matrix due to the particle inclusions. The modified elastic modulus of the PVDF-TrFE matrix (E_m^*) is then described as $E_m^* = \zeta E_m$. The value of the modifier ζ was calculated based on the increase in crystallinity extracted from the XRD data in Figure 3-4. Therefore, ζ was taken to be 1.27, resulting in an excellent agreement between the predicted and experimental results, as shown in Figure 3-6b.

The failure of the model in Eqn. 3-4 to predict the response points to violation of the under assumptions leading to this model. For example, the porosity within the composite may play a role. However, close examination under the scanning electron microscope, both on the surface and through the cross section, indicate the composite is pore-free, generally. Therefore, the possible accumulation and dichotomy between the elastic properties of the constituents may indicate that

the dense and stiff magnetic particle acted as pores within the electroactive polymer matrix. Future research will emphasize the basis of this hypothesis by seeking to measure the porosity.

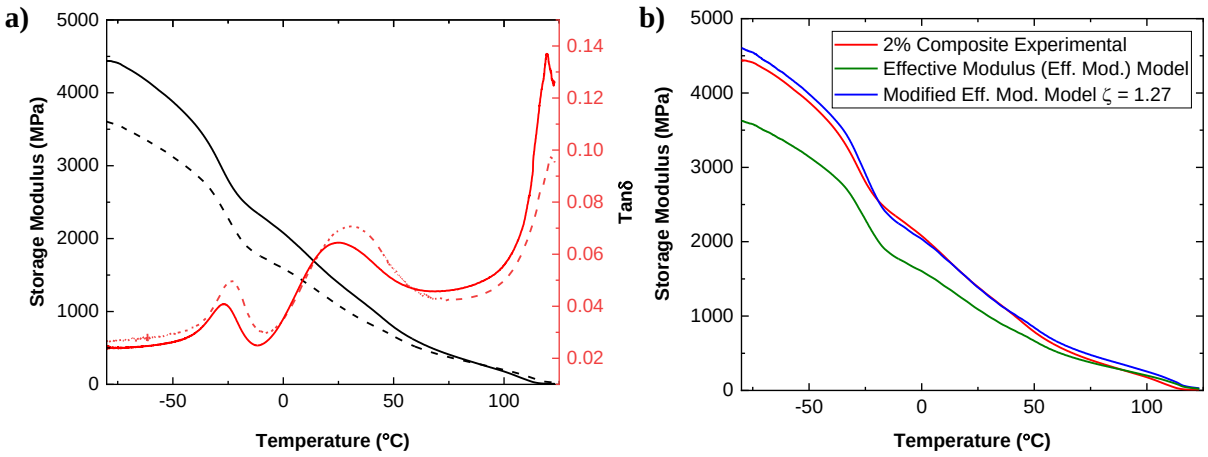

Figure 3-6: (a) Thermomechanical spectrum of neat PVDF-TrFE (dash line) and 2 *wt.*% Terfenol-D/PVDF-TrFE composite (solid line) and (b) the theoretical predictions using the effective modulus theory and the crystallinity-adjusted model.

3.4.5 Magnetization Analysis Results

Figure 3-7 shows the average magnetization for the 0.5 *wt.*%, 2 *wt.*%, and 10 *wt.*% 0-3 Terfenol-D/PVDF-TrFE composite samples as a function of magnetic field up to 2000 Oe, which is well above the onset of magnetic saturation for Terfenol-D of ~1000 Oe. The saturation magnetization of the 10 *wt.*% samples was 22.2 emu/cm^3, nearly 3.82% of the saturation magnetization of bulk Terfenol-D by volume (~1 T). Typically, bulk Terfenol-D has a soft magnetic behavior, whereas Figure 3-7 exemplifies a small hysteretic behavior for the composite samples. Previous research showed that milling Terfenol-D caused a magnetic hardening effect due to the introduction of dislocations, a higher energy barrier for the magnetic domains to cross, resulting in irreversible remanent magnetization [8]. The lack of hysteresis for the 0.5 *wt.*% sample

was attributed to the lesser filler content, i.e., a further separation distance between the particles, reducing the particle-to-particle magnetic flux interaction.

The magnetization response of Terfenol-D filled composite samples appeared to scale logarithmically as a function of the weight fraction of the magnetic particles. For example, the response of the 10 *wt.*% samples was 1.32x higher than the 2 *wt.*% samples, while the latter was 2.3x greater than the 0.5 *wt.*%. The dichotomy between the expected and reported increase in magnetization can be explained by considering the orientation and packing of the particles within the same matrix volume. The particles were randomly distributed during the fabrication process based on the weight and geometry of each particle, i.e., settling vs. buoyancy, and the evaporation rate of the DMF solvent. Each particle, therefore, is a separate and isolated magnetic domain whose contribution is defined based on the magnetic orientation of the other particles in the vicinity. In one scenario, the particles can exhibit either parallel or anti-parallel magnetization while being located side-to-side, where a nonzero resulting magnetization is guaranteed in the parallel situation. Furthermore, the emanating stray field from one particle may result in a demagnetization effect on the neighboring particles. In another scenario, the particles may assume any of the magnetic orientations while being stacked vertically one above the other. In either of these situations, a nonzero net magnetization is expected. The random distribution of the Terfenol-D particles within the PVDF-TrFE samples warranted the conditions for the existence of the previously mentioned scenarios, hence the nonlinear scaling of magnetization with respect to the particle weight ratio. The mobility of the particles within the PVDF-TrFE matrix is discussed in detail later. Nonetheless, the mere existence of Terfenol-D particles dramatically changed the

magnetic behavior of PVDF-TrFE in addition to the electrical response and the molecular structure, as discussed previously.

The efficacy of the 0-3 composites for energy applications relies on their potency for attracting magnetic flux, which is succinctly captured by the susceptibility. The data in Figure 3-7 was used to apply a linear fit to the magnetization-magnetic field response below 500 Oe, the slope of which was taken to be the susceptibility of the different sample configurations. The susceptibility for the 0.5 *wt.*%, 2 *wt.*%, and 10 *wt.*% composite samples is 0.085, 0.178, and 0.215, respectively, compared to the susceptibility of bulk Terfenol-D that ranges from 2 to 10.

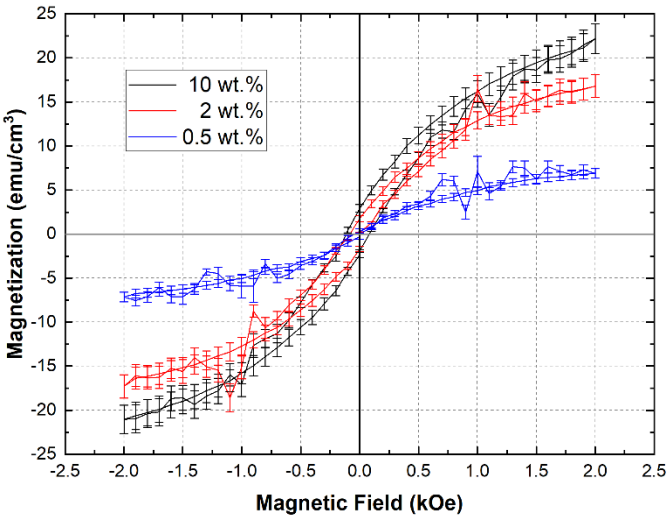

Figure 3-7: Magnetization of the 0-3 composite samples at different weight fraction, showing the magnetic response where increasing the weigh fraction of Terfenol-D ehanced magnetizatio.

3.4.6 Magnetoelectric Analysis Results

Figure 3-8a is a plot of the field-sweep direct magnetoelectric response of the Terfenol-D/PVDF-TrFE 0-3 composite samples with different weight fractions of the magnetic particles at

a monofrequency of 4kHz. Generally, the DME appeared to be insensitive to the testing condition, i.e., constant field, but was dependent on the field direction (see inset in Figure 3-8a). The average α_{33} (along the thickness) was 43±3 mV/Oe·cm, regardless of the weight fraction of the magnetic particles. The α_{31} (along the length) was directly proportional with the Terfenol-D weight fraction, reporting the value of 15.7, 33.4, 61.5 mV/Oe·cm, for the 0.5 *wt*%, 2 *wt.*% and 10 *wt.*%, respectively. Remarkably, the α_{31} for the 10 *wt.*% samples reported a 180% improvement compared to the α_{31} for the 2 *wt.*% counterparts, while the length-wise DME coefficient of the latter was nearly twofold higher than the coefficient of 0.5 *wt.*% samples. The interdependence of the magnetoelectric coupling on the weight fraction is consistent with previous predictions by theoretical and computational models [15], [16] and attributed to three possible mechanisms.

1- The reduction of the electroactive matrix by increasing the weight fraction of the magnetic particles hinders the potential of magnetic to electric energy conversion.
2- Terfenol-D particles act as pinning sites within the PVDF-TrFE crystalline structure, inhibiting the formation of the desirable β-phase at higher loading ratios, as discussed in the previous sections.
3- Increasing the weight fraction of the Terfenol-D particles entices the probability of agglomeration and particle-to-particle interactions, negating the sought-after strain transduction process.

On the other hand, increasing the weight fraction of the magnetic particles improved the efficacy of the magnetoelectric coupling, i.e., resulting in a higher DME coefficient, however, not with linear proportional scale, as discussed previously. Such an improvement is desirable in energy extraction since it increases the available power for end-use applications. These results are in excellent agreement with the previous reports of other 0-3 composites made with different

constituents and exemplify a higher DME coupling [10], [25]. The expected extracted power for the 10 *wt.*% is estimated to be 100 μW at the maximum magnetic field of 3000 Oe. Similarly, the extracted power for the 0.5 *wt.*% and 2 *wt.*% is forecasted to be ~25 and ~50 μW. These power values are sufficient to power many small implantable devices, such as pacemakers and biosensors [26].

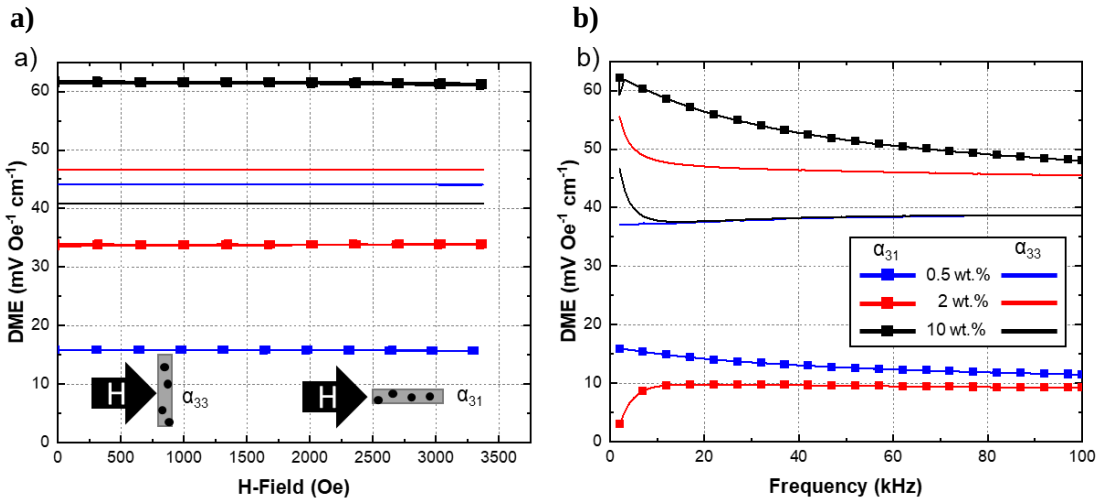

Figure 3-8: Magnetoelectric coupling of the Terfenol-D/PVDF-TrFE composites (a) field-sweep at a monofrequency of 4 kHz and (b) frequency-sweep at a constant magentic field of 650 Oe.

The spectral response of the magnetoelectric coefficients (Figure 3-8b) exhibited similar behavior, as discussed above, reporting a nearly constant α_{33} and α_{31} as a function of frequency, ranging from 1 to 100 kHz. Below 15 kHz, the α_{31} response decayed from an apparent maximum at low frequencies, except for the case of the 2 *wt.*% samples where the DME increased to reach the steady-state value. The higher response at low frequency translates to a larger potential of extracted power, leading to the selection of 4 kHz for the measurements discussed above as a function of a varying magnetic field. The α_{33} also remained nearly independent with respect to the weight fraction of the Terfenol-D, similar to the behavior in Figure 3-8a and attributed to the same

reason. On the contrary, the spectral values of the α_{31} showed a high dependence on the weight fraction. The average α_{31} coefficients for the 0.5 *wt.*%, 2 *wt.*%, and 10 *wt.*% were 12.8, 9.5, and 52.1 mV/Oe·cm, within the frequency range of 15kHz to 100kHz. The spectral variance in the DME response is believed to be due to the particle mobility within the PVDF-TrFE matrix (discussed next) analogous to the motion of colloidal in a viscous fluid. It is worth noting that nearly all of the samples exhibited short circuit behavior after extended testing, further substantiating the particle mobility hypothesis. To verify, we conducted a tangent experiment where several samples were microscopically observed in the presence of DC and AC magnetic fields.

3.5 Modeling of Failure Mechanism

The properties and performance mapped in the previous subsections (summarized in Table 3-1) and those reported a *priori* in the literature point to a perplexing behavior contrary to the technological potential commonly hyped by theoretical models of 0-3 magnetoelectric composites [15]. For example, the magnetoelectric response reported above is inferior to the theoretical and computational predictions, where both are forecasted ~125 mV/Oe·cm for the 10 *wt.*% case. It is worth noting that many of the samples investigated herein reported a short-circuit condition after prolonged testing despite starting as an open-circuit. The latter is consistent with the forecasted behavior based on the dielectric properties of the PVDF-TrFE matrix. It was then hypothesized that particle mobility and migration are responsible for the electrical breakdown, deeming the samples futile. Three practical rationales are substantiating this hypothesis:

1. A few samples survived the electrical polarization process, leading to the addition of the separator layer during poling in the current study and proceeding to the characterization of unpoled samples.

2. The surprising TGA results, showing insensitivity to the magnetic field while it was expected to shift the thermal response.
3. The testing temperature (i.e., room temperature) coincided with the rubbery region of the thermomechanical response of PVDF-TrFE, based on the DMA results mentioned above.

Table 3-1: Summary of experimental results.

	β-phase content	Crystallite Size (Å)	Decomp. Temp. (°C)	M_s emu cm^{-3}	α_{31} mV/Oe·cm
Neat	0.670±0.014	81.65	417.10±0.50	--	--
0.5 wt.%	0.684±0.009	103.65	407.14±0.20	7.3±0.6	15.7
2 wt.%	0.699±0.009	107.86	391.20±3.04	16.8±1.3	33.4
10 wt.%	0.696±0.021	119.50	413.08±2.79	22.2±1.7	61.5

Therefore, electrode-free samples were microscopically observed in the presence of a DC magnetic field of 650 Oe and an AC magnetic field of 16 Oe at a frequency of 4 kHz to provide evidence for the proposed failure mechanism. A series of photographs were captured using an in-house built microscope mounted above the samples. Analysis of the images showed several Terfenol-D particles moving into and out of the picture frame while other particles mobilized within the frame in different directions. The particle mobility is then attributed to the force balance between the magnetic force due to the application of the magnetic field and the viscous drag force from the viscoelastic properties of PVDF-TrFE. A 2D dynamic model was developed to describe the motion of two spherical magnetic particles based on Newton's law, which is described by the force balance

$$m\frac{d\vec{v}}{dt} = \vec{F}_m + \vec{F}_v \tag{3-6}$$

where, $\vec{F}_m$ and $\vec{F}_v$ are the magnetic and drag forces, respectively, m and v are the mass and velocity of the particle, respectively, and t is time. The magnetic particles radiate a nonuniform magnetic flux, allowing attraction or repulsion of nieghboring particles. For an external magnetic field applied in the *y*-direction, the magnetic force can be decomposed into

$$\begin{bmatrix} F_{m,x} \\ F_{m,y} \end{bmatrix} = \frac{4\pi\mu_o\chi^2H^2R^6}{3r^4}\begin{bmatrix} (1-5\cos^2\theta)\sin\theta \\ (3-5\cos^2\theta)\cos\theta \end{bmatrix} \tag{3-7}$$

where, R, r, χ, and θ, are the radius of a particle, the distance between the two particles, the magnetic susceptibility, and the angle of the particle alignment with respect to the applied magnetic field, respectively. The viscous drag force is given by Stoke's law,

$$\vec{F}_v = -6\pi R\eta\vec{v} \tag{3-8}$$

where, η is the viscosity of the matrix. Other forces, including electrostatic, Brownian motion, and dynamic magnetic forces, were initially considered, but they were found negligible compared to the forces shown in Equations 3-3 to 3-8. The particle motion was then simulated by selecting initial locations using explicit calculations with a timestep below the Courant limit [27]. One particle was stationary, while the second particle was free to move based on the solution of Equations 3-8 to 3-10. The material properties used for this simulation were extracted from the previous subsections. The viscosity of PVDF-TrFE was taken to be 10 kPa·s, and the density of Terfenol-D was assumed to be 9210 kg.m^{-3} [28].

The particle mobility model was solved for multiple starting alignments of the particles, demonstrating the possible paths the particles may take, as has been experimentally observed. Figure 3-9a shows the simulated path for different starting angles (0°, 15°, 30°, 45°, 60°, 75°, 90°) with respect to the direction of the external bias magnetic field. The starting distance between the particles used in Figure 3-9a is the average distance between particles for a 10 *wt.*% composite sample. The plotted trajectory line tracks the locations of the center of the particle at 50 s time increments. In other words, the distance between subsequent locations (i.e., different markers on the line plot shown in Figure 3-9a is related to the velocity of the particle. Thus, fewer points on the trajectory path correlate with less time for the particle to reach its final destination, i.e., coinciding with the stationary particle. Every starting particle position, except for the 90°, leads to the particles eventually making contact; however, the time to reach the final destination increased exponentially based on the starting angle due to the longer path and lower attractive force. Based on Equation 3-7, any particle positioned at an angle higher than the critical angle (~63°) initially repel but eventually mobilize towards the stationary counterpart as it corrects its orientation within the magnetic field, as seen from the particle starting at 70°. Figure 3-9b shows optical photographs of two selected particle motion scenarios. The particle encircled blue traveled towards the particle encircled gray due to magnetic attraction. Alternatively, Figure 3-9c shows the trajectory of a particle moving perpendicular to the applied magnetic field due to repulsion with the neighboring particle (encircled red). The observed particles appear to move faster than the model suggests, likely due to the difference in the particle geometry being spherical in the latter while being platonic in the physical experiment.

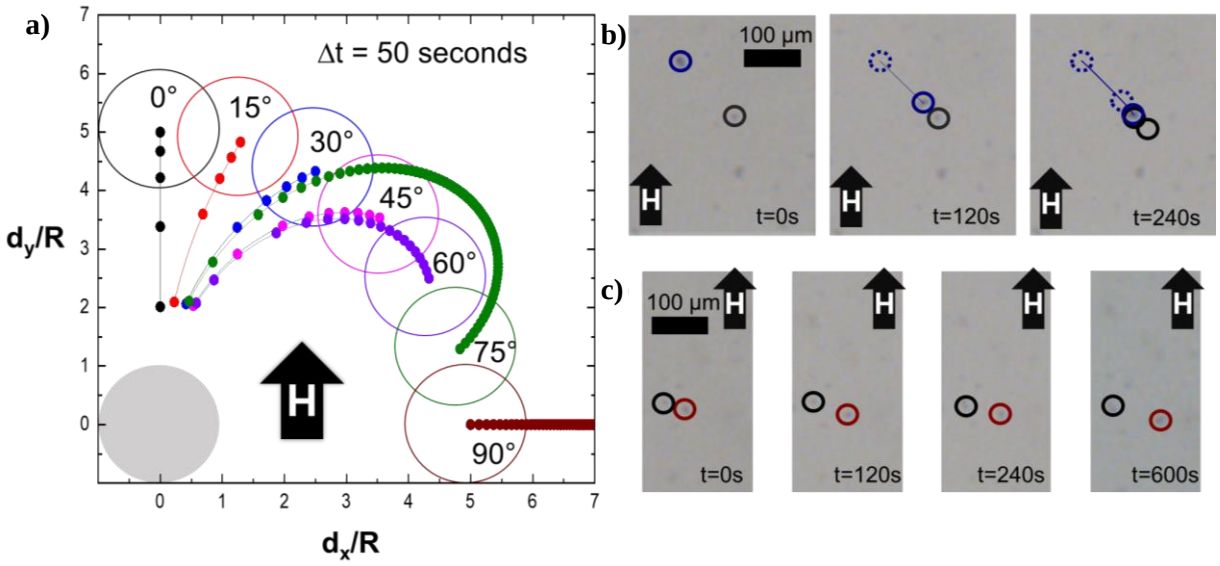

Figure 3-9: (a) Simulated trajectories of magnetic particle motion for different starting angles with respect to the magnetic field, (b) Photograph timeline showing a particle with a ~30° trajectory, and (c) timeline of a particle with an ~80° trajectory.

The phenomena of particle migration and mobility are detrimental to the performance of particulate composites for magnetoelectric or magnetodielectric coupling, leading to performance failure. The accumulation of the particles due to migration may nullify or reduce the magnetoelectric efficiency, deeming the composite unfunctional or inoperable. In the case of 10 wt.%Terfenol-D/PVDF-TrFE 0-3 composite samples, the model presented before predicts the mobility-induced agglomeration to occur within a few hours, which translates to the meager life of a device based on 03 composites. It is worth reiterating that the device life depends on the separation distance to particle size ratio, particle orientation with bias magnetic field, the magnetic susceptibility, and viscosity of the matrix, in addition to operating and environmental conditions. Therefore, longer device life can be achieved by controlling or tuning alignment angle, particle size, weight fraction, using magnetic particles with a low magnetic moment, or matrix with higher viscosity, according to their importance based on the model presented above. Future research

should investigate methods to pin the particles within the matrix through particles and polymer matrix innovations to produce active particulate composites with magnetoelectric coupling functionalities.

3.6 Conclusion

In closing, magnetoelectric particulate composite material, consisting of magnetic Terfenol-D particles embedded into an electroactive PVDF-TrFE, has been investigated using multiscale characterization and modeling approaches. The effect of the weight fraction of the magnetic particles was evaluated, demonstrating the magnetoelectric properties while elucidating the mechanisms responsible for changes in the performance. More specifically, the thermogravimetric analysis demonstrated the resilience of PVDF-TrFE to harsh environmental conditions, protecting the oxidation-prone Terfenol-D particles. The magnetic response of composites provided expected results based on bulk Terfenol-D, substantiating the multi-utility of the PVDF-TrFE matrix. In reciprocation, Terfenol-D improved the ferroelectric behavior of the PVDF-TrFE matrix by enhancing the β-phase content and improving the semi-crystallinity. In addition, the inclusion of Terfenol-D stiffened the PVDF-TrFE matrix, promoting the amendment of the effective modulus model to include the effect of crystallization on the material stiffness. The 0-3 Terfenol-D/PVDF-TrFE composites yielded a similar magnetoelectric coupling as other particulate-PVDF composites. A unique outcome of this research is explicating the effect of particle mobility and migration on the short- and long-term performance of magnetoelectric particulate composites through an analytical model that accounts for the balance between magnetic and viscous drag forces. The mobility of the magnetic particles aspired us to propose several future research directions to close the gap between experimental and analytical predictions of the

magnetoelectric performance of multiferroic particulate composites while providing a fundamental basis for failure.

3.7 Acknowledgments

The authors are grateful to the SDSU Electron Microscope Facility, with data acquired under the support of a National Science Foundation grant (DBI-0955908). The authors additionally wish to express appreciation toward Sophia Do and Nha Uyen Huynh for their assistance in obtaining the scanning microscopy images. The authors also acknowledges the support of the by the United States Department of Defense under Grant Agreement No. W911NF-14-1-0039 for acquisition of Dynamic Mechanical Analyzer and Thermogravimetric Analyzer. The research was also supported by internal funds from San Diego State University.

Chapter 3, in full, has been submitted for publication of the material as it may appear in Smart Materials and Structures 2021. Singh, Anil. Youssef, George. The dissertation author was the primary investigator and author of this paper.

Chapter 4 Colossal crystals in P3HT:PCBM blends for enhanced organic magnetism

Scott Newacheck, Nha Uyen Huynh, and George Youssef

4.1 Abstract

Ferromagnetism in organic blends of poly(3-hexyl thiophene) with phenyl-C61-butyric acid methyl ester (P3HT:PCBM) is known to be highly dependent on the degree of crystallinity. The magnetic response of the blend P3HT:PCBM has been meager due to the relatively small crystalline size. The highest previously reported crystallinity and magnetization for this blend are due to nanometer-scale P3HT crystalline regions with nanometer-scale magnetic domains. The novelty of the work presented herein was the synthesis of colossal millimeter-scale PCBM crystals in the P3HT:PCBM blend, which exhibited large > 20μm magnetic domains based on magnetic force microscopy characterization. The PCBM crystal structure was further analyzed for its composition and structure using scanning electron microscopy, X-ray diffraction analysis, and energy dispersive X-ray spectroscopy, affirming the largest PCBM crystal reported in the literature. The morphology and mechanical properties of the colossal PCBM crystals were analyzed using atomic force microscopy and force-displacement measurements, reporting the phase-dependent mechanical properties. In all, this research pushes organic ferromagnetic materials to be comparable to their inorganic counterparts and feasible to be used in magnetic devices for wearable and flexible electronic applications.

4.2 Introduction

Regioregular poly (3-hexylthiophene) (P3HT) and phenyl-C61-butyric acid methyl ester (PCBM) blends currently rest as a top-performing organic photoactive polymer used in photovoltaic and photomagnetic devices [57]. The blend polymer behaves under an electron donor-acceptor paradigm, where the P3HT absorbs solar light energy, exciting an electron to a higher energy state then donating that electron to the PCBM in the form of a charge transfer exciton [93].

There, the exciton could either be dissociated for photovoltaics or left bounded as an exciton to produce the magnetic spin needed for a photomagnetic response [93], [94]. The effectiveness of P3HT:PCBM to act as a photovoltaic cell or photomagnetic material depends on the efficiency of the light absorbed and the electron transport from the donor to the acceptor [95].

For the first case, i.e., the efficiency of the P3HT:PCBM to absorb light (η_{Abs}), is dependent on the thickness of the film (L) and the extinction coefficient (ε) of the material following the Beer-Lambert law ($1 - \eta_{Abs} = 10^{-\varepsilon L}$). Prior research has reported that the extinction coefficient varies from 2E4 to 4E4 cm^{-1} for P3HT:PCBM blend in the visible light spectrum, depending on the wavelength of the incident light [55]. For 90% absorption efficiency, the thickness of the blend needs to be roughly 250 to 350 nm, resulting in 99% overall absorption efficiency of the incident light after reflection off the far surface [56], [93]. However, P3HT:PCBM films are typically fabricated through a spin-coating process, which results in 50-100 nm thick layers, requiring the deposition of 3+ layers in order to produce films thick enough to achieve a high absorption efficiency [96]. An alternative method to fabricate thick P3HT:PCBM films is drop-casting, which can easily produce films thicker than 1 μm in a single layer, potentially resulting in better crystallinity. The latter is imperative for the photomagnetic functionality of this blend polymer framework.

Previous research exhaustively investigated the effect of the fabrication method, solvent, electrode material, electrode size, annealing conditions, and the addition of dopant on the efficiency of P3HT:PCBM in photovoltaic applications [56], [57]. However, less attention has been devoted to the magnetic response of this blend polymer due to the low magnetic yield, hence weak efficiency. From the limited photomagnetic research done so far, the higher degree of crystallinity of the semi-crystalline P3HT is a contributing factor for enhancing the magnetic

response as well as the light absorbance and charge transfer efficiencies [95], [97]. For example, Ren *et al.* demonstrated that the magnetic response of semi-crystalline nw-P3HT:Fullerene was roughly fourfold higher than their amorphous counterpart, where the magnetization at 500 Oe of the former was 8 emu/cm^3 compared to the latter of 2 emu/cm^3 [97]. It is then the objective of this research study to improve the degree of crystallinity of P3HT:PCBM in favor of enhancing its photomagnetic response. Specifically, we investigate two methods to improve crystallinity and potentially the light absorbance (topic of future work). First, ~100 μm thick films were fabricated via a drop-casting method using *o*-dichlorobenzene (ODCB) solvent and cured in a controlled environment to extend the cure time and, in turn, to provide the necessary conditions to improve the degree of crystallinity. A possible byproduct of increasing the thickness is increasing the light absorption; thus, exciting the electrons required for the magnetic response. Second, a nonsolvent, acetonitrile (ACN), was introduced to the blending process before the deposition of P3HT:PCBM films to further increase the degree of crystallinity of P3HT, which has been previously shown to elicit a higher magnetic response [97]. Furthermore, the samples were fabricated on either silicon or ITO substrates to demonstrate the substrate effect, if any. As a result, the introduction of the longer curing time successfully synthesized large millimeter-scale crystalline regions of PCBM with the desired magnetic response, whereas the addition of ACN and the substrate modestly improved the crystallinity of P3HT.

4.3 Material Fabrication

Regioregular poly (3-hexylthiophene) (P3HT) was first dissolved in ortho-dichlorobenzene (ODCB) in a concentration of 35 mg/mL. Phenyl-61-butyric acid methyl ester (PCBM) was then added in a 1:1 weight ratio with respect to P3HT, to the solution and stirred at 40°C for 15 hours. Half of a milliliter of the solution was drop casted onto a 2.5 x 2.5 x 0.07 cm indium tin oxide (ITO) coated glass substrate (University Wafers) that was previously cleaned with isopropyl

alcohol. A photo of the solution on the ITO substrate is in the supplementary document. Another 1 mL of the solution was drop-cast onto undoped silicon (Si) wafers (University Wafers), also pre-cleaned with isopropyl alcohol. The samples were then left to cure under a petri dish, slowing the cure time up to 2 days to achieve greater crystallinity. The latter was accomplished by increasing the volume of the solution dropped on the substrate while keeping the confinement space constant, i.e., a high volume to surface area ratio, slowing down the natural evaporation process and providing conducive conditions for crystal growth. Naturally, the thickness of the film has increased as a bigger volume was deposited, which was found to be imperative to achieve high crystallite population. Another set of samples, ACN was added at a 10% volume ratio to the P3HT:ODCB solution that was ultrasound mixed for 15 minutes then left overnight to allow for P3HT to crystallize, at which point the PCBM was then added. The same fabrication process was followed as before. Photographs of the four sample types (with or without ACN, on ITO or Si substrates) are shown in the supplementary document. All fabrication steps were performed in an inert N_2 environment while all analyses were done in ambient conditions.

4.4 Results

Figure 4-1(a-c) shows a collage of scanning electron microscope (SEM) micrographs of the two types of samples, i.e., with or without ACN on ITO substrate, to explicate the solvent-dependent morphological changes. Several millimeter-scale PCBM crystals can be seen occupying a large subset of the SEM micrograph shown in Figure 4-1a, where rhombohedral and hexagonal structures are protruding above the surface of the surrounding P3HT:PCBM blend. These features were ubiquitously distributed throughout the surface of all fabricated samples, regardless of the substrate, as shown in the additional SEM micrographs included in the supplementary document. The size and the geometry of the PCBM crystals reported herein are much larger than those previously reported, which are attributed to the controlled environment that slowed the curing time

[98], [99]. Each of the corners of the rhombohedra and hexagon formed angles of ~60° or ~120°, suggesting a hexagonal crystal structure. On the micron-scale, the SEM micrograph in Figure 4-1b reveals multiple 2-5 μm sized ellipsoidal bumps on the top surface of the blend polymer fabricated without ACN. The ellipsoidal bumps were found on and off the large rhombohedra structures. The ellipsoidal bumps were previously observed and explained to be clusters of PCBM, caused by the crystallization of the P3HT expelling the PCBM [100]. Conversely, the P3HT:PCBM blend polymer fabricated with ACN neither possessed the millimeter-scale rhombohedra structures nor the micron-scale ellipsoidal bumps, as illustrated in Figure 4-1c. The absence of the morphologies is likely due to the P3HT crystallizing before the addition of PCBM, which prevented their expulsion and subsequent agglomeration or crystallization during the curing process.

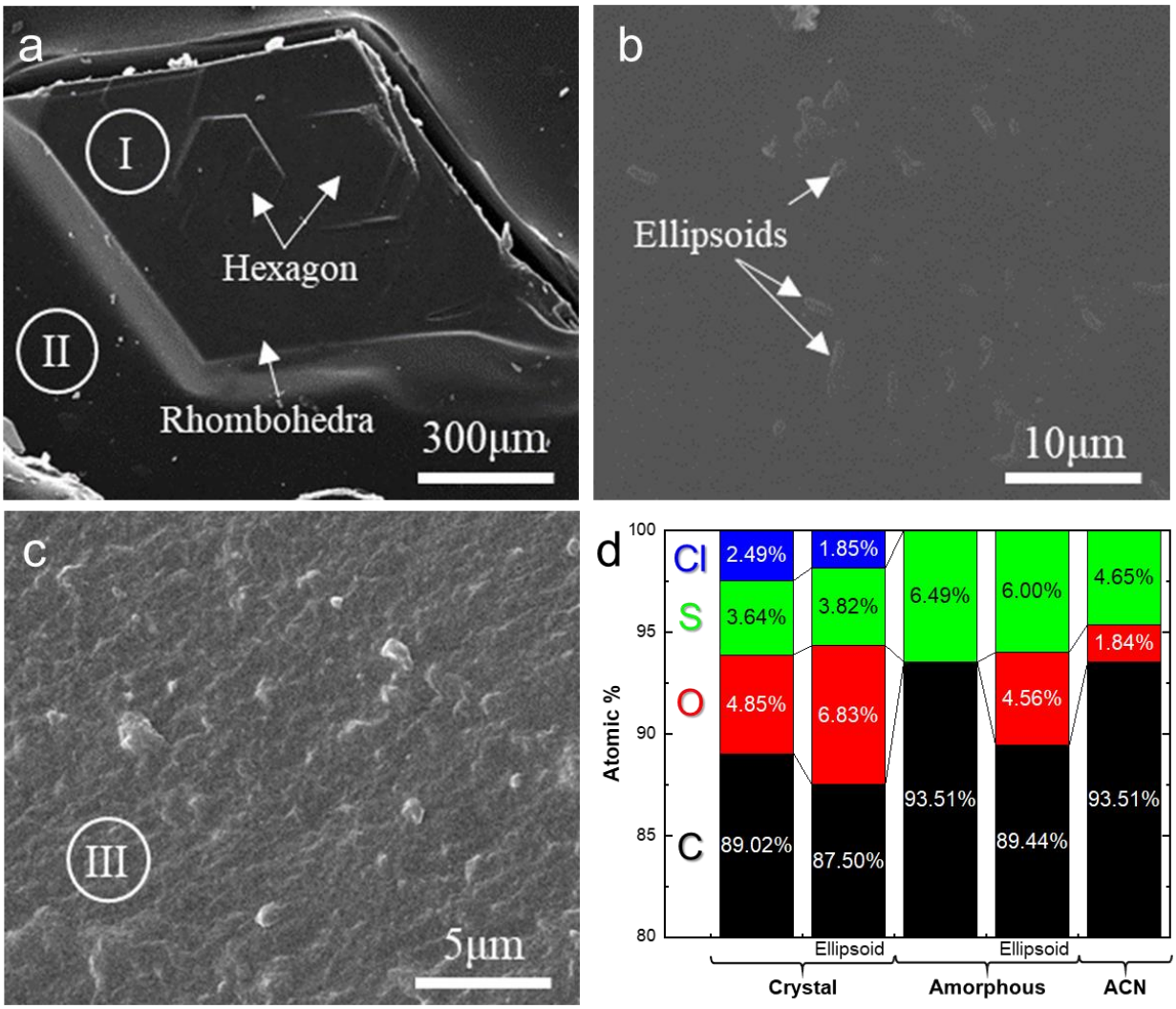

Figure 4-1: SEM micrographs of (a and b) drop-casted P3HT:PCBM fabricated with only ODCB as solvent, and (c) drop-casted P3HT:PCBM fabricated with ACN and ODCB. The millimeter-scale rhombohedral crystal structure is shown in (a) while a close-up surface morphology of (a) is shown in (b), (c) is the morphology of the ACN-based P3HT:PCBM, and (d) atomic percentages of each element measured on each type of surface feature identified in (a-c).

Figure 4-1d shows the EDS elemental analysis of the sample fabricated with acetonitrile [labeled (III) in Figure 4-1c] along with the crystal [labeled (I) in Figure 4-1a] and amorphous [labeled (II) in Figure 4-1a] regions of the sample fabricated without acetonitrile. Additionally, focused EDS spectral analysis was performed on and off the ellipsoids (Figure 4-1b) for both the crystalline and amorphous surfaces of the samples fabricated without acetonitrile. Since oxygen is

only found in PCBM and sulfur is unique to P3HT, the atomic ratio of oxygen to sulfur is related to the concentrations of the constituents, where a 1:1 weight ratio of P3HT:PCBM will yield an oxygen to sulfur ratio of 0.36. The EDS spectra of the crystals encompass relatively high oxygen to sulfur ratio and a notable content of chlorine, indicating a greater concentration of PCBM and some residual ODCB solvent. Conversely, the EDS spectrum of the amorphous region shows trace levels of oxygen suggesting a rich concentration of P3HT. Comparing the elemental traces of the crystal and amorphous regions suggests that the crystal structure largely consists of PCBM and ODCB (referred to hereafter as PCBM crystals), but potentially also includes traces of P3HT due to the persistence of sulfur in the EDS spectra. This is found to be in good agreement with reports in [98]. These large PCBM crystals were likely formed due to the small surface area to volume ratio during curing, causing the surface layer of P3HT to cure quickly and trap ODCB solvent inside. The trapped ODCB solvent could then slowly crystallize with PCBM. EDS analysis of both ellipsoids (on crystal and amorphous surfaces) showed a higher oxygen content than their respective off-ellipsoid surfaces, suggesting that the ellipsoids have a high concentration of PCBM. These ellipsoids were likely formed by PCBM being expelled from the solidifying P3HT during curing. Finally, the chemical composition of the ACN sample was found to be more balanced in oxygen to sulfur ratio (0.39) than the two non-ACN surfaces, suggesting a more homogenous blend. The dichotomy between ACN and non-ACN sample compositional distributions is likely due to P3HT partially solidifying in the ACN-ODCB solution, thus the mixed-in PCBM would not be expelled during curing. The expelled PCBM in the non-ACN sample would either form small ellipsoids on the surface or large crystals underneath.

The crystallinity of the newly synthesized P3HT:PCBM with significantly larger PCBM crystals, which has yet to be reported before, was explicated using an X-ray diffractometer (XRD, Philips XPert) with $\lambda = 1.5404$ Å and at 45 kV, given the importance of the degree of crystallinity for the magnetic response as discussed above. Figure 4-2a is a plot of the XRD spectra for the P3HT:PCBM blends fabricated with or without ACN on different substrates (i.e., silicon or ITO) using the drop-casting deposition method. Regardless of the type of solvent or substrate, a sharp peak was observed at a $2\theta = \sim 5.16°$ associated with P3HT (100), two shallow peaks at 10.6° for P3HT (200), 16.6° for P3HT (300), and one broad peak around 20° corresponding to P3HT (010). Samples fabricated without ACN exhibited five intense peaks at 6.92°, 13.96°, 21.04°, 28.20°, and 35.48°, regardless of the substrate, attributed to the PCBM-ODCB crystals.

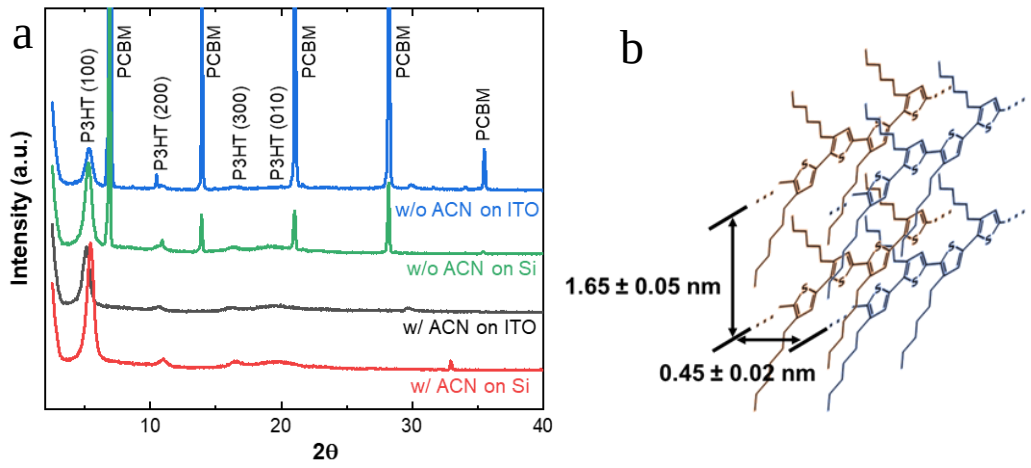

Figure 4-2: (a) XRD analysis of drop-cast P3HT:PCBM films fabricated using only ODCB and using ODCB with ACN on Silicon or ITO glass substrates. (b) Schematic of the P3HT crystallite showing the atomic spacing and stacking alignment.

Table 4-1 quantifies the crystallite sizes (τ) for each distinct peak calculated using the Scherrer equation, $\tau B \cos\theta = \lambda$, where B is the full width at half maximum in radians [101]. The PCBM

crystals were only observed in the non-ACN samples, reporting a crystallite size higher than the allowable limit of the Scherrer equation (> 100 nm), hence the designation in Table 4-1. The PCBM peaks for the non-ACN samples on the ITO substrate have higher intensity than the corresponding peaks on the silicon substrate, suggesting that ITO promotes PCBM crystallinity. A higher degree of PCBM crystallinity improves electron mobility, which is ideal for photovoltaic applications [54]. However, the effect of higher PCBM crystallinity on the magnetic properties remains elusive, discussed later. On the other hand, the spacing and crystallite sizes of the P3HT indicate a crystal geometry that is roughly 1-4 layers in the (010) stacking direction and 6-8 layers in the (100) stacking orientation, based on the values extracted from the XRD spectra and summarized in Table 4-1. The spacing and the stacking configurations are shown schematically in Figure 4-2b. Generally, and based on Table 4-1, the crystallite size of P3HT increased upon the addition of ACN, showing a ~6% increase compared to the absence of this solvent. The silicon substrate and the utilization of the nonsolvent appeared to enhance the P3HT crystallite size, where the latter was expected. In addition to improving the magnetic properties as previously reported [95], [97], crystalline P3HT also improves the hole mobility, thus, additionally enhancing the photovoltaic response.

Table 4-1: Crystallite sizes and interatomic layer distances for P3HT:PCBM.

Sample		P3HT (100)		P3HT (010)		PCBM	
ACN	Substrate	τ (nm)	d (nm)	τ (nm)	d (nm)	τ (nm)	d (nm)
Yes	ITO	13.8	1.7	1.2	0.45	--	--
Yes	Si	14.7	1.6	1.5	0.45	--	--
No	ITO	13.0	1.7	0.6	0.43	> 100	1.28
No	Si	13.8	1.7	1.6	0.47	> 100	1.27

The effect of the nonsolvent and substrate on the degree of crystallinity of P3HT and PCBM can be elucidated via measurements of the mechanical and topographical properties, which were characterized using an atomic force microscope (AFM). The mechanical properties are reported in terms of the plane-stress stiffness parameter, $E/(1-\nu^2)$, given the kinematical configuration of the studied films, while the surface roughness was used as a metric for the topographical properties. The plane-stress stiffness of the samples was obtained by applying a maximum force of 14-20 mN, while measuring the indentation depth through the Oliver and Pharr model [102] in Equation 4-1 and applying the approach outlined in [103].

$$\frac{E}{(1-\nu^2)} = \frac{1}{\frac{(h_{max}S-\varepsilon P_{max})}{0.18S^2} - \frac{(1-\nu_i{}^2)}{E_i}} \tag{4-1}$$

Where, E_i and ν_i are the Young's modulus (170 GPa) and Poisson's ratio (0.27) of the indenter, respectively, S is the slope of the load-elastic displacement curve, ε is a geometry constant based on the indenter, and P_{max} and h_{max} is the maximum load applied and maximum indentation depth measured, respectively. The resultant material stiffness metrics were averaged over 15 isolated indentations, while the surface roughness for each sample was calculated based on the topography

collected from a 50x50 μm^2 area. Figure 4-3 summarizes the stiffness metric and surface roughness for samples fabricated with the nonsolvent, as well as on and off the PCBM crystals.

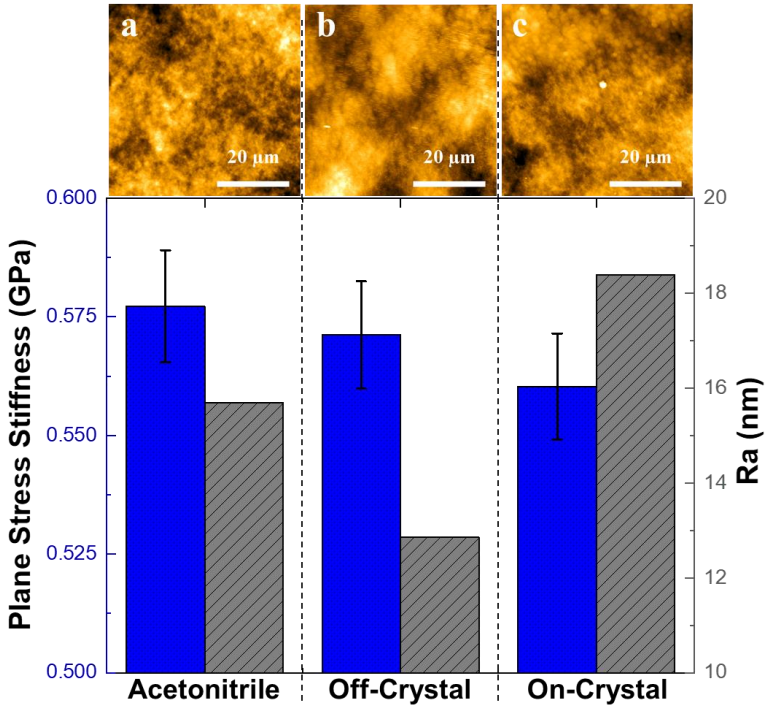

Figure 4-3: (top panel) AFM topography scans of drop-cast P3HT:PCBM with (a) ACN, (b) off and (c) on the PCBM crystal. (bottom panel) Calculated surface roughness and plane stress stiffness.

The results of the t-test confirm a statistically significant difference between the stiffness on and off the PCBM crystals ($p = 0.0048$). A similar statistical significance was found when comparing the PCBM crystal results and the ACN sample ($p = 0.0004$). However, the difference in the stiffness for the ACN and off-PCBM crystal surfaces were statistically insignificant ($p = 0.17$). In general, the rhombohedra surface was found to be slightly softer (< 5%) and moderately rougher (> 15%) than the other measured surfaces. The compliant behavior of the PCBM crystal is believed to be due to the residual solvent and the relatively high roughness. It is important to

note that the stiffness parameter shown in Figure 4-3, and discussed above, is defined based on the Poisson's ratio (no assumptions were made of the Poisson's ratio), which may be different for the amorphous, PCBM crystal, and P3HT semi-crystalline regions, explicating the apparent softening response of the PCBM crystal. The residual solvent was previously reported in the EDS spectra (Figure 4-1d). Meanwhile, a rougher surface may lead to a higher exciton decomposition, which is favorable for photovoltaic efficiency but potentially disadvantageous for magnetic behavior [54].

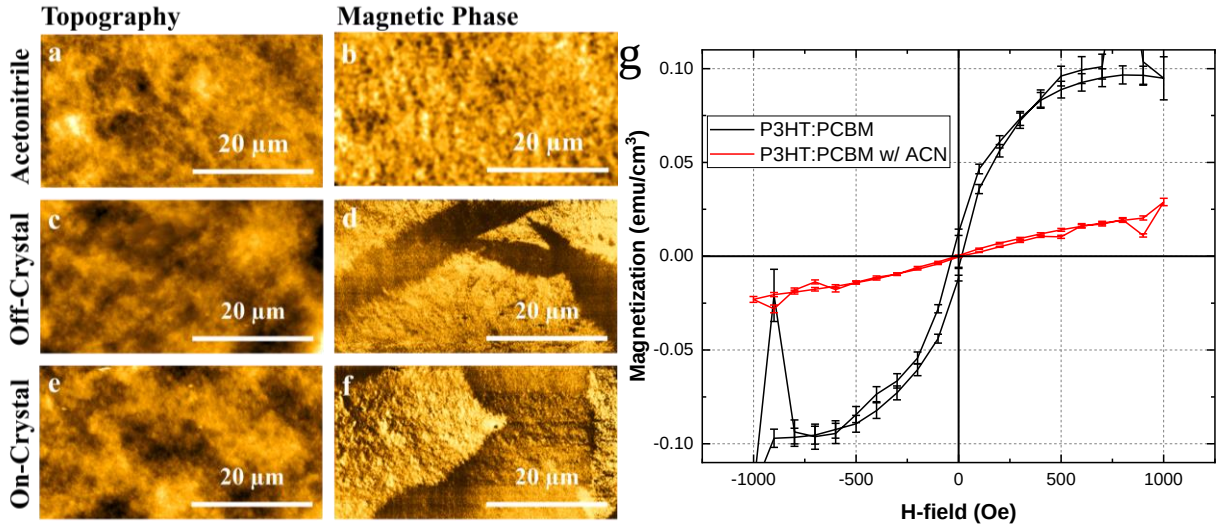

Figure 4-4: MFM results (left column is topography and right column is magnetic phase) for samples fabricated (a & b) with ACN, (c & d) off and (e & f) on the PCBM crystal. Dark and bright regions exemplify different magnetic domains. (g) The effect of acetonitrile on the magnetization of P3HT:PCBM showing that the addition of ACN decreases the magnetic response.

Finally, the magnetic attributes of the newly synthesized P3HT:PCBM blends are elucidated in the MFM phase scans shown in Figure 4-4, regardless of the solvent. Well defined magnetic domains are observed on both surfaces (on/off PCBM crystal) of the samples fabricated without ACN (Figure 4-4d and f). However, it should be noted that the magnetic phase was infrequently observed off the PCBM crystals, or in other words, multiple scanning areas were

taken to locate a magnetic response such as the one seen in Figure 4-4d. Meanwhile, a magnetic response was easily evident at nearly every scan taken on the PCBM crystal (see additional MFM scans in the supplementary document). The magnetic domains were notably larger on the PCBM crystal, further substantiating the magnetic superiority. Therefore, we consider that the PCBM crystals improve the magnetic response of the blend polymer, as hypothesized earlier. Remarkably, the colossal PCBM crystal reported herein are larger magnetic domains than any other organic magnetic material, to our knowledge, and comparable to many inorganic ferromagnets. The magnetic phase was also observed in the ACN samples (Figure 4-4b) with a similar nanoscale domain configuration as previously reported for P3HT:C60 films [97]. As previously discussed based on the MFM results, the PCBM crystals had a much greater magnetic response than the high P3HT crystallinity sample, as shown in Figure 4-4g. In contrast, the samples fabricated with acetonitrile exhibited a very similar response to the P3HT:PCBM samples reported by Majumdar *et al*., where the magnetic behavior appears to be a juxtaposition of paramagnetism and ferromagnetism [104]. The strong paramagnetic response is attributed to a greater dissociation of the electron-hole pair; thus, the exchange interactions are too weak to impose a strong ferromagnetic ordering. Overall, the giant PCBM crystals and the high P3HT crystallinity samples portrayed a soft magnetic behavior with remanent magnetization of 11 memu/cm^3 and 0.4 memu/cm^3, and coercive magnetic fields of 9.4 and 0.3 Oe, respectively.

Based on the above discussion and previous reports, the PCBM crystallinity (our results herein), as well as P3HT crystallinity (e.g., reports by [95], [97]) have been independently shown to be favorable in obtaining a magnetic response. However, the preceding discussion indicates the details of the fabrication process promotes the growth of either PCBM or P3HT crystals but not both concurrently. Hence, it is concluded that PCBM crystallinity is more conducive than P3HT

crystallinity for ferromagnetism, which is likely due to stronger exchange interactions of the excited electrons. These exchange interactions from the PCBM crystals could be the driving force to align spins in neighboring PCBM molecules to behave ferromagnetically instead of paramagnetically or antiferromagnetically, which was a limitation in a previous model about the origin of ferromagnetism in P3HT:C60 blends [105].

4.5 Conclusion

In summary, we demonstrate viable approaches to fabricate highly crystalline thick P3HT:PCBM films with a magnetic response. On the one hand, increasing the thickness resulted in large millimeter-scale PCBM crystals with large distinct magnetic domains and notable crystallite sizes. On the other hand, the incorporation of a nonsolvent improved the crystallinity of P3HT. In all, the higher degree of crystallinity improved the magnetic response; however, the coexistence of PCBM and P3HT crystals was found to be limited by the fabrication approach. In contrast with previous studies, we reported the largest PCBM crystals, which found to be more favorable for ferromagnetism than the P3HT semi-crystallinity. Future studies will focus on quantifying the magnetic response of the P3HT:PCBM films for modeling and application purposes.

4.6 Acknowledgements

Chapter 4, in full, has been submitted for publication of the material as it may appear in Crystal Growth and Design 2021. Huynh, Nha Uyen. Youssef, George. The dissertation author was the primary investigator and author of this paper.

Chapter 5 Polymer-based multifunctional electronic devices

Scott Newacheck, Nha Uyen Huynh, and George Youssef

5.1 Abstract

This letter presents a physical demonstration of a multifunctional electronic device based on an organic multiferroic fabricated with a newly fabricated P3HT:PCBM with a colossal crystal size. The novelty of the presented framework is the insensitivity to the fabrication process. That is a device with drastically different functionality is made using the same processing steps as a device operating in a completely different regime. In here, we demonstrate, a non-contact magnetic field sensor based on magnetoresistivity. Remarkably, the same device exemplifies a magnetic data storage characteristic.

Keywords: organic magnetoresistance, organic ferromagnetic, organic crystals

5.2 Introduction

Heterojunctions of polythiophenes polymers, e.g., Poly 3-hexylthiophene-2,5-diyl (P3HT), blended with fullerene derivative molecules, e.g., Phenyl-C61-butyric acid methyl ester (PCBM), are at the forefront of the organic photovoltaic industry and have been recently emerging in organic ferromagnetism and organic magnetoresistance (OMAR) transistor technologies [1], [2]. However, field-dependent and voltage-dependent magnetoresistant behavior remains debatable within the possibilities of multiple particle-spin interaction mechanisms. This research aims to uncover the potential underlying interactions responsible for the response for OMAR in the concurrent presence of electric and magnetic field. Elucidation of these mechanisms suggest the potential for multifunctional devices based on organic semiconductors. For example, magnetoresistance is an imperative mechanism for spintronic applications, where organic-based systems promote the development of flexible and transparent magnetic field sensors and computer memory [3].

It has been generally observed that the individual constituents, i.e., fullerene-derivative molecules and polythiophenes, and their heterojunctions usually have positive magnetoresistances (although negative is also possible) and can be sensitive to small magnetic fields. Majumdar *et al*. reported a 13% positive magnetoresistance for P3HT:PCBM when submitted to a 300 mT magnetic field and first attributed the effect to enhanced Columbic attractions of the electron-hole pairs [4]. Many other mechanisms have been proposed to explain the source of magnetoresistance such as triplet-polaron interactions and bipolaron formation; however, this topic is still a matter of debate [3], [5]. Triplet-polaron interactions was first demonstrated by Ern and Merrifield [6] to explicate fluorescence of organic crystals, then later discussed in terms of magnetoresistance by Desai *et al*. [7]. The model suggests that triplet excitons and polarons scatter, resulting in a charge carrier mobility reduction. The application of a magnetic field could quench the triplets (e.g., triplet-triplet annihilation), thus leading to less scattering events and decreasing the resistance. The bipolaron mechanism, proposed by Bobbert *et al*., is explained by bipolaron and polaron spin blocking interactions, locking the charge carriers [8]. The density of bipolarons is magnetic field dependent and their formation is either positively or negatively correlated depending on the distance of their coulombic repulsion. Finally, Majumdar *et al*. later reported a strong correlation between the magnetoresistance and magnetization of P3HT:PCBM blends, a consideration that many models seem to neglect, suggesting that a source of magnetoresistance could be similar to those observed in inorganic ferromagnetic materials [9].

Organic ferromagnetism was observed with P3HT:C60 blend and it was reported that the magnetic behavior exhibited both Villari magnetostriction and converse magnetoelectricity [10]. The response was illumination and P3HT crystallinity dependent [10]. Ferromagnetism was also reported in P3HT:PCBM blends and observed that the magnetic behavior is dependent on charge

transfer efficiency, orientation, illumination, and P3HT crystallinity [11]. Thus, it has been hypothesized that increasing the crystallite size may translate into an enhanced magnetic response. Indeed, large millimeter-scale PCBM crystals were recently synthesized within P3HT:PCBM blends, where the PCBM crystals exhibited the largest magnetic domains (on the order of dozens of microns) of any organic magnetic material (typically on the order of a few nanometers). Those studies did not conclusively explore the mechanisms for the magnetic field effects on these organic semiconductor polymers with exceptionally large 'colossal' crystallites. In this study, the magnetoconductivity, i.e., magnetoresistance, and the ferromagnetic response of P3HT:PCBM blends with the large PCBM crystals are measured and the mechanisms are explicated.

5.3 Results

Remarkable outcome of this the synthesized organic polymer framework (see methods) is the colossal crystal size that yet to be reported in the literature, which was attributed to enhancement of the volume to surface area ratio [12]. Figure 5-1 represents multiscale characterizations of this organic framework, including the results of microscopy and spectroscopy techniques. The optical image in Figure 5-1a demonstrated the ubiquity and size of the PCBM crystals, visible to the naked eye. The P3HT and the PCBM remain as separate phases even during the mixing process, where the P3HT starts to solidify displacing the PCBM molecules closer to each other given rise to colossal crystal formation. Figure 5-1b is a SEM micrograph exemplifying the shape and morphology of the rhombohedral PCBM crystals, which were ubiquitously and repeatably (several batches were studied) found throughout the samples. Congruent study using energy dispersion spectroscopy exploited the elemental composition of these crystals, verifying its PCBM nature [12]. The prime interest in P3HT:PCBM stems from its intrinsic magnetic and

electrical properties when combined situates this polymer framework at the forefront of electronic devices. Figure 5-1c shows MFM micrographs of the P3HT:PCBM crystal, elucidating large magnetic domains that were consistently found on the crystals. Figure 5-1d shows the conductivity map of P3HT:PCBM using C-AFM, where the map illustrates a network of high conductivity domains clustered around regions of relatively high resistance. The contrasting conductivity regions are attributed to the dispersion of PCBM through the P3HT matrix. Finally, Figure 5-1e shows XRD spectra, demonstrating the crystallinity of P3HT:PCBM.

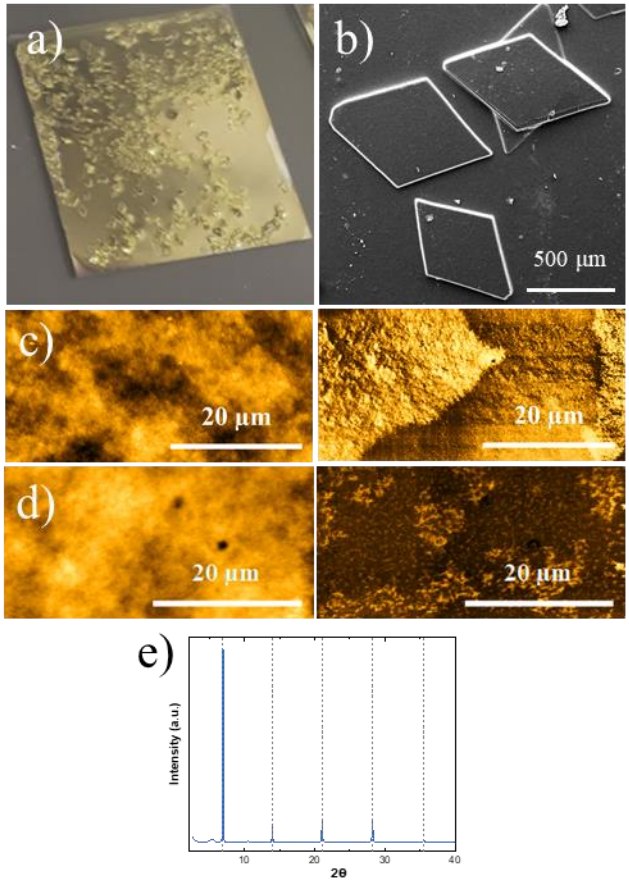

Figure 5-1: (a) optical image of the synthesized P3HT:PCBM, showing high distribution of colossal crystals throughout the visible surface, (b) an SEM micrograph with high magnification of the morphology and geometry of the PCBM crystals, (c) MFM scan demonstrating the magnetic phase of the P3HT:PCBM crystal, (d) C-AFM mapping of surface conductivity of P3HT:PCBM exemplifying conductive domains surrounded by regions of high resistivity, and (e) XRD spectra elucidating the crystallinity of the organic framework.

The volumetric magnetization curve of the P3HT:PCBM crystal blend is plotted in Figure 5-2a. Overall, the giant PCBM crystals and the high P3HT crystallinity samples portrayed a soft magnetic behavior with a negligible remanent magnetization of 6.4 memu/cm^3 and a low coercive magnetic field of 9.4 Oe. The soft ferromagnetic behavior implies that the P3HT:PCBM crystals have a trace quantity of pinning sites, thus improving the amount of reversible magnetization, which is beneficial for switchable magnetic applications. Comparatively, the colossal P3HT:PCBM crystals exemplifies a notably large magnetic saturation surpassing many notable room-temperature organic ferromagnetic materials such as PANiCNQ (0.1 emu/g), 1,3,5-Trizaine (0.04 emu/g), single layer graphene (0.02 emu/g), and even other P3HT:PCBM films fabricated without these colossal crystals [9], [13]–[15]. The enhanced magnetic response is attributed to the crystallinity of PCBM acceptor which strengthens the exchange interactions of the unpaired electrons while weakening the electron-phonon interactions.

The conjugated π-bonds of P3HT allows for an electrically conductive behavior, while the donor-acceptor paradigm of P3HT:PCBM composite results in a semiconductor-type behavior. Figure 5-2b is a plot of the I-V curve measured on the top surface of the sample while an aligned DC magnetic field was applied and varied (schematically shown in the inset). The brass needle probes were placed 5 mm apart, which allowed for multiple colossal crystals to be within the current path. The results plotted in Figure 5-2b also points to a nonsymmetric response with respect to the iteration number of the applied voltage at low levels of magnetic fields. For clarity, the first iteration is plotted in the third quadrant while the second is plotted in the first. At moderate magnetic fields, the I-V curve becomes quasi-symmetric irrespective of the run iteration. For example, the I-V curve exhibited a quasilinear response in the first quadrant while being highly nonlinear in the third quadrant in the absence of a magnetic field (black line in Figure 5-2b). On

the other hand, the I-V curves are unevenly linear with respect run iteration of the electric field at moderate biasing magnetic fields, i.e., the curves in the first and third quadrants characterized by different slopes. The change in the I-V curve is attributed to the potential alignment of the magnetic spins along the direction of the bias field, thus enhancing the electron transport phenomena, effectively evolving the response from a nonohmic to ohmic response. Finally, the presence of high magnetic fields (above 2000 Oe) hinders the conductivity, possibly due to magnetic field mechanisms discussed later.

The iteration number during the magnetoresistance measurements results in two distinctly different behaviors, field-dependent in one case and field-switchable in the other. Figure 5-2c is a plot of the magnetoresistance measurements, which were calculated using $MR = [R(B) - R(0)]/R(0)$, where $R(0)$ and $R(B)$ are the resistances in absence and under the applied magnetic field, respectively, at a constant voltage (5V). On the first run, a field-switchable response occurs where a large 75% drop in resistance is observed upon the application of a small magnetic field (200 Oe) and a negative voltage is applied. Thereafter, further increase of the magnetic field results in a relatively constant magnetoresistance. For every run afterwards, the magnetoresistance exhibits a near linear response with respect to the increasing magnetic field with a slope of 22 %/kOe, as shown in Figure 5-2c. After a magnetic field of 3 kOe, the reversion response discussed before becomes pronounced, caused by the magnetic field effects. The dichotomy of the P3HT:PCBM response across a positive and negative voltage is believed to be associated with spin-orbit mechanisms that prohibits spin scattering of the latter. Overall, the duality of the field-dependent and field-switchable behaviors of P3HT:PCBM enable their use in organic magnetic field sensors due to the linearity of the magnetoresistance/magnetic field

response and organic magnetic memory systems due to the ability of the magnetic field to turn ON/OFF conductivity.

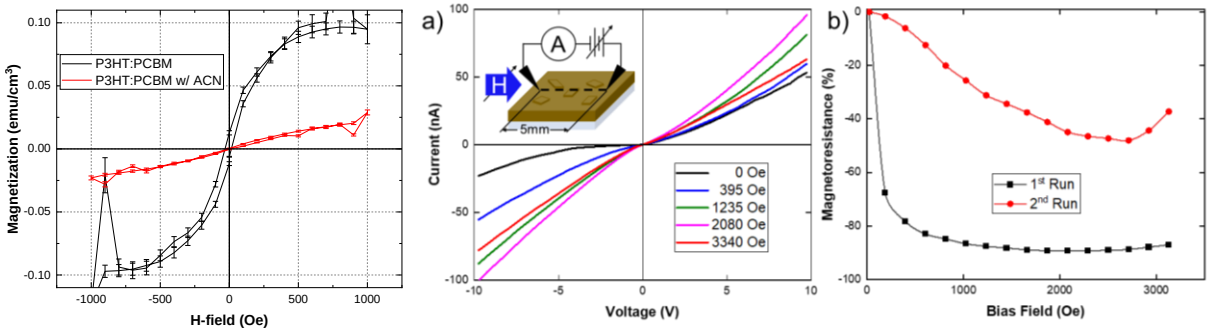

Figure 5-2: (a) Magnetic hysteresis loop of P3HT:PCBM with colossal crystals. (b) Current-Voltage curves of P3HT:PCBM at different magnetic field strengths ranging from 0 to 3400 Oe. (c) Deduced magnetoresistance response of P3HT:PCBM based on the electromagnetic data reported in (b).

The magnetoresistance behavior in Figure 5-2c reveals the potential mechanisms at play when the material is submitted to electrical and magnetic fields concurrently. The initial run curve in Figure 5-2c exhibits a negative Lorentzian magnetoresistive behavior, which can be explained with the e-h pair and bipolaron mechanisms proposed by Prigodin *et al.* [114] and Bobbert *et al.* [112], respectively. In these models, the charge carrier mobility is limited within hyperfine fields but can be released (or exacerbated, leading to a positive magnetoresistance) when an external magnetic field is applied. Further increasing the magnetic field has negligible effects on the resistance once the hyperfine field is considered insignificant and the charge carrier mobility has been unleashed. On the other hand, consecutive iterations results in a negative pseudolinear magnetoresistive behavior, also explained by the bipolaron mechanism based on a different rate of polaron hoping [112] and/or by the excitonic pair mechanism [115]. Finally, a reversal of the magnetoresistance is observed in the presence of magnetic field exceeding 2000 Oe, which could

be due to classical magnetoresistance that typically requires large magnetic fields to have a meaningful effect.

Here, we demonstrate the control of magnetoresistive response of P3HT:PCBM using a magnetic field. The latter plays a role in spin-orbit interactions leading to a switchable behavior. Figure 5-3 exemplifies a uniform magnetic field of 600 Oe switches the current, leading to a magnetoresistance of 11±3% for any magnetic field beyond 200 Oe (See Figure 5-2c). Moreover, the results in Figure 5-3 substantiate the multifunctionality of this organic composite system. Ren *et al*. postulated the application of these novel class of materials in spintronics, which is demonstrated herein via suitability of this material system for two different applications. However, the long-term repeatability of the field-switchable response (in order of millions of cycles) has not been investigated.

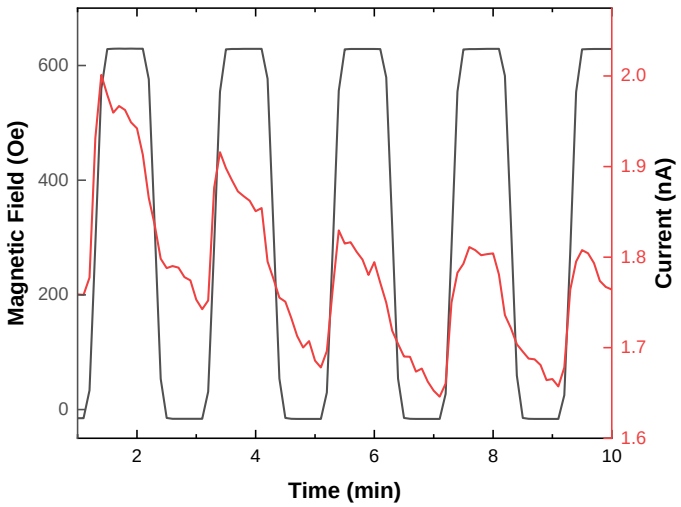

Figure 5-3: Magnetic field switchable magnetoresistance effect in P3HT:PCBM under continuous illumination of white light at room temperature. The magnetoresistance was measured in the same direction of the magnetic field along the sample surface.

5.4 Experimental Methods

Regioregular poly (3-hexylthiophene) (Rieke Metals) was completely dissolved in ortho-dichlorobenzene (ODCB) with a concentration of 35 mg/mL. Phenyl-61-butyric acid methyl ester (Nano-C) was then added to the solution in a 1:1 weight ratio with respect to P3HT and stirred at 40°C for 15 hours. The solution was drop casted onto 2.5" x 2.5" glass substrate, previously cleaned with isopropyl alcohol. Samples were then left in a controlled environment to cure for enhanced crystallinity. All fabrication steps were performed in an inert N_2 environment while all analyses were done in ambient conditions.

The morphology of the fabricated samples was examined under an electron microscope (FEI Quanta 200), while the magnetic phase was detected using magnetic force microscope (AFM Workshop TT1). The crystallinity of the newly synthesized P3HT:PCBM was characterized using an X-ray diffractometer (XRD, Philips XPert) with λ = 1.5404 Å and at 45 kV. Magnetic

characterization was performed using a Quantum Design MPMS in DC mode at room temperature and in dark conditions. Magnetoresistivity was measured under different level of magnetic field (applied using GMW 3470) while applying a voltage between 2 brass needle probes and reporting the current (Keithley 6514) through the sample. All magnetoresistance measurements were done while the samples were illuminated using a halogen light source (3250K).

5.5 Acknowledgements

Chapter 5, in part, is currently being prepared for submission for publication of the material. Huynh, Nha Uyen; Youssef, George. The dissertation author was the primary investigator and author of this material.

Chapter 6 Effect of substrate on the performance of P3HT:PCBM organic framework

Scott Newacheck and George Youssef

6.1 Abstract

Millimeter-scale rhombohedral PCBM crystals were fabricated on multiple types of substrates, from metal, glass, and polymer. The multi-substrate fabrications granted the ability of characterizing the crystals for their full range property map. Moreover, the colossal crystals were fabricated with or without P3HT which permitted different capabilities of the crystals for certain applications. The lone PCBM crystals were characterized for their optical and mechanical properties, whereas the P3HT coated crystals has notable magnetic and conductive performance. These PCBM crystals combined with P3HT hold a promising future for organic photovoltaics and magnetic systems.

6.2 Introduction

Wearable and flexible electronics pose several scientific and technological challenges, requiring a paradigm shift in material science and engineering. On the one hand, the material candidates must exhibit high efficacy for the bidirectional conversion of magnetic and electrical energies, pointing towards oxide-based crystalline materials. On the other hand, the available materials possess poor mechanical flexibility and short fatigue life. Multiple research directions sprang into action to explore the technological potential of metal-perovskite thin films to address this challenge [1], traditional extrinsic and intrinsic multiferroics [2], and metal-organic frameworks [3]. Recently, blends of conjugated polymers with molecular acceptors have attracted much attention in photovoltaic applications, while some have shown a potential magnetoelectric

response. Examples of these conjugated polymers include P3HT, MEH-PPV, MDMO-PPV, while molecular acceptors include PCBM, C_{60}, and $PC_{70}BM$ [4]–[6].

Poly 3-hexylthiophene-2,5-diyl (P3HT) blended with Phenyl-C61-butyric acid methyl ester (PCBM) is a rigorously researched material system for organic photovoltaic (OPV) technologies, achieving nearly 5% efficiency in some cases [7], [8]. The fascinating capability of this organic composite system delves much deeper by landing potential use in organic magnetoresistance (OMAR) and organic ferromagnetic technologies [9]–[11]. The coexistence of the P3HT and PCBM in semiconductive polymer frameworks gives rise to charge-transfer excitonics, theorized to be the source of their magnetic and magnetoresistive properties. The culmination of the electrical, mechanical, and magnetic properties in exitonic polymers situate them as a material candidate for wearable and flexible electronics. For example, P3HT:PCBM thin films exhibit 16% magnetoresistivity at a 0.3 T magnetic field, which is helpful for organic magnetic field sensors [12]. Moreover, the same polymer framework reported a magnetic saturation of 0.65 emu/g at 0.1 T when light is applied, which can be good for organic optomagnetic applications [13].

Most OPV, OMAR, and organic magnets have been fabricated on smooth rigid substrates, such as glass or silicon wafers, for their planarity and ease of handling [6]. Both glass and silicon are resilient to nearly all organic solvents used to fabricate these conjugated polymers, and the substrates can endure the stresses from thermal treatments. Moreover, these inorganic substrates are more conducive for depositing conductive layers such as ITO, necessary for OPV and vertical OMAR devices. However, some research groups have successfully fabricated P3HT:PCBM OPV on polyethylene with similar efficiencies to devices fabricated on glass, demonstrating the potential of soft substrates [14]. Utilizing soft polymeric substrates enables the use of these

conjugated polymers in flexible and wearable electronic applications, which is one of the key benefits of organic-based technology compared to their inorganic counterparts.

This research investigates the effect of the substrate on the mechanical, electrical, and magnetic performance of P3HT:PCBM composite by growing colossal crystals on glass, glass-coated ITO, and PVDF membrane filters. Our group recently demonstrated the process of growing PCBM with sizes exceeding 1 mm, representing more than a 600% increase over the state-of-the-art reported in [15]. The exceptional crystal growth was attributed to the low surface area-to-volume ratio, causing the external layer to solidify and entrapping solvent and slowing down the curing time of the interior. Henceforth, the PCBM crystals are referred to as 'colossal' for the rest of this chapter. The selection of substrate has been shown to affect the film growth characteristics [16], [17]. When P3HT:PCBM is investigated for photovoltaic application, ITO-coated glass is of primary interest as a substrate for its transparency and good electrical conductance. Alternatively, standalone PVDF is suitable for ferroelectric and piezoelectric electronic applications and has excellent mechanical and chemical resilience to withstand the fabrication process of P3HT:PCBM and loading conditions during normal deployment conditions. In the context of this research, PVDF facilitated the dynamic mechanical characterization of P3HT:PCBM, for the first time since other substrates either dominate the response or are not conducive for lifting off the films.

6.3 Materials and Methods

Regioregular poly (3-hexylthiophene) (Rieke Metals) was dissolved entirely in ortho-dichlorobenzene (ODCB) with a concentration of 35 mg/mL. Phenyl-61-butyric acid methyl ester (Nano-C) was then added to the solution in a 1:1 weight ratio concerning P3HT and stirred at 40°C for 15 hours. The solution was drop cast onto a PVDF membrane (Durapore DVPP02500)

previously ultrasound cleaned with deionized water or glass and ITO-coated glass cleaned with isopropyl alcohol. Samples were then left in a controlled environment to cure for enhanced crystallinity. All fabrication steps were performed in an inert N2 environment, while all analyses were done in ambient conditions.

The samples were evaluated magnetically, electrically, and mechanically to fulfill their property maps. Magnetic characterization was measured using a Quantum Design MPMS in DC mode while the samples were without illumination. The microscale electrical characterization was achieved through an AFM workshop TT1 with Pl/Cr coated tips while the macroscale electrical characterization was accomplished with a Terahertz Time-Domain setup with details explained in [18]. Finally, the mechanical characterization was performed on a TA instruments Q800 DMA in film tension mode.

6.4 Results and Discussion

Figure 6-1 encompasses the multiscale microscopy investigation of P3HT:PCBM crystals grown on different substrates, including bare glass, ITO glass, and PVDF membrane. Regardless of the substrate type, the images in the figure demonstrate the ubiquity and unusually large (‘colossal’) crystal size, where the crystal sizes range from 50 um to 1300 um. Several researchers reported the nucleation of these types of crystals when preparing P3HT:PCBM on silicon or ITO glass; however, the crystal size usually appeared to be on the order of the film thickness of approximately 10-80 um. On the contrary, the colossal crystals shown in the figure appear to grow out of the film, attributed to the long curing cycle based on controlling the volume to surface area ratio, as discussed in the methods section.

Figure 6-1a shows an SEM micrograph of a collection of P3HT:PCBM crystals fabricated on glass, whereas Figure 6-1b shows a single crystal with exemplary uniformity and symmetry.

On the one hand, when fabricated on solid and rigid substrates, such as glass, ITO, or silicon, the crystals formed underneath a capping polymer layer of P3HT. A few smaller crystals barely protruding the top capping layer is observed in Figure 6-1a. The top capping layer was gently peeled off to try to uncover the crystals underneath, revealed many crystals with an appearance similar to Figure 6-1c. The rough surface of the exposed crystal is likely due to a strong bond with the P3HT capping layer, damaging the crystal when it was removed. The strong bond between layers is beneficial for its conductivity and photovoltaic efficiency. On the other hand, fabricating these crystals on the PVDF membrane exposed the PCBM formations to the top surface, observed in the optical microscope photographs in Figure 6-1d and 6-1e. It is worth noting that the PVDF membrane acted as a sieve, separating the PCBM colossal crystals on the top from the P3HT crystals on the bottom. In some instances, several PCBM crystals were found lingering at the bottom of the PVDF membrane. This approach can potentially be used to grown large PCBM crystals separated from P3HT crystals for micro- and nano-scale characterization. The partition of the P3HT and PCBM components revealed the crystal's black color owed to the fullerene derivative and smooth reflective surfaces. Moreover, rigids concentric to the outside perimeter are observed in on the crystals due to their layer-by-layer formation.

The exposed PCBM crystals on PVDF were coated with platinum for scanning electron microscopy (Shown in Figures 6-1d-f), which covered the feature ridges causing a similar appearance to the P3HT coated crystals in Figure 6-1a and 6-1b. Unique to the PVDF membrane substrate is the multi-directionality of the crystal growth, where Figure 6-1e shows a SEM micrograph of two crystals growing out of the plane of the film and another interlaced with the others. The bottom panel in Figure 6-1 shows several elemental composition maps extracted from and surrounding a single PCBM crystal, where the first subpanel is an SEM micrograph of the

isolated crystal while the subsequent subpanels, showing the chlorine, sulfur, and fluorine concentration maps. The EDS analysis elucidates a large concentration of chlorine in the PCBM crystal, while fluorine and sulfur were only present in the surrounding PVDF membrane. The elemental composition confirms our previous report that the PCBM crystals include residual dichlorobenzene solvent with a trace amount of P3HT. Fluorine or sulfur were not detected beneath the crystal due to the relatively shallow penetration depth of EDS (~1 μm) compared to the thickness of the crystal.

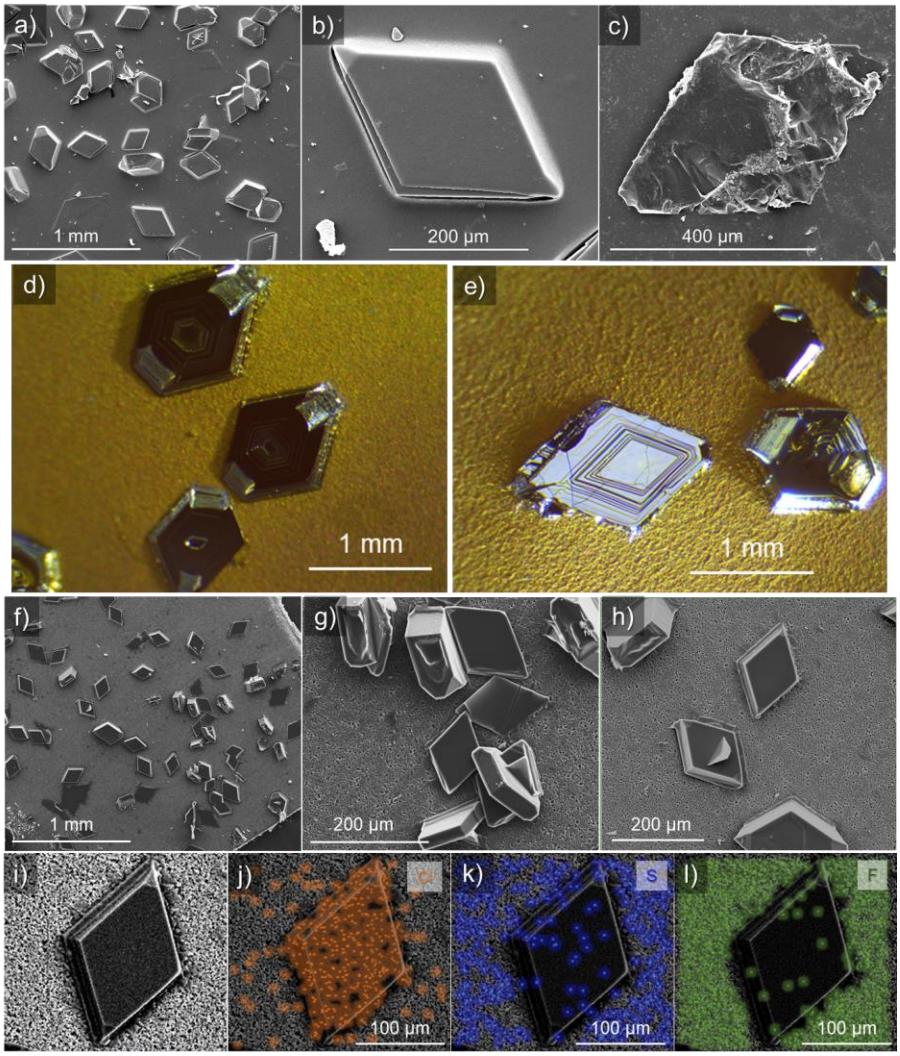

Figure 6-1: (a,b) SEM micrographs of P3HT:PCBM fabricated on glass substrates, where (c) shows a PCBM crystal after the P3HT layer was lifted. (d-e) A collection of microscope images of the P3HT:PCBM fabricated on the PVDF membrane filter, elucidating their geometrical structure. (f-h) SEM micrographs of the organic crystals demonstrating potential geometry formations. (i-l) SEM micrograph of a crystal fabricated on PVDF with superimposed EDS maps for chlorine, sulfur, and fluorine, elucidating the chemical composition of the crystal.

6.4.1 Magnetic properties

The magnetic response of P3HT:PCBM as a donor-acceptor organic framework hinges on the charge transfer between these two components. Thus, the absence or separation of the constituents compromises the magnetic behavior of these polymers. Figure 6-2 provides the

evidence for the dependence of the magnetic response on the cohabitation of the donor and acceptor macromolecules, where the film cast on glass substrate ensured the coexistence of the P3HT and PCBM, resulting in a ferromagnetic response. The P3HT:PCBM crystals on glass yielded a magnetic saturation of 8.2 emu/cm^3, which is in good agreement with the previously reported 10 emu/cm^3 magnetic saturation of the same organic framework when deposited on ITO substrate. On the other hand, the film fabricated on the PVDF membrane shows a diamagnetic response since the membrane successfully segregated the two phases observed in Figure 6-1. Typically, some magnetic behavior is observed for P3HT and PCBM as separate phases; however, the large volume fraction of diamagnetic PVDF overpowers the response. That is to say, the coexistence of P3HT and PCBM is necessary for magnetic functionality.

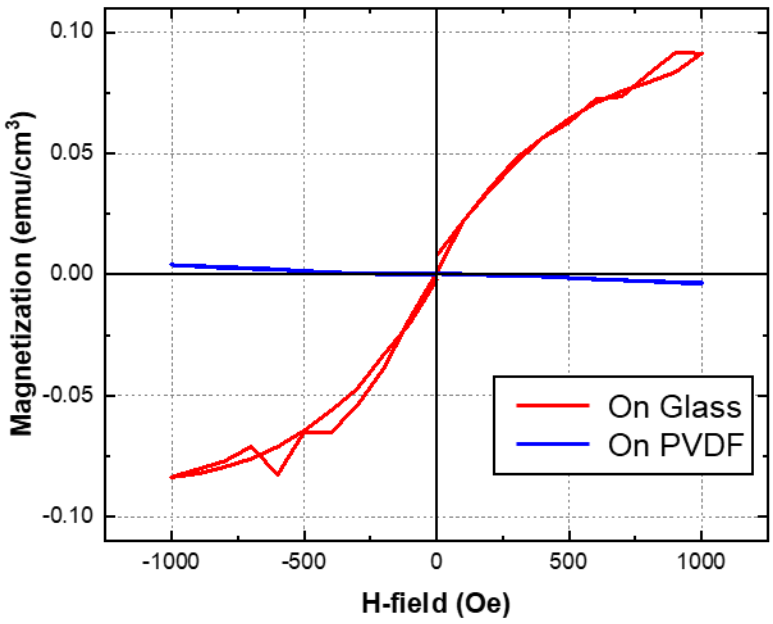

Figure 6-2: Magnetic hysteresis plots of P3HT:PCBM deposited on glass substrate and PVDF membrane, showing ferromagnetic response for the former and diamagnetic response for the latter.

6.4.2 Electrical Properties

The requirements for a material candidate to meet the demand for wearable electronics include electrical conductivity. Probing the electrical properties of the P3HT:PCBM was divided into two sections, depending on the substrate type. First, the crystals fabricated on ITO-coated glass was probed for microscale I-V measurements, utilizing the substrate as a ground plate. Second, the samples fabricated on PVDF and glass were suitable for terahertz time-domain (THz-TD) spectroscopy in transmission mode due to the transparency of the substrates, which measured the complex electric properties in bulk.

Microscale electrical characterization of the P3HT:PCBM crystals fabricated on ITO-coated glass was carried out using conductive atomic force microscopy (C-AFM), where conductivity maps and localized I-V curves were collected from different locations on the samples. Three I-V curves were measured near, on the edge, and on the center of a PCBM crystal, coated with P3HT, and are plotted in Figure 6-3a. The results in the figure elucidate the underlying location-dependent electrical behavior. It should be noted that additional current measurements were collected far away from the crystals but resulted in negligible values, hence not reported here for brevity. The near-crystal I-V curve exhibited a semi-symmetrical, resister-like behavior with a resistance of 7.9 GΩ. The resistance reported herein is significantly lower than prior C-AFM measurements on non-crystalline P3HT:PCBM, especially when considering the difference in thicknesses (12.5 GΩ and 50 nm thick) [19]. On the other hand, the remaining I-V curves on the crystal reported a diode-like characteristic with similar negative resistances of 6.5 GΩ and 6.4 GΩ (at -5V). Uniquely, the I-V measured near the edge of the crystal showed a dramatic forward breakdown voltage (V_z) at 3.38V while the I-V curve measured near the center of the crystal did not exhibit a breakdown voltage within the 5V testing envelope (in other words, there may be a

breakdown above 5V). The perceived delay in breakdown voltage may be due to the increased sample thickness near the center of the crystal since electrical breakdown is exponentially proportional to the applied electric field.

Conductive maps were measured near and on the crystal and are displayed in Figure 6-3b-c and Figure 6-3d-e, respectively. The conductive phase maps both near and on the crystal shows a ridge pattern, which closely mimics the patterns observed on the crystals in the optical photographs of Figure 6-1. The connection of the conductivity and optical patterns suggests that the edges of the crystal ridges play a major role in the conductivity, might be due to a better interconnectedness between the material phases. This claim is substantiated by the ridges that are faintly imprinted in the topography in the near-crystal scan of Figure 6-3b. These topological ridges in Figure 6-3b are likely due to a thinner P3HT layer capping the crystal, allowing the ridges of the crystal to slightly protrude the surface. Notably, the ridge pattern on the crystal (Figure 6-3e) was thicker, clearer, and less frequent than the ridge pattern near the crystal (Figure 6-3c). The ridge pattern dichotomy is also observed in the optical photographs in Figure 6-1 when comparing the periodicity of the ridges on the center of the crystals and around the edges.

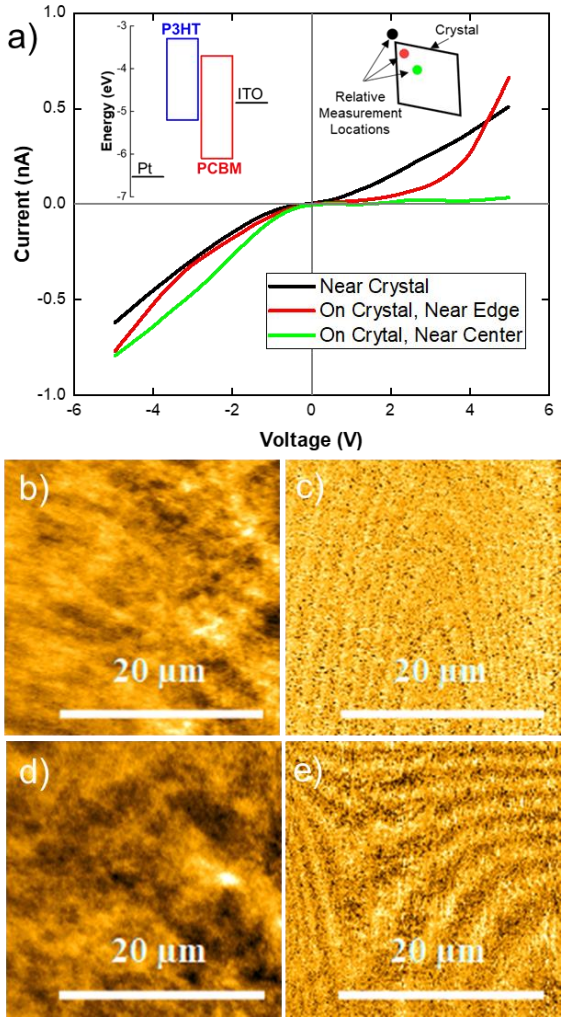

Figure 6-3: (a) I-V curves of P3HT:PCBM crystal on ITO glass using conductive AFM with a Cr/Pt tip. Top left inset shows the bandgap energies of P3HT, PCBM, and work functions of ITO and Pt from values reported in literature. Top right inset shows a schematic diagram of the relative locations of the measurement with respect to a P3HT:PCBM crystal. (b-c) Topography and conductive phase maps of near the crystal and (d-e) on the crystal.

The THz-TD measurements of the samples fabricated on glass and PVDF are plotted in Figure 6-4 with a reference of a plain glass substrate. For consistency of the reference signal, the P3HT:PCBM-PVDF sample was also measured with a glass substrate. The P3HT:PCBM samples delayed and attenuated the peak amplitude of the THz wave due to their relative refractive index

and their absorption of light. The time delay and amplitude of the peak are related to the complex refractive index ($\tilde{n} = n + i\kappa$) by

$$n = 1 + \frac{ct_s}{d}, \text{ and } \quad \kappa = \frac{c \ln\left(1 - {}^{A-A_0}/_{A_0}\right)}{4\pi d f} \tag{6-1}$$

where A_o, A, and t_s are the amplitudes of the reference signal and sample signal, and the time difference between the two, respectively. The sample thickness is defined as d while f and c are the frequency and speed of light in vacuum. From the complex refractive index, the relative permittivity can be obtained by $\varepsilon_r = \tilde{n}^2$, assuming the relative permeability is close to unity based on the low magnetic response in Figure 6-2. The refractive index values and complex permittivity, averaged over three THz-TD measurements, are listed in Table 6-1. The real refractive index of the P3HT:PCBM fabricated on glass closely matches reported values in literature [20], [21], suggesting that the PCBM crystals does not have a notable effect on the photonic behavior compared to amorphous films in this frequency range. The reduction in the refractive index for the P3HT:PCBM-PVDF sample is attributed to the inclusion of the PVDF substrate, where the refractive index for PVDF was previously reported to range from 1.4-2.1 in the THz region [22].

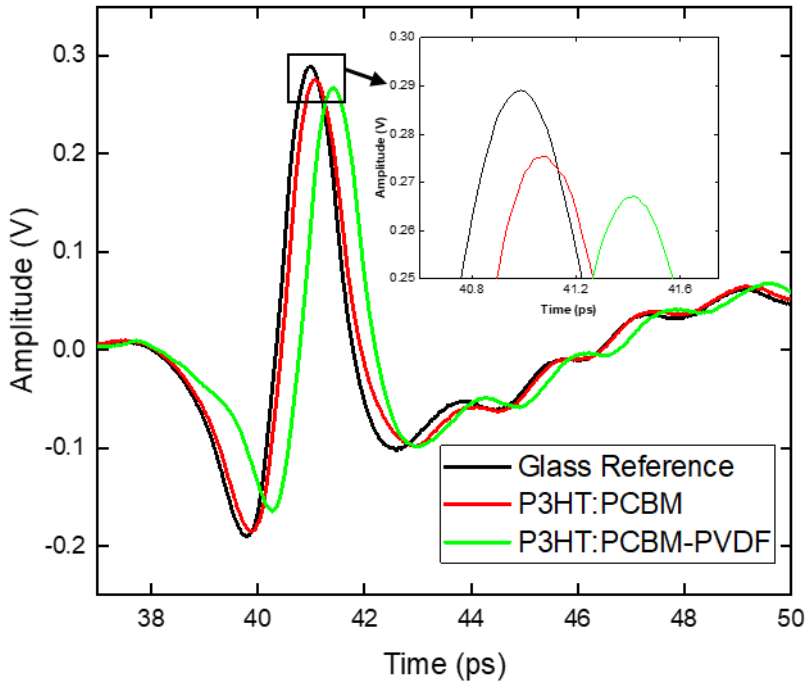

Figure 6-4: Terahertz time-domain spectroscopy of glass reference, P3HT:PCBM fabricated on glass, and P3HT:PCBM-PVDF samples.

Table 6-1: Optical and dielectric properties of P3HT:PCBM on glass and PVDF

Sample	n	κ	ε_r
P3HT:PCBM	3.30	2.6e-3	10.82+1.73i
P3HT:PCBM-PVDF	1.42	4.7e-4	2.00+0.15i

6.4.3 Mechanical Properties

As mentioned in the introduction, the commonly used traditional substrates, i.e., ITO-glass and bare glass, are not conducive for flexible, wearable, and biomedical electronics. Moreover, macroscale mechanical characterization of P3HT:PCBM is experimentally challenging (within the

limitation of the equipment available to the research team) on these traditional substrates due to their overwhelming rigidity compared to the local modulus of P3HT:PCBM reported to be 550-600 MPa [23]. Thus, the mechanical properties of P3HT:PCBM-PVDF samples were characterized using a dynamic mechanical analyzer (TA Q800) in uniaxial tension. Three P3HT:PCBM-PVDF samples were compared to pristine PVDF membranes. The averaged stress-strain curves are plotted in Figure 6-5. Notably, P3HT:PCBM decreased the strain-to-yield of the PVDF membrane by 65±0.3%, which may be due to chemical degradation from the dichlorobenzene during processing. Nevertheless, the significant 24% strain-to-yield of P3HT:PCBM-PVDF is still suitable for flexible, wearable, and biomedical electronic systems.

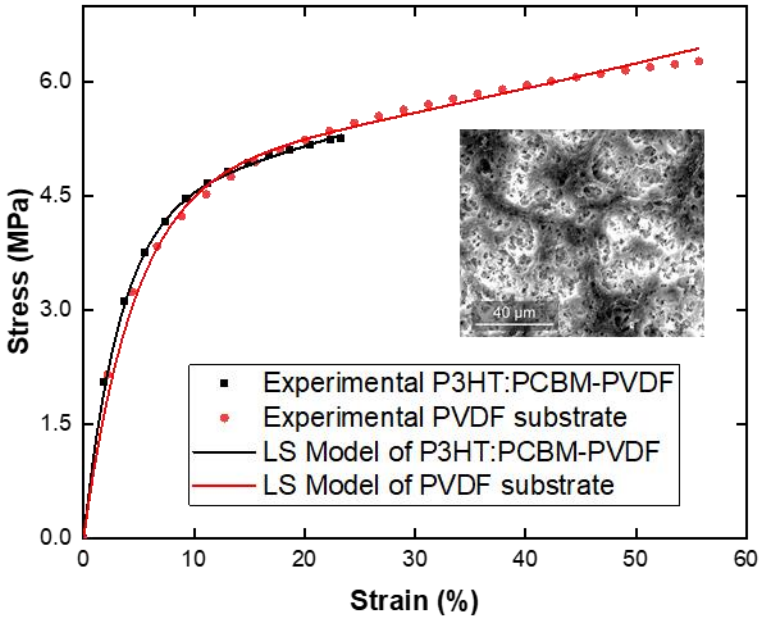

Figure 6-5: Engineering Stress-Strain relationship of P3HT:PCBM-PVDF and plain PVDF substrate with their respective fitted Liu-Subhash model responses. Inset showing an SEM micrograph of the porous structure of the PVDF substrate

The overall behavior of the PVDF and P3HT:PCBM-PVDF samples bared little resemblance to any hyperelastic model for bulk polymers but did closely mimic the response of polymeric foam. This is attributed to the pores structure of the PVDF membrane used here as the substrate (SEM micrograph of the PVDF membrane surface is included in the inset of Figure 6-5). Liu and Subhash proposed a phenomenological model (referred to as the LS model herein) to describe the stress-strain relationship of polymeric foam under uniaxial tension, given as

$$\sigma = A\frac{e^{\alpha\varepsilon}-1}{B+e^{\beta\varepsilon}} \tag{6-2}$$

where, σ and ε are the engineering stress and strain, respectively, A, B, α, and β are curve fitting parameters. A has the units of stress and the others are unitless. Walter *et al.* went on to further explain that A is related to the stress of pore collapse and the ratio of the α and β parameters are related to material stiffening (if $\alpha/\beta > 1$) or softening (if $\alpha/\beta < 1$). The elastic modulus (E) can be obtained by differentiating Equation 6-2, as the strain approaches zero, given as

$$E = \frac{A\alpha}{1+B}. \tag{6-3}$$

The results of the fitted LS model to the experimental stress-strain plots in Figure 6-5 are presented in Table 6-2. From the reported averaged parameters, the stress-strain relationships were reconstructed for the PVDF membrane and the P3HT:PCBM-PVDF composite and are replotted in Figure 6-5, demonstrating their excellent agreement. Overall, the LS model pronounces some notable effects of P3HT:PCBM, such as a 30% increase in the stiffness and an 8% decrease of the stress of pore collapse of the PVDF substrate. The 30% increase of stiffness is attributed to the higher rigidity of the PCBM crystals. Prior microscale characterization reported that the PCBM crystals had a plane-stress stiffness of ~550 MPa, which is lending its relatively high stiffness to the P3HT:PCBM-PVDF bulk. Thermogravimetric analysis revealed that P3HT:PCBM constituted

~9% of the weight of the tested P3HT:PCBM-PVDF samples. Moreover, image processing analysis showed that the PCBM crystals had a ~8% coverage of the sample surface. Using the in-plane force-balance relationship of laminate composites ($E_c a_c = E_1 a_1 + E_2 a_2$, where a is the cross-sectional area, and subscripts c, 1, and 2, represent the composite and the two materials, respectively), the Young's modulus parameters in Table 6-2, and the cross-sectional area where their details are given in the appendix, the calculated stiffness of P3HT:PCBM is ~580 MPa, which is in great agreement to the prior microscale characterization study. Finally, the 8% decrease in pore collapse stress is attributed to P3HT:PCBM filling in the pore volume of PVDF.

Table 6-2: Liu-Subhash model parameters for PVDF substrate and P3HT:PCBM-PVDF

Sample	A (MPa)	α	β	E (MPa)
P3HT:PCBM-PVDF	4.391 ±0.014	0.306±0.011	0.298±0.011	1.344±0.044
PVDF substrate	4.768 ±0.028	0.223±0.004	0.217±0.004	1.058±0.012

6.5 Conclusion

This study followed a prior report on the formation of colossal PCBM crystals when P3HT:PCBM solution is drop casted onto ITO-coated glass and silicon wafers [23]. Herein, the synthesis of these crystals was repeated on glass and on PVDF polymer membranes. It is worth noting that polymer substrates are detrimental to other reported crystal growth processes, but was unaffected herein [15]. When fabricating on glass, the PCBM crystals were found to form on the glass while a layer of P3HT covered the crystals. The crystals had a good adhesion to the glass and P3HT, causing their mechanical failure when the P3HT layer was separated. Conversely, when fabricating on PVDF, the P3HT passed the substrate to leave the crystals uncoated on the top surface. The uncoated crystals revealed numerous features which was occluded by P3HT in prior

samples. However, the separation of the component phases was found to be detrimental to the magnetic and conductive properties. When the phases were in contact (i.e., fabricated on glass), the colossal crystals outperformed magnetic and conductive measurements of their amorphous counterparts reported in literature [24]. Finally, their mechanical properties were also characterized and were found to be in good agreement to prior micromechanical measurements.

6.6 Acknowledgements

Chapter 6, in part, is currently being prepared for submission for publication of the material. Youssef, George. The dissertation author was the primary author of this chapter.

Future Work

Engineering components for flexible, soft, organic, biocompatible, and wearable electronics is a worthy goal that still demands research and development. An aspect that is severely lacking within this industrial domain, but is normally easy for rigid and inorganic systems, is magnetoelectricity. The solution to this was to fabricate strain-mediated magnetoelectric composites by embedding inorganic magnetic particles into a piezoelectric polymeric matrix, which has been investigated over the last decade thoroughly by the research community. Although soft magnetoelectric composites have been demonstrated (herein and by others), the efficiency needs to be improved for practical use. This dissertation elucidated a few challenges with the current dogma of organo-magnetoelectric material systems, namely, electrical leakage, electrical breakdown, and the instability of the embedded particle confinement. All these noted issues are caused by the inorganic magnetic particles; thus, future research should look to address these problems either by investigating a way to lock the motion (i.e., particle migration) and electrical current passing through (electrical breakdown) the inorganic particles. Alternatively, the inorganic particles can substituted completely. Potential possibilities for the former could be to encapsulate the particles with a coating system with high dielectric permittivity and the ability to chemically bond with the polymer matrix to divert current leakage and lock their location while improving strain transfer, respectively. The second approach, of completely substituting the inorganic particles, was investigated in this project through the implementation of organic magnetic materials. However, research in organic magnetic materials is still in its infancy stage, only offering a handful of options that can operate at room-temperature. More importantly, the ferromagnetic coupling of these organic magnetic materials is still orders of magnitude lower than

their inorganic counterparts. Additional future research is needed to improve organic ferromagnetic coupling before they can be used in industry.

The last part of the dissertation looked to improve the crystallinity of organic materials to enhance their ferromagnetic ordering, as it has been suggested multiple times in literature [95], [97]. The fabrication process utilized was capable of fabricating the largest organic crystals of the reported material system; however, only moderate improvements in magnetism was observed. Nonetheless, the colossal crystals improved the conductivity, which may be beneficial for photovoltaic research. Future research emphasize the potential of the reported colossal crystals for flexible and wearable electronic applications with a focus of the electrical and magnetic utilities [122].

References

[1] R. F. Gibson, “A review of recent research on mechanics of multifunctional composite materials and structures,” *Compos. Struct.*, vol. 92, no. 12, pp. 2793–2810, 2010, doi: 10.1016/j.compstruct.2010.05.003.

[2] K. Friedrich and U. Breuer, *Multifunctionality of Polymer Composites Challenges and New Solutions*. Waltham, MA, 2015.

[3] A. Perez-Rosado, S. K. Gupta, and H. A. Bruck, “Mechanics of multifunctional wings with solar cells for robotic birds,” in *Conference Proceedings of the Society for Experimental Mechanics Series*, 2016, vol. 7, pp. 1–10, doi: 10.1007/978-3-319-21762-8_1.

[4] S. Dong, J. Liu, S. Cheong, and Z. Ren, “Multiferroic Materials and Magnetoelectric Physics: Symmetry, Entanglement, Excitation, and Topology,” *Adv. Phys.*, vol. 64, no. 519–626, pp. 1–120, 2015.

[5] H. Palneedi, V. Annapureddy, S. Priya, and J. Ryu, “Status and Perspectives of Multiferroic Magnetoelectric Composite Materials and Applications,” *Actuators*, vol. 5, no. 1, p. 9, 2016, doi: 10.3390/act5010009.

[6] Y. Yuan *et al.*, “Efficiency enhancement in organic solar cells with ferroelectric polymers,” *Nat. Mater.*, vol. 10, no. 4, pp. 296–302, Feb. 2011, doi: 10.1038/nmat2951.

[7] G. Srinivasan, “Introduction to Magnetoelectric Coupling and Multiferroic Films,” *J. Phys. D. Appl. Phys.*, vol. 44, no. 243001, 2011, doi: 10.1088/0022-3727/44/24/243001.

[8] Y. Wang, J. Hu, Y. Lin, and C.-W. W. Nan, “Multiferroic magnetoelectric composite nanostructures,” *NPG Asia Mater.*, vol. 2, no. 2, pp. 61–68, 2010, doi: 10.1038/asiamat.2010.32.

[9] X. Liang *et al.*, “A Review of Thin-Film Magnetoelastic Materials for Magnetoelectric Applications,” *Sensors*, vol. 20, no. 5, p. 1532, Mar. 2020, doi: 10.3390/s20051532.

[10] G. Catalan and J. F. Scott, “Physics and applications of bismuth ferrite,” *Adv. Mater.*, vol. 21, no. 24, pp. 2463–2485, 2009, doi: 10.1002/adma.200802849.

[11] Z. Yao, Y. E. Wang, S. Keller, and G. P. Carman, “Bulk Acoustic Wave-Mediated Multiferroic Antennas : Architecture and Performance Bound,” *IEEE Trans. Antennas Propag.*, vol. 63, no. 8, pp. 3335–3344, 2015.

[12] S. Newacheck and G. Youssef, “Wireless energy transfer based on strain-mediated composite multiferroics,” *Smart Mater. Struct.*, vol. 29, no. 1, p. 015014, 2019, doi: 10.1088/1361-665X/ab545b.

[13] L. W. Martin and R. Ramesh, “Multiferroic and magnetoelectric heterostructures,” *Acta Mater.*, vol. 60, no. 6–7, pp. 2449–2470, Apr. 2012, doi: 10.1016/j.actamat.2011.12.024.

[14] R. Ramesh and N. A. Spaldin, “Multiferroics: progress and prospects in thin films,” *Nat. Mater.*, vol. 6, no. 1, pp. 21–29, 2007, doi: 10.1038/nmat1805.

[15] S. Dong, J. Zhai, J.-F. Li, and D. Viehland, “Magnetoelectric effect in Terfenol-D⁄Pb(Zr,TiO)[sub 3]⁄μ-metal laminate composites,” *Appl. Phys. Lett.*, vol. 89, no. 12, p. 122903, 2006, doi: 10.1063/1.2355459.

[16] K. Mori and M. Wuttig, “Magnetoelectric coupling in Terfenol-D/polyvinylidenedifluoride composites,” *Appl. Phys. Lett.*, vol. 81, no. 1, pp. 100–101, Jul. 2002, doi: 10.1063/1.1491006.

[17] T. Wu, M. Emmons, T.-K. Chung, J. Sorge, and G. P. Carman, “Influence of mechanical load bias on converse magnetoelectric laminate composites,” *J. Appl. Phys.*, vol. 107, no. 9, p. 09D912, 2010, doi: 10.1063/1.3362919.

[18] J. Ryu, S. Priya, K. Uchino, and H. E. Kim, “Magnetoelectric effect in composites of magnetostrictive and piezoelectric materials,” *J. Electroceramics*, vol. 8, no. 2, pp. 107–119, 2002, doi: 10.1023/A:1020599728432.

[19] C. W. Nan, G. Liu, and Y. Lin, “Influence of interfacial bonding on giant magnetoelectric response of multiferroic laminated composites of Tb1-xDyxFe2 and PbZrxTi1-xO3,” *Appl. Phys. Lett.*, vol. 83, no. 21, pp. 4366–4368, 2003, doi: 10.1063/1.1630157.

[20] S. Dong, J. F. Li, and D. Viehland, “Magnetoelectric coupling, efficiency, and voltage gain effect in piezoelectric-piezomagnetic laminate composites,” *Front. Ferroelectr. A Spec. Issue J. Mater. Sci.*, vol. 41, pp. 97–106, 2007, doi: 10.1007/978-0-387-38039-1_9.

[21] M. Vopsaroiu, M. G. Cain, G. Sreenivasulu, G. Srinivasan, and A. M. Balbashov, “Multiferroic composite for combined detection of static and alternating magnetic fields,” *Mater. Lett.*, vol. 66, no. 1, pp. 282–284, 2012, doi: 10.1016/j.matlet.2011.08.094.

[22] Z. Zuo *et al.*, “In-plane anisotropic converse magnetoelectric coupling effect in FeGa/polyvinylidene fluoride heterostructure films,” *J. Appl. Phys.*, vol. 113, no. 17, 2013, doi: 10.1063/1.4793780.

[23] R. C. O’Handley, J. K. Huang, D. C. Bono, and J. Simon, “Improved Wireless, Transcutaneous Power Transmission for In VivoApplications,” *IEEE Sens. J.*, vol. 8, no. 1, pp. 57–62, 2008, doi: 10.1109/JSEN.2007.912899.

[24] D. Viehland and S. Dong, “Longitudinal and transverse magnetoelectric voltage coe ffcients of magnetostrictive/ piezoelectric laminate composite: experiments,” *IEEE Trans. Ultrason. Ferroelectr. Freq. Control*, vol. 50, no. 10, pp. 1253–1261, 2003, doi: 10.1109/TUFFC.2004.1320738.

[25] T. Wu, C. M. Chang, T. K. Chung, and G. Carman, “Comparison of Effective Direct and Converse Magnetoelectric Effects in Laminate Composites,” *IEEE Trans. Magn.*, vol. 45, no. 10, pp. 4333–4336, 2009, doi: 10.1109/TMAG.2009.2024546.

[26] S. Dong, J. F. Li, and D. Viehland, “Ultrahigh magnetic field sensitivity in laminates of TERFENOL-D and Pb(Mg1/3Nb2/3)O3-PbTiO3 crystals,” *Appl. Phys. Lett.*, vol. 83, no. 11, pp. 2265–2267, 2003, doi: 10.1063/1.1611276.

[27] S. Dong, J. Zhai, J. Li, and D. Viehland, “Near-ideal magnetoelectricity in high-permeability magnetostrictive/ piezofiber laminates with a (2-1) connectivity,” *Appl. Phys. Lett.*, vol. 89, no. 25, pp. 1–4, 2006, doi: 10.1063/1.2420772.

[28] F. Ramirez, P. R. Heyliger, and E. Pan, “Free vibration response of two-dimensional magneto-electro-elastic laminated plates,” *J. Sound Vib.*, vol. 292, pp. 626–644, 2006, doi: 10.1016/j.jsv.2005.08.004.

[29] C. P. Zhao, F. Fang, and W. Yang, “A dual-peak phenomenon of magnetoelectric coupling in laminated Terfenol-D/PZT/Terfenol-D composites,” *Smart Mater. Struct.*, vol. 19, no. 125004, p. 125004, 2010, doi: 10.1088/0964-1726/19/12/125004.

[30] F. Ramirez, P. R. Heyliger, and E. Pan, “Free vibration response of two-dimensional magneto-electro-elastic laminated plates,” *J. Sound Vib.*, vol. 292, pp. 626–644, 2006, doi: 10.1016/j.jsv.2005.08.004.

[31] G. Feuillard and F. Levassort, “New tools for electromechanical characterisation of piezoceramics,” *J. Electroceramics*, vol. 19, pp. 419–426, 2007, doi: 10.1007/s10832-007-9177-4.

[32] D. Filippov and V. Petrov, “Resonance Magneto-Electric Effects in Layered Magnetostrictive-Piezoelectric Composites,” *Phys. Rev. B*, no. January 2016, 2003, doi: 10.1103/PhysRevB.68.132408.

[33] T. I. Muchenik and E. J. Barbero, “Micromechanics Modeling of Magnetoelectric Composites,” 2014.

[34] PerkinElmer, “Dynamic Mechanical Analysis Basics: Part 2 Thermoplastic Transitions and Properties.” Accessed: Mar. 10, 2020. [Online]. Available: www.perkinelmer.com.

[35] J. Zhai *et al.*, “Giant magnetoelectric effect in Metglas/polyvinylidene-fluoride laminates,” *Appl. Phys. Lett.*, vol. 89, no. 8, p. 083507, Aug. 2006, doi: 10.1063/1.2337996.

[36] M. Staruch, J. F. Li, Y. Wang, D. Viehland, and P. Finkel, “Giant magnetoelectric effect in nonlinear Metglas/PIN-PMN-PT multiferroic heterostructure,” *Appl. Phys. Lett.*, vol. 105, no. 15, 2014, doi: 10.1063/1.4898039.

[37] Y. Jia, S. W. Or, H. L. W. Chan, X. Zhao, and H. Luo, “Converse magnetoelectric effect in laminated composites of PMN–PT single crystal and Terfenol-D alloy,” *Appl. Phys. Lett.*, vol. 88, no. 24, p. 242902, Jun. 2006, doi: 10.1063/1.2212054.

[38] C. P. Zhao, F. Fang, and W. Yang, “A dual-peak phenomenon of magnetoelectric coupling in laminated Terfenol-D/PZT/Terfenol-D composites,” *Smart Mater. Struct.*, vol. 19, no. 12, 2010, doi: 10.1088/0964-1726/19/12/125004.

[39] M. Venkata Ramanaa, N. Ramamanohar Reddy, G. Sreenivasulu, K. V. Siva kumar, B. S. Murty, and V. R. K. Murthy, "Enhanced mangnetoelectric voltage in multiferroic particulate Ni0.83Co0.15Cu0.02Fe1.9O4- δ/PbZr0.52Ti0.48O3 composites - dielectric, piezoelectric and magnetic properties," *Curr. Appl. Phys.*, vol. 9, no. 5, pp. 1134–1139, 2009, doi: 10.1016/j.cap.2009.01.002.

[40] R. Christensen, *Mechanics of Composite Materials*. New York: Dover Publications, 2005.

[41] F. Bauer, E. Fousson, and Q. M. Zhang, "Recent advances in highly electrostrictive P(VDF-TrFE-CFE) terpolymers," *IEEE Trans. Dielectr. Electr. Insul.*, vol. 13, no. 5, pp. 1149–1153, 2006, doi: 10.1109/TDEI.2006.247843.

[42] D. M. Shin, S. W. Hong, and Y. H. Hwang, "Recent advances in organic piezoelectric biomaterials for energy and biomedical applications," *Nanomaterials*, vol. 10, no. 1, 2020, doi: 10.3390/nano10010123.

[43] L. Ruan, X. Yao, Y. Chang, L. Zhou, G. Qin, and X. Zhang, "Properties and applications of the β phase poly(vinylidene fluoride)," *Polymers (Basel).*, vol. 10, no. 3, pp. 1–27, 2018, doi: 10.3390/polym10030228.

[44] C. W. Nan, M. Li, and J. H. Huang, "Calculations of giant magnetoelectric effects in ferroic composites of rare-earth-iron alloys and ferroelectric polymers," *Phys. Rev. B - Condens. Matter Mater. Phys.*, vol. 63, no. 14, pp. 1–9, 2001, doi: 10.1103/PhysRevB.63.144415.

[45] Y. Guo *et al.*, "Giant magnetodielectric effect in 0-3 Ni0.5Zn 0.5Fe2O4-Poly(vinylidene-fluoride) nanocomposite films," *J. Phys. Chem. C*, vol. 114, no. 32, pp. 13861–13866, 2010, doi: 10.1021/jp103777r.

[46] J. X. Zhang *et al.*, "The effect of magnetic nanoparticles on the morphology, ferroelectric, and magnetoelectric behaviors of CFO/P(VDF-TrFE) 0–3 nanocomposites," *J. Appl. Phys.*, vol. 105, no. 5, p. 054102, Mar. 2009, doi: 10.1063/1.3078111.

[47] D. Guyomar, B. Guiffard, R. Belouadah, and L. Petit, "Two-phase magnetoelectric nanopowder/polyurethane composites," *J. Appl. Phys.*, vol. 104, no. 7, 2008, doi: 10.1063/1.2985904.

[48] P. Martins *et al.*, "Linear anhysteretic direct magnetoelectric effect in Ni0.5Zn0.5Fe2O4/poly(vinylidene fluoride-trifluoroethylene) 0-3 nanocomposites," *J. Phys. Chem. C*, vol. 44, no. 48, pp. 0–3, Dec. 2011, doi: 10.1088/0022-3727/44/48/482001.

[49] O. D. Jayakumar, B. P. Mandal, J. Majeed, G. Lawes, R. Naik, and a K. Tyagi, "Inorganic-organic multiferroic hybrid films of Fe3O4 and PVDF with significant magneto-dielectric coupling," *J. Mater. Chem. C*, vol. 1, no. 23, pp. 3710–3715, 2013, doi: 10.1039/c3tc30216d.

[50] P. Anithakumari, B. P. Mandal, E. Abdelhamid, R. Naik, and A. K. Tyagi, "Enhancement of dielectric, ferroelectric and magneto-dielectric properties in PVDF-BaFe12O19 composites: A step towards miniaturizated electronic devices," *RSC Adv.*, vol. 6, no. 19, pp. 16073–16080, 2016, doi: 10.1039/c5ra27023e.

[51] K. P. Mohanchandra, S. V. Prikhodko, K. P. Wetzlar, W. Y. Sun, P. Nordeen, and G. P. Carman, "Sputter deposited Terfenol-D thin films for multiferroic applications," *AIP Adv.*, vol. 5, no. 9, 2015, doi: 10.1063/1.4930602.

[52] J. A. Crayston, J. N. Devine, and J. C. Walton, "Conceptual and Synthetic Strategies for the Preparation of Organic Magnets Contents 1. Introductory Aspects of Magnetism," *Tetrahedron*, vol. 56, no. 541, pp. 7829–7857, 2000,

[53] J. S. Miller and A. J. Epstein, "Organic and Organometallic Molecular Magnetic Materials—Designer Magnets," *Angew. Chemie Int. Ed. English*, vol. 33, no. 4, pp. 385–415, Mar. 1994, doi: 10.1002/anie.199403851.

[54] V. A. Online *et al.*, "Investigation of morphological degradation of P3HT : PCBM bulk heterojunction fi lms exposed to long-term host solvent vapor †," *J. Mater. Chem. A*, vol. 4, pp. 3743–3753, 2016, doi: 10.1039/c5ta09873d.

[55] P. Šiffalovic, J. Müllerová, M. Kaiser, and V. Nádaz, "Optical absorption study of P3HT : PCBM blend photo-oxidation for bulk heterojunction solar cells," *Sol. Energy*, vol. 134, pp. 294–301, 2016, doi: 10.1016/j.solener.2016.05.009.

[56] P. R. Berger and M. Kim, "Polymer solar cells : P3HT : PCBM and beyond," *J. Renew. Sustain. Energy*, vol. 013508, 2018, doi: 10.1063/1.5012992.

[57] M. T. Dang, L. Hirsch, and G. Wantz, “P3HT : PCBM , Best Seller in Polymer Photovoltaic Research,” *Adv. Mater.*, vol. 23, pp. 3597–3602, 2011, doi: 10.1002/adma.201100792.

[58] K. S. Ramadan, D. Sameoto, and S. Evoy, “A review of piezoelectric polymers as functional materials for electromechanical transducers,” *Smart Mater. Struct.*, vol. 23, no. 3, p. 033001, Mar. 2014, doi: 10.1088/0964-1726/23/3/033001.

[59] J. P. Domann, C. Chen, G. P. Carman, and R. N. Candler, “Multiferroic Micro-Motors With Deterministic Single Input Control,” pp. 1–24, 2018.

[60] J.-G. Zhu, Y. Zheng, and G. A. Prinz, “Ultrahigh density vertical magnetoresistive random access memory (invited),” *J. Appl. Phys.*, vol. 87, no. 9, pp. 6668–6673, 2000, doi: 10.1063/1.372805.

[61] K. S. Tan, W. C. Gan, T. S. Velayutham, and W. H. A. Majid, “Pyroelectricity enhancement of PVDF nanocomposite thin films doped with ZnO nanoparticles,” *Smart Mater. Struct.*, vol. 23, no. 12, p. 125006, 2014, doi: 10.1088/0964-1726/23/12/125006.

[62] P. Martins, A. C. Lopes, and S. Lanceros-Mendez, “Electroactive phases of poly(vinylidene fluoride): Determination, processing and applications,” *Prog. Polym. Sci.*, vol. 39, no. 4, pp. 683–706, 2014, doi: 10.1016/j.progpolymsci.2013.07.006.

[63] B. Ploss, “Influence of poling and annealing on the nonlinear dielectric permittivity of PVDF-TRFE copolymers,” *IEEE Trans. Dielectr. Electr. Insul.*, vol. 5, no. 1, pp. 91–95, Feb. 1998, doi: 10.1109/94.660777.

[64] Q. Yang, Z. Shi, D. Ma, Y. He, and J. Wang, “Flexible PbTiO3-nanowires/ P(VDF-TrFE) composite films and their dielectric, ferroelectric and pyroelectric properties,” *Ceram. Int.*, vol. 44, no. 12, pp. 14850–14856, Aug. 2018, doi: 10.1016/J.CERAMINT.2018.05.118.

[65] T. H. L. Nguyen *et al.*, “Magnetoelectric properties of nickel nanowires-P(VDF-TrFE) composites,” *Mater. Chem. Phys.*, vol. 153, pp. 195–201, 2015, doi: 10.1016/j.matchemphys.2015.01.003.

[66] A. Prewitt, “Effects of the poling process on dielectric, piezoelectric, and ferroelectric properties of lead zirconate titanate,” pp. 1–159, 2012, doi: 10.1017/CBO9781107415324.004.

[67] Yiming Liu, Kai Liang Ren, H. F. Hofmann, and Qiming Zhang, “Investigation of electrostrictive polymers for energy harvesting,” *IEEE Trans. Ultrason. Ferroelectr. Freq. Control*, vol. 52, no. 12, pp. 2411–2417, Dec. 2005, doi: 10.1109/TUFFC.2005.1563285.

[68] L. Zheng, W. Li, B. Cui, and G. C. Hadjipanayis, “Tb0.3Dy0.7Fe1.92 nanoflakes prepared by surfactant-assisted high energy ball milling,” *J. Alloys Compd.*, vol. 509, no. 19, pp. 5773–5776, 2011, doi: 10.1016/j.jallcom.2011.02.092.

[69] N. A. Spaldin and R. Ramesh, “Advances in magnetoelectric multiferroics,” *Nat. Mater.*, vol. 18, no. 3, pp. 203–212, 2019, doi: 10.1038/s41563-018-0275-2.

[70] S. Newacheck and G. Youssef, “Magnetoelectricity beyond saturation,” *Mater. Horizons*, 2020, doi: 10.1039/d0mh00595a.

[71] C. W. Nan, M. I. Bichurin, S. Dong, D. Viehland, and G. Srinivasan, “Multiferroic magnetoelectric composites: Historical perspective, status, and future directions,” *J. Appl. Phys.*, vol. 103, no. 3, p. 031101, 2008, doi: 10.1063/1.2836410.

[72] Y. Cheng, B. Peng, Z. Hu, Z. Zhou, and M. Liu, “Recent development and status of magnetoelectric materials and devices,” *Phys. Lett. A*, vol. 382, no. 41, pp. 3018–3025, Oct. 2018, doi: 10.1016/j.physleta.2018.07.014.

[73] X. Zhang *et al.*, “Magnetoelectric soft composites with a self-powered tactile sensing capacity,” *Nano Energy*, vol. 69, p. 104391, 2020, doi: 10.1016/j.nanoen.2019.104391.

[74] L. Zhang, P. Bass, and Z.-Y. Cheng, “Physical aspects of 0-3 dielectric composites,” *J. Adv. Dielectr.*, vol. 05, no. 02, p. 1550012, 2015, doi: 10.1142/s2010135x15500125.

[75] S. Newacheck and G. Youssef, “Synthesis and characterization of polarized novel 0–3 Terfenol-D/PVDF-TrFE composites,” *Compos. Part B Eng.*, vol. 172, no. March, pp. 97–102, 2019, doi: 10.1016/j.compositesb.2019.05.043.

[76] Y. Zong, T. Zheng, P. Martins, S. Lanceros-Mendez, Z. Yue, and M. J. Higgins, “Cellulose-based magnetoelectric composites,” *Nat. Commun.*, vol. 8, no. 1, pp. 1–8, Dec. 2017, doi: 10.1038/s41467-017-00034-4.

[77] C. Y. Liang *et al.*, “Modeling of magnetoelastic nanostructures with a fully coupled mechanical-micromagnetic model,” *Nanotechnology*, vol. 25, no. 43, 2014, doi: 10.1088/0957-4484/25/43/435701.

[78] P. Wang *et al.*, “Colossal Magnetoelectric Effect in Core–Shell Magnetoelectric Nanoparticles,” *Nano Lett.*, 2020, doi: 10.1021/acs.nanolett.0c01588.

[79] G. Youssef, S. Nacy, and S. Newacheck, “Leveraging strain localization to improve the performance of magnetoelectric composite cylinder,” *Eur. Phys. Lett.*, vol. 131, no. 14003, 2020.

[80] R. Brito-Pereira, C. Ribeiro, S. Lanceros-Mendez, and P. Martins, “Magnetoelectric response on Terfenol-D/ P(VDF-TrFE) two-phase composites,” *Compos. Part B Eng.*, vol. 120, pp. 97–102, 2017, doi: 10.1016/j.compositesb.2017.03.055.

[81] G. Youssef, S. Newacheck, and M. Lopez, “Mapping magnetoelastic response of terfenol-D ring structure,” *Appl. Phys. Lett.*, vol. 110, no. 19, p. 192408, 2017, doi: 10.1063/1.4983202.

[82] Z. Zhang, H. Pang, A. Georgiadis, and C. Cecati, “Wireless Power Transfer - An Overview,” *IEEE Trans. Ind. Electron.*, vol. 66, no. 2, pp. 1044–1058, 2019, doi: 10.1109/TIE.2018.2835378.

[83] H. Wei *et al.*, “An overview of lead-free piezoelectric materials and devices,” *J. Mater. Chem. C*, vol. 6, no. 46, pp. 12446–12467, Nov. 2018, doi: 10.1039/C8TC04515A.

[84] G. Engdahl and E. Quandt, *Handbook of Giant Magnetostrictive Materials*. College Park, MY, 2000.

[85] R. I. Mahdi, W. C. Gan, and W. H. Abd Majid, “Hot plate annealing at a low temperature

of a thin ferroelectric P(VDF-TrFE) film with an improved crystalline structure for sensors and actuators," *Sensors (Switzerland)*, vol. 14, no. 10, pp. 19115–19127, Oct. 2014, doi: 10.3390/s141019115.

[86] V. Sencadas *et al.*, "Poling of ß-poly(vinylidene fluoride): Dielectric and IR spectroscopy studies," *E-Polymers*, no. May 2014, pp. 1–12, 2005, doi: 10.1515/epoly.2005.5.1.10.

[87] R. Gregorio, Jr. and M. Cestari, "Effect of crystallization temperature on the crystalline phase content and morphology of poly(vinylidene fluoride)," *J. Polym. Sci. Part B Polym. Phys.*, vol. 32, no. 5, pp. 859–870, Apr. 1994, doi: 10.1002/polb.1994.090320509.

[88] R. Khajavi and M. Abbasipour, "Piezoelectric PVDF polymeric films and fibers: Polymorphisms, measurements, and applications," in *Industrial Applications for Intelligent Polymers and Coatings*, Springer International Publishing, 2016, pp. 313–336.

[89] G. Teyssedre, A. Bernes, and C. Lacabanne, "DSC and TSC study of a VDF/TrFE copolymer'," 1993.

[90] E. S. Clark and L. S. Scott, "Superdrawn crystalline polymers: A new class of high-strength fiber," *Polym. Eng. Sci.*, vol. 14, no. 10, pp. 682–686, Oct. 1974, doi: 10.1002/pen.760141004.

[91] K. N. Bocan and E. Sejdić, "Adaptive transcutaneous power transfer to implantable devices: A state of the art review," *Sensors (Switzerland)*, vol. 16, no. 3, 2016, doi: 10.3390/s16030393.

[92] H. M. Chen *et al.*, "Tuning the interaction of an immiscible poly(l-lactide)/poly(vinylidene fluoride) blend by adding poly(methyl methacrylate) via a competition mechanism and the resultant mechanical properties," *RSC Adv.*, vol. 4, no. 76, pp. 40569–40579, 2014, doi: 10.1039/c4ra03936j.

[93] P. Vijay and V. Sumaria, "Advancement in P3HT PCBM solar cells , the most efficient Polymer Photovoltaic cell," in *Students' Chemical Engineering Congress*, 2014, no. 10, doi: 10.13140/2.1.1487.7442.

[94] S. Han, L. Yang, K. Gao, S. Xie, W. Qin, and S. Ren, "Spin polarization of excitons in

organic multiferroic composites," *Sci. Rep.*, vol. 6, pp. 1–7, 2016, doi: 10.1038/srep28656.

[95] B. Yang *et al.*, "Room-temperature organic ferromagnetism in the crystalline poly(3-hexylthiophene): Phenyl-C61-butyric acid methyl ester blend film," *Polymer (Guildf).*, vol. 54, no. 2, pp. 490–494, 2013, doi: 10.1016/j.polymer.2012.12.024.

[96] S. Islam, E. Islam, A. B. Ismail, H. Baerwolff, and E. T. Al, "Influence of Thickness and Annealing Temperature on the Optical Properties of Spin-Coated Photoactive P3HT : PCBM Blend," *Opt. Photonics J.*, vol. 2013, no. December, pp. 28–32, 2013.

[97] S. Ren and M. Wuttig, "Organic Exciton Multiferroics," *Adv. Mater.*, vol. 24, no. 6, pp. 724–727, Feb. 2012, doi: 10.1002/adma.201104250.

[98] M. Rispens, A. Meetsma, R. Rittberger, C. Brabec, N. Sariciftcib, and J. Hummelen, "Influence of the solvent on the crystal structure of PCBM† and the efficiency of MDMO-PPV:PCBM 'plastic' solar cells," *Chem. Commun.*, no. 17, 2003.

[99] G. Patern *et al.*, "Micro-focused X-ray diffraction characterization of high- quality [6,6]-phenyl-C61-butyric acid methyl ester single crystals without solvent impurities†," *J. Mater. Chem. C*, vol. 1, no. 36, 2013, doi: 10.1039/c3tc31075b.

[100] Y. H. Chen, P. T. Huang, K. C. Lin, Y. J. Huang, and C. T. Chen, "Stabilization of poly(3-hexylthiophene)/PCBM morphology by hydroxyl group end-functionalized P3HT and its application to polymer solar cells," *Org. Electron.*, vol. 13, no. 2, pp. 283–289, 2012, doi: 10.1016/j.orgel.2011.11.019.

[101] A. J. C. Wilson, "Scherrer after Sixty Years: A Survey and Some New Results in the Determination of Crystallite Size," *J. Appl. Crystallogr.*, vol. 11, no. 2, pp. 102–113, 1978.

[102] W. Oliver and G. Pharr, "An improved technique for determining hardness and elastic modulus using load and displacement sensing indentation experiments," *J. Mater. Res.*, vol. 7, no. 6, 1992.

[103] S. Do, S. Stepp, and G. Youssef, "Quasi-static and dynamic characterization of polyurea microspheres reinforced polyurea matrix composite," *Mater. Today Commun.*, vol. 25, no. July, p. 101464, 2020, doi: 10.1016/j.mtcomm.2020.101464.

[104] S. Majumdar, H. Majumdar, J. Lill, J. Rajander, and R. Laiho, “Correlation between Organic Magnetoresistance (OMAR) and Ferromagnetic ordering,” pp. 1–17.

[105] W. Qin, D. Jasion, X. Chen, M. Wuttig, and S. Ren, “Charge-transfer magnetoelectrics of polymeric multiferroics,” *ACS Nano*, vol. 8, no. 4, pp. 3671–3677, Apr. 2014, doi: 10.1021/nn500323j.

[106] W. Ge, “An overview on P3HT:PCBM, the most efficient organic solar cell material so far.”

[107] M. Gobbi and E. Orgiu, “The rise of organic magnetoresistance: Materials and challenges,” *J. Mater. Chem. C*, vol. 5, no. 23, pp. 5572–5580, 2017, doi: 10.1039/c6tc04403d.

[108] S. Majumdar, H. Majumdar, H. Aarnio, R. Laiho, and R. Osterbacka, “Magnetorsistance in Poly (3-hexyl thiophene) Based Diodes and Bulk Heterojunction Solar Cells,” vol. 129, no. April, pp. 161–165, 2009, doi: 10.1007/978-3-540-95930-4.

[109] M. Cox, S. H. W. Wouters, M. Kemerink, M. M. Wienk, P. Janssen, and B. Koopmans, “Tuning organic magnetoresistance in polymer-fullerene blends by controlling spin reaction pathways,” *Nat. Commun.*, 2013, doi: 10.1038/ncomms3286.

[110] V. Ern and R. E. Merrifield, “Magnetic Field Effect on Triplet Exciton Quenching in Organic Crystals,” *Phys. Rev. Lett.*, vol. 21, no. 9, pp. 609–611, 1968.

[111] P. Desai, P. Shakya, T. Kreouzis, and W. P. Gillin, “Magnetoresistance and efficiency measurements of Alq 3 -based OLEDs,” *Phys. Rev. B*, vol. 75, pp. 1–5, 2007, doi: 10.1103/PhysRevB.75.094423.

[112] P. A. Bobbert, T. D. Nguyen, F. W. A. Van Oost, B. Koopmans, and M. Wohlgenannt, “Bipolaron Mechanism for Organic Magnetoresistance,” *Phys. Rev. Lett.*, vol. 216801, no. November, pp. 1–4, 2007, doi: 10.1103/PhysRevLett.99.216801.

[113] N. A. Zaidi, S. R. Giblin, I. Terry, and A. P. Monkman, “Room temperature magnetic order in an organic magnet derived from polyaniline,” *Polymer*, vol. 45, no. 16, pp. 5683–5689, 2004, doi: 10.1016/j.polymer.2004.06.002.

[114] V. N. Prigodin, J. D. Bergeson, D. M. Lincoln, and A. J. Epstein, “Anomalous room temperature magnetoresistance in organic semiconductors,” *Synth*, vol. 156, pp. 757–761, 2006, doi: 10.1016/j.synthmet.2006.04.010.

[115] Y. Sheng *et al.*, “Hyperfine interaction and magnetoresistance in organic semiconductors,” *Phys. Rev. B*, vol. 74, p. 045213, 2006, doi: 10.1103/PhysRevB.74.045213.

[116] S. Ha, R. Su, J. Xing, Q. Zhang, and Q. Xiong, “Metal halide perovskite nanomaterials: synthesis and applications,” *Chem. Sci.*, vol. 8, pp. 2522–2536, 2017, doi: 10.1039/c6sc04474c.

[117] O. Shekhah, J. Liu, A. Fischer, and C. Woll, “MOF thin films: existing and future applications,” *Chem. Soc. Rev.*, vol. 40, no. 2, pp. 1081–1106, 2011, doi: 10.1039/c0cs00147c.

[118] A. Mhamdi, S. Sweii, H. Saidi, and F. Saidi, “Morphological , structural and optical properties of MEH-PPV : PC 70 BM nanocomposite film,” *J. Mol. Struct.*, vol. 1160, pp. 33–37, 2018, doi: 10.1016/j.molstruc.2018.01.063.

[119] S. C. Veenstra *et al.*, “Photovoltaic Properties of a Conjugated Polymer Blend of MDMO - PPV and PCNEPV,” *Chem. Mater.*, vol. 16, no. 4801, pp. 2503–2508, 2004.

[120] W. Qin, D. Jasion, X. Chen, M. Wuttig, and S. Ren, “Charge-Transfer Magnetoelectrics of Polymeric Multiferroics,” vol. 01, p. 20, 2020, doi: 10.1021/nn500323j.

[121] M. Kaltenbrunner *et al.*, “Ultrathin and lightweight organic solar cells with high flexibility,” *Nat. Commun.*, vol. 3, no. 770, 2012, doi: 10.1038/ncomms1772.

[122] Y. Yang *et al.*, “Large [6 , 6] -phenyl C 61 butyric acid methyl (PCBM) hexagonal crystals grown by solvent-vapor annealing,” *Mater. Chem. Phys.*, vol. 145, no. 3, pp. 327–333, 2014, doi: 10.1016/j.matchemphys.2014.02.017.

[123] R. Bunshah, *Handbook of Deposition Technologies for Films and Coatings*. Elsevier, 1994.

[124] D. Mattox, *Handbook of Physical Vapor Deposition (PVD) Processing*, 2nd ed. Oxford, UK: Elsevier, 2010.

[125] M. Farina, T. Ye, G. Lanzani, A. Donato, and G. Venanzoni, "Fast Ultrahigh-Density Writing of Low Conductivity Patterns on Semiconducting Polymers," pp. 1–22, 2013, doi: 10.1038/ncomms3668.

[126] S. Wang, S. Wang, C. Wang, Q. Li, L. Han, and W. Kong, "Terahertz Dielectric Properties of Polyvinylidene Fluoride Films," 2017.

[127] K. Zhang, Z. Hou, L. Kong, H. Fang, and K. Zhan, "Origin of Negative Imaginary Part of Effective Permittivity of Passive Materials," *Chinese Phys. Lett.*, vol. 34, no. 9, p. 097701, 2017, doi: 10.1088/0256-307X/34/9/097701.

[128] S. Newacheck, N. U. Huynh, and G. Youssef, "Colossal crystals in P3HT:PCBM blends for enhanced organic magnetism," *Cryst. Growth Des.*, vol. Under Revi, 2021.